Numerical simulations for the nonequilibrium control of quantum materials

Dissertation

zur Erlangung des Doktorgrades

an der Fakultät für Mathematik, Informatik und Naturwissenschaften

Fachbereich Physik

der Universität Hamburg

vorgelegt von

Gabriel Elias Topp

aus Friedrichshafen

Hamburg

2019

Gutachter/innen der Dissertation:	Dr. Michael Sentef Prof. Dr. Alexander Lichtenstein
Zusammensetzung der Prüfungskommission:	Dr. Michael Sentef Prof. Dr. Alexander Lichtenstein Prof. Dr. Angel Rubio Prof. Dr. Henning Moritz Prof. Dr. Daniela Pfannkuche
Vorsitzende/r der Prüfungskommission:	Prof. Dr. Daniela Pfannkuche
Datum der Disputation:	22.04.2020
Vorsitzender Fach-Promotionsausschusses PHYSIK:	Prof. Dr. Günter Hans Walter Sigl
Leiter des Fachbereichs PHYSIK:	Prof. Dr. Wolfgang Hansen
Dekan der Fakultät MIN	Prof. Dr. Heinrich Graener

Eidesstattliche Versicherung / Declaration on oath

Hiermit versichere ich an Eides statt, die vorliegende Dissertationsschrift selbst verfasst und keine anderen als die angegebenen Hilfsmittel und Quellen benutzt zu haben.

Die eingereichte schriftliche Fassung entspricht der auf dem elektronischen Speichermedium.

Die Dissertation wurde in der vorgelegten oder einer ähnlichen Form nicht schon einmal in einem früheren Promotionsverfahren angenommen oder als ungenügend beurteilt.

Hamburg, den

Unterschrift der Doktorandin / des Doktoranden

Preface

The work for this thesis has been carried out at the Max Planck Institute for the Structure and Dynamics of Matter (MPSD) in Hamburg and at the University of Hamburg between December 2015 and December 2019 under the supervision of Dr. Michael Sentef, Prof. Angel Rubio, and Prof. Alexander Lichtenstein. Financial support was provided through the Emmy Noether program (SE 2558/2-1) and the European Research Council (No. ERC-2015-AdG694097).

First and above all I would like to express my deepest gratitude to Michael A. Sentef, my supervisor and mentor, for being a constant source of support, guidance, and encouragement and for always being available for discussions and advice. Without any doubt I can recommend all potential PhD students who are interested in ultrafast phenomena to seek his supervision. I want to thank Angel Rubio for giving me the opportunity to be part of his international, open-minded, cutting-edge research team and for his guidance and support. I am grateful to Alexander Lichtenstein for his supervision. I want to express my gratitude to Lex Kemper for teaching me the ways of efficient programming, and for making my three month visit to Raleigh (NC, USA) a great experience both professionally and privately. Furthermore, I want to thank Shunsuke Sato, Lede Xian, James McIver, and Gregor Jotzu for many great discussion which fostered the progress of my projects. Thanks to Fabio Covito, Vasilis Rokaj, and Davis Welakuh for being awesome office mates, who were always up to both having fun and sincere scientific discussions. I want to thank Julia Quante and Neda Lotfiomran for support and guidance via the IMPRS UFAST graduate program and beyond. Furthermore, I owe special thanks to my best friend Teresa Reinhard, who introduced me to the group and thus started the ball rolling. Finally, I want to express my deepest gratitude to my family. To my parents, who taught me curiosity and who always support me, and especially to my loved wife Ann-Christin. Without her always covering my back, cheering me up, caring for our daughter, and giving me helpful advice regarding good scientific practice, I would never have been able to complete this exciting journey.

Contents

1 Complete list of publications

I. **G. E. Topp**, N. Tancogne-Dejean, A. F. Kemper, A. Rubio, and M. A. Sentef. All-optical nonequilibrium pathway to stabilising magnetic Weyl semimetals in pyrochlore iridates. *Nature Communications*, 9(1):4452, Oct 2018. URL https://www.nature.com/articles/s41467-018-06991-8

II. M. Chávez-Cervantes, **G. E. Topp**, S. Aeschlimann, R. Krause, S. A. Sato, M. A. Sentef, and I. Gierz. Charge density wave melting in one-dimensional wires with femtosecond subgap excitation. *Phys. Rev. Lett.*, 123:036405, Jul 2019. URL https://link.aps.org/doi/10.1103/PhysRevLett.123.036405

III. **G. E. Topp**, G. Jotzu, J. W. McIver, L. Xian, A. Rubio, and M. A. Sentef. Topological Floquet engineering of twisted bilayer graphene. *Phys. Rev. Research*, 1:023031, Sep 2019. URL https://link.aps.org/doi/10.1103/PhysRevResearch.1.023031

1.1 Declaration of contribution

I. **G. E. Topp** wrote the code for the model, performed all model simulations, analysed the data and created all plots. The manuscript was written by **G. E. Topp** and M. A. Sentef. The TDDFT calculations were performed by N. Tancogne-Dejean. All authors discussed the results.

II. M. Chávez-Cervantes performed the experiment together with S. Aeschlimann, R. Krause, and I. Gierz. The main part of the manuscript was written by M. Chávez-Cervantes and I. Gierz. **G. E. Topp** performed the model calculations, created the corresponding figures of the supplement, and wrote the corresponding text passages of the supplement. All authors discussed the results.

III. L. Xian provided a `Fortan90` code, containing a DFT-fitted implementation of the equilibrium Hamiltonian and a method for the generation of the crystal lattice. **G. E. Topp** translated this code to `Python` and `C++`. **G. E. Topp** extended the code by Floquet and Berry curvature methods. **G. E. Topp** performed all model calculations, analysed the data, and created all figures. The manuscript was written by **G. E. Topp** and M. A. Sentef. All authors discussed the results.

2 Abstract

Significant developments over the past decades in creating ultrashort laser pulses on the sub-picosecond time scale have paved the way for nonequilibrium many-body dynamics to become an active research field in condensed matter physics. A central goal of ultrafast material science is the engineering of material properties by precisely tailored laser excitations on their intrinsic microscopic time- and energy scales. Providing and applying a comprehensive set of numerical tools for the simulation of the ultrafast control over the electronic, magnetic, and topological degrees of freedom in different kinds of quantum materials is the central topic of this thesis. In the following, this kind of control is demonstrated for three different materials.

The ordered phase of correlated materials can be characterised by an order parameter which fundamentally impacts the material properties. Theoretical investigations of the 227 pyrochlore iridates showed a rich variety of equilibrium phases in dependence of a magnetic order parameter, which can be tuned by the electronic correlations. By a combination of time-dependent ab initio calculations and magnetic mean-field model simulations, we show how an ultrafast laser-induced modification of the effective Hubbard U can transiently induce a topologically nontrivial Weyl phase. By probing the emerging Weyl points with time- and angle-resolved photoemission spectroscopy in our simulations, we provide an experimentally relevant nonequilibrium pathway towards the stabilisation and measurement of Weyl fermions in pyrochlore iridates.

One-dimensional indium wires are the second investigated compound. At a critical temperature this system passes a thermal critical point towards a charge-density wave phase. The transition is accompanied by the opening of an energy gap at the Fermi surface. It can be tracked by angle-resolved photoemission spectroscopy. Laser-mediated photo-doping offers the possibility to dynamically drive the system through the insulator-to-metal transition. This was shown in an experiment with femtosecond mid-infrared sub-gap excitations. Within a model simulation, we identify multi-photon absorption as the dominant driving process for the transition.

As last material, twisted bilayer graphene is investigated. In 2019, an ultrafast transport experiment showed a light-induced anomalous Hall effect in graphene. An intriguing new aspect is that the measured Hall conductivity might in part be a non-intrinsic Berry curvature effect of the 2D electronic system, originating from a transient breaking of time-reversal symmetry. Motivated by these findings, we investigate the topological properties of the equilibrium and Floquet-dressed band structure of twisted bilayer graphene in the intermediate-angle regime. We show that chiral laser light can induce a phase transition to a topologically nontrivial state with an effective winding number analogous to a Chern insulator. Furthermore, we show that this transition can be controlled by an applied backgate voltage.

Our theoretical findings underline the outstanding role of ultrafast material science as a platform for the tailored engineering of material properties on demand.

3 Zusammenfassung

Wesentliche Entwicklungen in den letzten Jahrzehnten bezüglich der Erzeugung ultraschneller Laserpulse im Subpikosekundenbereich machen Vielteilchen-Nichtgleichgewichtsdynamik heute zu einem wichtigen Bereich der Festkörperphysik. Eine zentrale Aufgabe der ultraschnellen Materialwissenschaften ist die Manipulation von Materialeigenschaften durch präzise angepasste Laseranregung auf den zugrunde liegenden mikroskopischen Zeit- und Energieskalen. Die Bereitstellung und Anwendung einer umfassenden numerischen Toolbox zur Simulation der ultraschnellen Kontrolle von elektronischen, magnetischen und topologischen Freiheitsgraden in verschiedenen Quantenmaterialien ist das zentrale Thema dieser Arbeit. Dies wird im Nachfolgenden anhand drei verschiedener Materialien demonstriert.

In korrelierten Materialien kann eine geordnete Phase oftmals durch einen Ordnungsparameter, der die Materialeigenschaften maßgeblich beeinflußt, beschrieben werden. Theoretische Untersuchungen an 227-Pyrochloriridate zeigen eine Vielzahl von Gleichgewichtsphasen in Abhängigkeit eines magnetischen Ordnungsparameters, welcher durch Manipulation der elektronischen Korrelationen kontrolliert werden kann. Wir zeigen anhand einer Kombination von zeitabhängigen abinitio Rechnungen und magnetischen Modellsimulationen, dass eine ultraschneller laserinduzierte Modifikation der effektiven Hubbard-Wechselwirkung U vorübergehend eine Weyl-Phase induzieren kann. Durch zeit- und winkelaufgelöste Photoelektronenspektroskopie, weisen wir Weyl-Fermionen in unseren Simulationen nach. Dadurch demonstrieren wir einen experimentell relevanten Nichtgleichgewichtsansatz zur Erzeugung und Messung von topologischen Weyl-Fermionen in Pyrochloriridaten.

Als zweites Material werden eindimensionale Indiumketten untersucht. Bei einer kritischen Temperatur durchlaufen diese einen Phasenübergang in eine symmetriegebrochene Phase mit Ladungsdichtewelle. Der Phasenübergang, welcher mit der Öffnung einer Bandlücke an der Fermioberfläche einhergeht, kann durch winkelabhängige Photoelektronenspektroskopie nachgewiesen werde. Laserinduzierte Elektronenanregung bietet eine Möglichkeit, einen ultraschnellen Isolator-Metall-Übergang im Material zu erzwingen. Selbiger wurde kürzlich experimentell anhand von subresonanter Starkfeldanregung nachgewiesen. Mithilfe einer Modellrechnung identifizieren wir Mehrphotonenabsorption als den dominanten Prozess für den Phasenübergang.

Als letztes Material wird zweilagiges Graphen untersucht. Im Jahr 2019 wurde in einem Transportexperiment ein anormaler lichtinduzierter Halleffekt in Graphen nachgewiesen. Interessant ist daran, dass die gemessene Hall-Leitfähigkeit zum Teil das Resultat einer nicht-intrinsischen Berrykrümmung innerhalb des zweidimensionalen elektronischen Systems ist, welche aus einer gebrochenen Zeitumkehrinvarianz resultiert. Dadurch motiviert, untersuchen wir die topologischen Eigenschaften der elektronischen Bandstruktur von verdrehten, zweilagigen Graphenschichten, im Gleichgewicht und im Floquet-getriebenen Fall. Wir zeigen, dass chirales Laserlicht einen Pha-

senübergang zu einer topologisch nicht-trivialen Phase mit einer effektiven Windungszahl analog zu einem Chern-Isolator erzeugen kann. Weiterhin demonstrieren wir, dass dieser Phasenübergang durch eine angelegte Gatespannung kontrolliert werden kann.

Die präsentierten Ergebnisse verdeutlichen die wichtige Rolle der ultraschnellen Materialwissenschaften, um die Eigenschaften von Materialien nach Bedarf anzupassen.

4 Introduction

The ultrafast control of material properties requires the availability of intense ultrashort laser pulses which act on the intrinsic time scales of the investigated system. Over the past decades huge efforts have been made in creating such laser sources which are able to generate laser pulses down to the femto- and even attosecond time scale over a broad frequency spectrum. These developments paved the way for a plethora of ultrafast theoretical and experimental investigations, which aim for the dynamical control over certain physical properties in various kinds of materials. Important examples are the ultrafast light control of internal couplings [4–6], measured features of light-induced superconductivity [7, 8] and the ultrafast switching between collective phases of matter [9–11]. The theoretical description of the optical control over different phases of matter with intense laser fields is the central topic of this thesis. In the context of this work, a tool box of numerical methods is provided. This tool box allows a nonequilibrium description of different kinds of driven phase transitions in various kinds of materials.

In order to control a phase transition, a tuning knob which allows the manipulation of its involved dominant energy scales has to be identified. The ordered macroscopic phases of a correlated material can be characterised by an order parameter. This order parameter has a strong impact on the Hamilton operator and its spectrum. Its control enables the manipulation of the macroscopic properties of a system. The magnetic phase transition from a paramagnetic metallic to an ordered antiferromagnetic insulating phase of the Hubbard model is an important and intensively studied example. Here, the magnetisation defines a local order parameter. It can be tuned by the local electronic interaction U. In a driven system far from equilibrium such transitions take place as a real time process, which can be tracked by a time-dependent order parameter. Naturally, thermalisation and dissipation-induced relaxation processes set a finite time window for the detection of such dynamically induced transitions. The dominant time scale of the order parameter dynamics tend to significantly increase in close proximity to critical points [12]. Due to this critical behaviour, light-induced new states of matter are potentially able to outlive the pump duration. This finite lifetime is important for the experimental detection of transiently induced nonequilibrium features, as it increases the time-window for probing the transient state.

In the last decade a consolidation between condensed matter physics and the more mathematical field of topology have lead to the experimental realisation and theoretical classification of various quantum materials which come along with a great number of novel striking physical phenomena. These phenomena range from the anomalous Hall effect [13–15] to momentum-spin locking [16] and possible realisations of chiral superconductivity in topological insulators [17–19]. Topological phase transitions might come along with changes of e.g. electronic or magnetic properties. Nevertheless, they are conceptually very different from conventional Landau phase transitions, which can be characterised by a local order parameter. Certain classes of topological

systems can be classified by one or more topological invariants, which do not change under adiabatic deformation. For topological insulators this is known as the $\mathcal{Z}_2$-invariant which originates from a combination of time-reversal symmetry and inversion symmetry. Topological phase transitions are always discrete. This manifests by the integer nature of their associated invariants. The great advantage of the topological aspect is generally twofold. First, the topology of the system and its associated properties are protected by symmetry. This makes it robust against local perturbations which preserve this particular symmetry. Second, all systems and corresponding Hamiltonians which are adiabatically connected, necessarily exhibit the same physical features.

Pump-probe spectroscopy offers the experimental tool to dynamically control and gain time-resolved information about nonequilibrium states of matter. The general idea of pump-probe spectroscopy is that an excitation is followed by a probe of the resulting excited-state response. By adjusting the time delay between pump and probe, the time evolution after the excitation can be tracked. Time-resolved pump-probe spectroscopy offers the possibility to disentangle processes in time which might be tedious to separate regarding their energy scale. From a computational perspective, the simulation of pump-probe measurements is the most natural way of extracting time-resolved information about a nonequilibrium state of matter. That way, the intertwining of time- and energy scales, which is an inherent feature of every real time-dependent measurement, is naturally incorporated. Time- and angle-resolved photoemission spectroscopy (tr-ARPES) is an established and widely used pump-probe method to investigate the electronic system. Typically, after the electrons were pumped via a high-intensity low-energy laser pulse, a high-energy probe pulse photoemmits the excited charge carriers. By measuring the exit angle and the velocity of the emitted electrons, their momentum and energy can be calculated. This provides dynamical information about the occupied parts of the electronic bands of a quantum material. While the temporal resolution is set by the time delay between the pulses, the energy resolution is set by the duration of the probe pulse.

Laser heating is an important issue for all optical experiments. In the newly emerging field of cavity materials [20–23], a small number or even zero photons might be sufficient to induce a measurable change within the system's energy landscape due to strong light-matter couplings. However, in common pump-probe setups, much higher field intensities are necessary in order to induce a measurable response of the excited matter system. These high intensities allow a classical treatment of the pump field. However, the pump-induced energy flow from the laser field into the probe material can result in strong heating effects, which reach from washed-out electronic characteristics to the complete destruction of a probe material. A reduction of the effective interaction time by using short pulses can scale down the amount of transferred energy. Furthermore, ultrashort laser pulses allow the manipulation of material properties on time scales that are much shorter than the typical time scales on that a system typically thermalises. For short probe delays the nonthermal excited-states can be measured. Moreover, the electronic

heating can be reduced by tuning the laser frequency off-resonant to the internal energy degrees of freedom. As was demonstrated by Sato and colleagues [24] for the light-induced anomalous Hall effect in graphene, a resonant population transfer often generates a strong response of the coupled matter system. This response can dominate other potentially interesting effects, like in the mentioned work, a topological contribution to the Hall conductivity. Avoiding such strong laser-induced heating effects is an important task of all projects which are presented within this thesis.

In the following, three important materials, for which collective material properties can be controlled by intense time-dependent external fields, are introduced.

4.1 Topological Weyl fermions in pyrochlore iridates

A certain class of materials that has raised considerable attention within the last years are systems which host Weyl fermions in their bulk band structure. From a theoretical point of view, a pair of Weyl fermions can be constructed from a degenerate pair of Dirac points by either breaking inversion symmetry or time-reversal symmetry. Weyl fermions are a special mass-less solution of the Dirac equation for relativistic electrons, originally postulated by Hermann Weyl in 1929 [25]. In a Weyl material [26–29], Weyl fermions appear as low energy excitations of the bulk band structure, which can be effectively described by the Weyl equation. The two Weyl quasiparticles, which are separated in momentum space have opposite handedness. A pair of Weyl points can be interpreted as a realisation of magnetic point charges with opposite sign. This chiral anomaly gives rise to interesting optical and transport phenomena, like a negative magneto-resistance [30]. As a result of the bulk-boundary correspondence, the two Weyl points are connected by conducting surface states, so-called Fermi arcs. Weyl fermions were first experimentally observed in TaAs in 2015 [27] by angle-resolved photoemission spectroscopy both directly in the bulk as Weyl cones and indirectly by their Fermi arcs. In this material, inversion symmetry is intrinsically broken while time-reversal symmetry is preserved.

As a potential host of a time-reversal symmetry-broken Weyl semimetallic (WSM) phase the $R_2Ir_2O_7$ (R is yttrium or a rare-earth element) pyrochlore iridate family with spontaneous magnetic order raised a lot of interest. In these correlated materials the extended nature of the 5d atomic orbitals yields a spin-orbit coupling comparable to the local Coulomb repulsion. Together with the emerging band topology this leads to a rich equilibrium phase diagram, as shown by DFT+U+SO (density functional theory + Hubbard U + spin-orbit coupling) calculations by Wan et al. [26]. For these correlation-driven phases, they showed that by controlling the effective electronic interaction (local Hubbard U), the magnetic order of the system could be manipulated. For systems with a nonmagnetic R-site, the magnetic properties are dominated by the Ir atoms [31–33], which build corner-sharing tetrahedra on a fcc Bravais lattice. A reduction of the Coulomb repulsion within the iridium 5d orbitals results in a transition from an antiferromagnetic insulating phase to

a topological Weyl phase and finally to a paramagnetic metallic phase. The emerging magnetic phases energetically favour an inversion-symmetry preserving all-in/all-out (AIAO) spin order. The appearance of these ordered magnetic phases was independently reproduced by CDMFT (cluster dynamical mean field theory) simulations performed by Go et al. [34] and more recently by the group of A. Millis [33]. These calculations went beyond the mean-field single-particle picture. Though direct proof is still lacking, most experimental results point towards a magnetic ground state [35–39], with recent evidence for magnetic AIAO order [40–43]. In their work [32], Witczak-Krempa and collaborators investigated the equilibrium phase diagram of a prototypical tight-binding model Hamiltonian with spin-orbit coupling. In this work, the local electronic interactions were included as a mean-field Hubbard term, which gave rise to a magnetic order parameter. In agreement with the DFT and CDMFT simulations, they found stable magnetic groundstates with AIAO order by tuning the Hubbard U. For intermediate values of U they identified a magnetic Weyl phase by the appearance of Weyl cones in the equilibrium band structure. However, this topological Weyl phase appeared to be quite unstable against melting at finite temperatures and required fine-tuning of the magnetic order parameter.

All these theoretical investigations suggest that in a hypothetical experiment in which one could adiabatically tune the electronic correlations, the control over the magnetic order parameter would allow one to switch the system to a topological Weyl phase with broken time-reversal symmetry. It is known that the effective Hubbard interaction is strongly affected by screening effects [33]. It was shown that the electronic screening can be dynamically modified by the interaction with an intense external laser field [44]. Via self-consistent time-dependent DFT+U calculations , N. Tancogne-Dejean and collaborators showed for the strongly correlated insulator NiO that by an off-resonant femtosecond excitation the effective electronic interactions can be manipulated on the ultrafast time scale of the laser pulse [6]. In this material the band structure crucially depends on the strength of the electronic correlations. The suppressed screening and the resulting ultrafast reduction of U was explained by the delocalised nature of the excited-state subset of the Hilbert space. The TDDFT+U (time-dependent density functional theory + Hubbard U) calculations for pyrochlore iridates, which are presented in this thesis, are based on this very idea. They motivated the subsequent magnetic mean-field model calculations, as discussed in more detail in Sec. 6.1, and gave rise to the idea of light-induced non-trivial topology in pyrochlore iridates [1].

4.2 Metal-to-insulator transition in one-dimensional indium wires

In condensed matter physics, low-dimensional electronic systems are of special interest. Their reduced spatial degrees of freedom give rise to a number of interesting physical effects that are not present in higher-dimensional systems. Important features are the appearance of non-Fermi-liquid behaviour [45], spin ordering [46, 47], and the instability towards the formation of

charge-density waves (CDW). In the latter case, at low temperatures, the response of the low-dimensional electron gas becomes unstable towards external perturbations fulfilling the nesting condition $q = 2\mathbf{k}_\mathrm{F}$, where $\mathbf{k}_\mathrm{F}$ is the Fermi momentum. This instability results in an electronic phase transition to a low-symmetry phase with a spatial variation of the electronic density. In the case that strong electron-phonon coupling is the dominant energy scale, the transition is coined "Peierls transition". The CDW is accompanied by a periodic modulation of the crystal lattice which reduces the crystal symmetry. This lattice distortion is the result of a softening of the associated phonon mode, driven by a Kohn anomaly [48]. The phase transition can be characterised by a complex order parameter. Its time- and space-dependent modulation defines the amplitude and phase mode of the symmetry-broken CDW phase, respectively. On the other hand, the metal-to-insulator transition can be of purely electronic nature in which case it is driven by electronic correlations. Importantly, the transition from the metallic phase to the CDW phase is accompanied by the opening of an energy gap at the Fermi surface in the electronic band structure. The condensation energy is defined as the difference between energies of the normal and the insulating phase, $E_\mathrm{cond} = E_\mathrm{norm} - E_\mathrm{CDW}$.

In 1999, one-dimensional indium wires, self-assembled on a Si(111) surface, were found to exhibit a CDW phase below a critical temperature of 100 K [49]. In the metallic phase each indium wire consists of parallel pairs of zigzag chains of indium atoms. As discussed in this influential work, the metal-insulator transition can be tracked by different experimental indicators. The periodic modulation of the charge carriers can be directly measured in an scanning tunneling microscopy (STM) experiment. By reflection high-energy electron diffraction (RHEED) the structural changes of the atomic lattice can be probed. Moreover, by ARPES measurements, changes of the electronic band structure at the Fermi surface can be detected. While a structural transition from the two indium chains with a (4×1) unit cell to a hexagonal (8×2) cell is well established, its microscopic origin is still under debate. Suggestions range from the Peierls picture [49–52], over an order-disorder transition [53, 54], to many-body correlation effects [55]. Based on DFT simulations [56], an atomistic picture with bond breaking and subsequent new bond formation was favoured against a nesting-induced Peierls dimerisation. Starting from a DFT-fitted Su-Schrieffer-Heeger (SSH) model, a study by Jeckelmann et al. proposed a first-order grand canonical Peierls transition in which the Si-substrate acts as a particle reservoir [57]. Their theoretical investigations were underpinned by Raman spectroscopy that showed partial phonon softening of certain shear and rotary modes when the critical temperature was approached from below. Due to their strong coupling to the electronic CDW, these modes are believed to play an important role for the transition.

In a time- and angle-resolved photoemission experiment Chávez-Cervantes and collaborators investigated the electronic structural dynamics of an optically driven insulator-to-metal transition in indium wires [58]. The key motivation for this nonequilibrium study of the transition was to

gain a deeper understanding of the microscopic processes involved. This was done by an analysis of the time scales that were involved in the CDW melting process. By photo-doping above the CDW band gap via an ultraviolet femtosecond pump pulse, they found the quasi-particle band gap to close on a sub-picosecond time scale that is slightly above one quarter of the oscillation period of the dominantly involved phonons (≈ 660 fs). From this time scale a Peierls-like transition was inferred. Because of the measurement of a long-lived electronic response, which is absent in the pumped metallic phase, a trapping in a meta-stable (4×1) phase was suggested. The existence of such a meta-stable normal phase was already claimed in [59, 60], based on time-resolved REHHD experiments. In a follow-up experiment Chávez-Cervantes et al. investigated the ultrafast CDW melting by femtosecond sub-gap excitations [2]. The theoretical analysis of the microscopic mechanism behind the light-induced metal-to-insulator transition is the second important part of this thesis.

4.3 Floquet engineering of twisted bilayer graphene

In electronic systems, light-induced phenomena can lead to transport properties which differ from equilibrium intuition. Particular examples are the above discussed suppression of electronic correlations by a strong laser field [1, 6], the sub-resonant melting of electronic order [2] and light-induced superconductivity [8]. Manipulating matter with time-periodic perturbations holds great promise for designing material properties on demand. In a significant theoretical work [13], Oka and Aoki showed that Floquet engineering offers a platform to control the topological landscape of Dirac materials. Within the context of Floquet theory they showed for graphene that, in analogy to Haldane's model [61], the breaking of time-reversal symmetry via circularly polarised light can induce a topologically nontrivial Chern-insulating phase. In contrast to the above described collectively ordered phases, this topological transition is characterised by an integer (Chern number), which can only change due to nonadiabatic deformation. Together with the application of a dc source-drain electric field, the light-engineered Berry curvature results in a finite anomalous Hall conductance. Motivated by these theoretical investigations, James McIver and collaborators built an ultrafast transport experiment in order to measure this light-induced anomalous Hall effect [15]. The sub-picosecond Hall current signal was tracked in a time-dependent fashion by a photo-conductive switch. In their setup, the Hall conductivity can be measured as a function of the chemical potential, which can be adjusted by a backgate voltage. By comparison with the Floquet-dressed band structure, they interpreted the measured anomalous Hall conductivity as a nonequilibrium Berry curvature effect. In a theoretical follow-up work [24], Sato et al. analyzed this light-induced anomalous Hall effect in graphene by investigation of an effective Dirac model with dissipative real-time dynamics. They found that the anomalous Hall conductance is predominantly caused by an imbalance of the resonantly excited charge carriers, while they only found a small contribution from the nonequilibrium Berry curvature of the natural

orbital states for realistic driving field strengths. Ultimately, these findings gave rise to two important questions. First, is it possible to reduce the electronic heating in order to minimize population imbalance effects in favor of topological Berry transport? Second, can one think of an experimental tuning knob to control this topological phase transition? For about ten years it has been a known fact that stacking two layers of graphene and introducing a relative twist angle between both layers offers a platform for tuning the electronic degrees of freedom [62–64]. The resulting Moiré atomic structure with regions of Bernal AA-stacking and AB-stacking yields a periodic modulation of the effective interlayer coupling on length scales up to several nanometers. Depending on the twist angle this results in a strong localisation of the charge carriers in the AA regions that is accompanied by a renormalisation of the electronic bandwidth and the Fermi velocity. At a discrete set of twist angles, coined magic angles, this leads to a vanishing Fermi velocity at the Dirac points and an electronic bandwidth of the lowest energy manifold of several meV. A seminal experimental investigation by the group of P. Jarillo-Herrero in 2018 [65, 66], which proved the existence of presumably unconventional superconductivity in close proximity to a correlated insulating phase in magic-angle graphene, generated a burst of attention for this material. As will be shown in this work, focusing on the intermediate-angle regime, twisted bilayer graphene offers a perfect platform to perform Floquet topological engineering with additional control knobs compared to single-layer graphene.

5 Published manuscripts

This section contains references to the published manuscripts listed in Sec. 1 (PDF documents removed for copyright reasons).

5.1 Publication I

G. E. Topp, N. Tancogne-Dejean, A. F. Kemper, A. Rubio, and M. A. Sentef. All-optical nonequilibrium pathway to stabilising magnetic Weyl semimetals in pyrochlore iridates. *Nature Communications*, 9(1):4452, Oct 2018. URL https://www.nature.com/articles/s41467-018-06991-8

5.2 Publication II

M. Chávez-Cervantes, **G. E. Topp**, S. Aeschlimann, R. Krause, S. A. Sato, M. A. Sentef, and I. Gierz. Charge density wave melting in one-dimensional wires with femtosecond subgap excitation. *Phys. Rev. Lett.*, 123:036405, Jul 2019. URL https://link.aps.org/doi/10.1103/PhysRevLett.123.036405

5.3 Publication III

G. E. Topp, G. Jotzu, J. W. McIver, L. Xian, A. Rubio, and M. A. Sentef. Topological Floquet engineering of twisted bilayer graphene. *Phys. Rev. Research*, 1:023031, Sep 2019. URL https://link.aps.org/doi/10.1103/PhysRevResearch.1.023031

6 Numerical details and results

For each project, this section provides an analysis of the most important numerical tools and how these tools are applied to the particular problem. The corresponding code is largely written in `C++`, parts are written in `Python`. The implementations of the basic mathematical functions, which are used for all projects, are listed in Appendix A. Important functions of the different projects are listed in a reduced and commented version in Appendix B. The motivation for discussing the numerical implementations, which were used to solve the addressed physical problems, is generally twofold. First, providing the code should help the reader to gain a deeper understanding of the numerical approaches. Second, it should be understood as a technical guidance for other researchers, who have to tackle similar problems.

6.1 Publication I

All-optical nonequilibrium pathway to stabilising magnetic Weyl semimetals in pyrochlore iridates In this project, the stabilisation of a transient Weyl semimetallic phase in pyrochlore iridates, controlled by a laser-reduced magnetization, is investigated. The details of the numerical approach, which led to the model results, presented in publication **I** (Ref. [1]), are analyzed in the following. The referred functions are listed in Appendix B.1. A complete version of the code can be accessed at `https://github.com/Fizztopp/Pyrochlore.git`.

For the model calculations, a prototypical pyrochlore iridates tight-binding Hamiltonian (Eq. 1 of Ref. [1]) in a global pseudospin basis, as introduced by Witczak-Krempa et al. [32], is used. In case of a nonmagnetic R-site, which is the focus here, the magnetic properties of the $R_2Ir_2O_7$ (R-227) family are dominated by the 5d electrons of the iridium atoms [26, 31–34]. These build corner-sharing tetrahedra on a face-centered cubic (fcc) Bravais lattice. Crystal-field splitting together with strong spin-orbit coupling allow an effective description by energetically well separated $J_{\text{eff}} = 1/2$ Kramers doublets. Ultimately, this yields an effective eight-band description. The first term of the Hamiltonian describes the kinetic part, including nearest-neighbour hopping (NN), both direct and oxygen-mediated, and next-nearest neighbour hopping (NNN) (see Eq. 9 of Ref. [1]). It has only nonvanishing terms in the single-particle sector. Due to its bilinear form it can be represented by a quadratic matrix. This matrix can be diagonalised in order to obtain its eigenvalues. These eigenvalues correspond to the eigenenergies of the kinetic Hamiltonian. This kind of finite interaction generally induces electronic correlations. In the real space representation it is defined as

$$H_U = U \sum_i c^\dagger_{i\uparrow} c_{i\uparrow} c^\dagger_{i\downarrow} c_{i\downarrow}.$$

This two-body operator, despite its simple structure, complicates the problem tremendously as it does not commute with the kinetic term. It is not possible to find a mutual eigenbasis and the

problem can per se not be reduced to a problem of independent particles for finite interactions. The resulting exponential scaling of the Hilbert space with the system dimension is a well-known problem of many-particle physics. This problem has been studied intensively over the last decades, e.g. by the Hubbard model and various numerical approximation techniques have been investigated. A numerically efficient approximation, which is used here, is to perform a mean-field decoupling of the two-body operator. The general idea is to mimic the electronic interactions by coupling each particle to a background potential which is generated by an averaged contribution of all particles themselves. That way the second term reduces to a single-particle operator. For the chosen magnetic decoupling, this yields an approximated energy contribution (see Eq. 2 Ref. [1])

$$H_{\mathrm{U}} \to -U \sum_{\mathbf{k}a} (2\langle \mathbf{j}_a \rangle \cdot \mathbf{j}_a(\mathbf{k}) - \langle \mathbf{j}_a \rangle^2).$$

The obtained Hamiltonian well reproduces the magnetic phase diagram found in LSDA+U (local spin density approximation + Hubbard U) calculations [26] and the crucial AIAO magnetic order which is supported by most experimental evidence [40–43]. Moreover, it agrees with the magnetic phases found in non-local CDMFT calculations [33, 34]. In this light the used mean-field Hamiltonian is assumed to correctly reproduce the crucial properties of the investigated bulk magnetic material.

The creation of the Hamiltonian matrix is implemented by the function 1, listed in Appendix B.1. The trivial energetic shift which is induced by the quadratic term $\langle \mathbf{j}_a \rangle^2$ has no effect on the magnetic order parameter m (see Eq. 10 of Ref. [1]) but adds up to the total energy. This term is important in order to make valid predictions about the equilibrium total energy. The mean-field expectation values of the pseudospin operators at the four sites define the magnetic order parameter (see Ref. [1])

$$m = \frac{1}{4} \sum_a \sqrt{\langle j_a^x \rangle^2 + \langle j_a^y \rangle^2 + \langle j_a^z \rangle^2},$$

where the expectation values are calculated by

$$\langle \mathbf{j}_a^i \rangle = 1/N \sum_{\mathbf{k}} \mathrm{Tr} \left\{ \rho(\mathbf{k}) \mathbf{j}_a^i(\mathbf{k}) \right\}.$$

Translational symmetry regarding the Bravais lattice allows an effective block-diagonal description in the $\mathbf{k}$-dependent orbital basis. In the continuous picture of an infinitely sized crystal lattice, the mean-field observables are calculated by a $\mathbf{k}$-dependent integration over the reciprocal unit cell. This integration is practically approximated by a summation over a finite set of grid points. Convergence is ensured by the choice of the grid spacing. As the low-energy magnetic phases under consideration preserve inversion symmetry, $\mathbf{r} = -\mathbf{r} \leftrightarrow \mathbf{k} = -\mathbf{k}$, a reduced zone of half the size is employed. In the calculation of the mean-field average, the contributions are weighted

by an integer number that indicates the number of equivalent copies of a certain $\mathbf{k}$-point. For the computation of the k-point grid the `Python`-package `spglib` is used. The calculation of the mean-field pseudospin vectors is implemented by method 2 of Appendix B.1.

The first step in order to perform a meaningful time-propagation is to identify the initial state. The system is chosen to start in (quasi-)thermal equilibrium which, by satisfying the condition $\left[\rho_(\mathbf{k}), H(\mathbf{k})\right] = 0 \ \forall \mathbf{k}$, is a steady state of the initial Hamiltonian. It is fully determined by the single-particle density operator, which is calculated self-consistently. The procedure is as follows: one starts with an initial assumption for the mean-field pseudospin vectors $\langle \mathbf{j_a} \rangle$. For a fixed set of hopping parameters and a fixed Hubbard interaction U this fully describes the single-particle Hamiltonian. By diagonalisation of the Hamiltonian matrix, its eigenenergies $\epsilon_{\mathbf{k}}^{a\sigma}$ are calculated. By an initially guessed chemical potential μ and a fixed temperature T the density operator can be determined. In the energy eigenbasis it is a diagonal matrix with the Fermi functions $f_{\mathbf{k}}(\epsilon_{\mathbf{k}}^{a\sigma}, \mu, T)$ appearing as diagonal entries. The total particle number can now be calculated by the trace $N_{\mathrm{tot}} = \sum_{\mathbf{k}a\sigma} f_{\mathbf{k}}(\epsilon_{\mathbf{k}}^{a\sigma}, \mu, T)$. In the next step, the chemical potential is adjusted by $\mu = \mu - \delta \cdot (N_{\mathrm{tot}} - N_{\mathrm{target}})$, where N_{target} defines the desired particle number and $\delta = 10^{-5}$ eV a small correction factor. Here, N_{target} is chosen such that it provides a half-filled system ($N_{\mathrm{target}} = 4 \cdot$ (number of k-points)). Afterwards, the density matrix is transformed back to the $\mathbf{k}$-dependent orbital basis in order to calculate the new pseudospin vectors. Via the new vectors an updated Hamiltonian can be defined. This loop is repeated until the intended convergence of the magnetic order parameter $|m_{new} - m_{old}| < 10^{-15}$ is reached. The self-consistent procedure is implement as function 3 of Appendix B.1.

In the following, the equilibrium phases in dependence of the Hubbard U are investigated for a fixed hopping. For large interactions U, the system is found in an antiferromagnetic insulating phase with an all-in/all-out pseudo-spin structure. Importantly, this symmetry of all four pseudospins of the unit cell pointing towards or opposite to the zone center preserves inversion symmetry. This is imperative for the potential emergence of a time-reversal symmetry-broken Weyl phase. In thermal equilibrium, the two microscopic parameters t_σ and U adjust the magnetic order parameter and thus the overall electronic and magnetic phase of the system, respectively (see Fig. 1a of Ref. [1]). Starting from strong correlations, a decreasing U yields a reduction of the magnetisation that is accompanied by a phase transition from the antiferromagnetic insulating (AFI) to an antiferromagnetic WSM phase. This topological Weyl phase is indicated by a closing of the energy gap at the L-point via the emergence of a pair of Weyl cones. The order of the phase transition depends on the σ-hopping integral t_σ. For the chosen parameter subspace it is of first order (Fig. 1b of Ref. [1]). Driven by a further reduction of the the magnetisation by reduced interactions, the Weyl points move towards the Γ-point, where, by their mutual annihilation, the system exhibits a second order phase transition to a topologically trivial, paramagnetic metallic (PMM) phase. This transition is generally indicated by a Kramer's degeneracy of the bands and

a quadratic band-touching at Γ.

With the aim to dynamically induce a phase transition from the experimentally favoured AFI ground state to the topologically interesting Weyl semimetallic phase, an initial state with strong interactions is chosen. It is indicated by a red square in the AFI sector of Fig. 1a of Ref. [1]. Proceeding from this value, the interaction parameter is instantaneously quenched to three different smaller values which are indicated by colored arrows in Fig. 2b (Ref. [1]). The corresponding thermal equilibrium states for these interaction energies lie both within the WSM for the first and within the PMM phase for the lower two values. These interaction quenches are motivated by the TDDFT+U calculations presented in Fig. 2a and Fig. 2b of Ref. [1]. It is shown that the self-consistently calculated effective interaction $U_{\mathrm{eff}}(t)$ and the magnetisation $m(t)$ decrease on the ultrafast time scale of a high-intensity sub-gap femtosecond laser pulse. The change in $U_{\mathrm{eff}}(t)$ increases with the intensity of the light pulse. In the model, the effect of a strong pulsed driving is included as an instantaneous quench, which due to the extremely short time scale (≈ 15 fs) is an adequate approximation.

Numerically, a quench of the effective Hubbard interaction U results in a new energy eigenbasis of the Hamiltonian. This gives rise to a nontrivial time evolution of the initial density operator ρ, which does not commute with the Hamiltonian matrix anymore. The change of the density operator is associated with a change of the magnetic order parameter, which becomes time-dependent ($m \rightarrow m(t)$,). The dynamics of the total density operator are described by the von-Neumann equation, the matrix equivalent of the time-dependent Schroedinger equation. The non-unitary dynamics of a reduced system, which is coupled to a fermionic bath, can be described by a Lindblad master equation [67]. By definition, its time-propagation preserves trace, hermiticity and positivity of the reduced system density matrix. Here, an instantaneous eigenbasis approximation (see Ref. [68]) is used in which the coupling to the bath is defined in the instantaneous energy eigenbasis of the time-dependent Hamiltonian. By allowing energy and particle exchange with the reservoir, the dissipative term of Eq. 13 (Ref. [1]), induces decoherence and relaxation of the system on a timescale of the inverse coupling, $1/\Gamma_0$. The total energy, E_{tot}, is not a conserved quantity after the quench. The computation of the temporal change of the reduced density matrix, $\partial_{\mathrm{t}}\rho_{\mathrm{t}}(\mathbf{k})$, is implemented by function 4 (see Appendix B.1). In the first part the temporal change due to unitary dynamics is calculated. The second part calculates the non-unitary change of the density matrix, which is induced by the system-bath coupling.

The time-dependent differential equation is numerically solved by a linear multi-step Adams-Bashforth predictor-corrector method, shown in Eq. 11-12 of Ref. [1]. The great advantage of this method is that already calculated steps are used for the computation of the subsequent time step. This reduces the overall computational costs. As the density matrix for a subsequent time step, $\rho_{t+1}(\mathbf{k})$ is calculated with help of the last two steps $\rho_{\mathrm{t}-1}(\mathbf{k})$ and $\rho_{\mathrm{t}}(\mathbf{k})$, the density matrix has to be stored in memory only for these three steps at the same time. Time-dependent

observables

$$\left\langle \hat{O} \right\rangle_t = \sum_{\mathbf{k}} \mathrm{Tr} \left\{ \rho_t(\mathbf{k}) \hat{O} \right\}$$

are calculated on the fly in order to minimize the memory costs. After every time step, the pointers to each of the three matrices are exchanged in a cyclic way and are subsequently refined by the method. In order to avoid nonphysical particle currents, the chemical potential of the bath-correlation functions is dynamically adjusted by $\mu_{\mathrm{t+1}}^{\mathrm{Bath}} = \mu_{\mathrm{t}}^{\mathrm{Bath}} \cdot N_{\mathrm{t}}/N_{\mathrm{t+1}}$. That way, the total particle number N of the reduced system is kept constant. The propagation scheme is implemented as function 5, listed in Appendix B.1.

In Fig. 2c (Ref. [1]) the quench-induced dynamics of the magnetic order parameter are shown. As expected for the interaction with a high intensity laser pulse, the system is found in an excited state with an excited amplitude mode of the magnetic order parameter (dashed lines). In case of a finite system-bath coupling (solid lines) this oscillation is strongly damped by electronic relaxation.

The low-temperature heat bath has two major effects. First, by the dissipation of energy into the bath it enables the quench-heated system to relax. Second, by particle transfer in and out of the reservoirs the electrons have the possibility to thermally redistribute. In the long-time limit (which is not calculated here) the density matrix would again reach a thermal ensemble with the magnetisation and energy corresponding to the respective U equilibrium state. As a first important result, a reduced but finite magnetisation $m(t)$ is found shortly after all three quenches. By comparing the total energy of the quenched states with the temperature-dependent total energies, obtained from the same U values in equilibrium, effective temperatures for the nonequilibrium states can be extracted. As shown in Fig. 2d of Ref. [1], these extracted effective temperatures lie, for the two stronger quenches, above the limit for a finite magnetisation in equilibrium. This indicates a nonthermal character of the corresponding transient nonequilibrium states, which is the second important result of this work. This nonthermality has two important consequences. First, Weyl fermions emerge for higher effective temperatures than in thermal equilibrium. This is expected to reduce the amount of necessary fine tuning in the experiment. Second, as discussed later in more detail, delayed thermalisation increases the lifetime of the transient Weyl states, which provides an increased time window for their potential detection.

The time-dependent bulk band structure is probed by time- and angle resolved photo emission spectroscopy. The single-particle removal spectrum is encoded in the two-times lesser Greens function, which is, due to the non-unitary real-time evolution, calculated in an approximate way after the actual time-propagation of the reduced density matrix. The L-Γ high-symmetry path on which the Weyl points appear is sampled by a finite set of k-points. With knowledge about the time-dependent magnetisation and thus the time-dependent Hamiltonian, the density matrices for this small set can be propagated via the multi-step method. The initial density matrix is

again defined by Fermi-weighted occupations in the initial energy eigenbasis. The k-dependent two-times lesser Greens function is then approximated by a unitary propagation (see Eq. 17 of Ref. [1]), of the density matrix from each point in time in both time direction t and t', as outlined by Eq. 16 (Ref. [1]). The number of time steps used for the unitary propagation is reduced by one order compared to the original propagation. Despite their unitary character, the information about the dissipative bath is still encoded in the propagators by the dependency of the Hamiltonian on the time-dependent order parameter, $m(t)$. For the calculation of the photocurrent (last Eq. of Ref. [1]), the trace of the lesser Greens function is required. The trace for each pair of time coordinates t and t' of the lesser Greens function is implemented as function 6 (see Appendix B.1).

The momentum- and frequency-dependent photocurrent can be calculated from the lesser Greens function by a double-time integration with a Gaussian shaped filter function. This filter function represents the time-envelope of the probe pulse. In the code, it is implemented by function 7. As the Greens function can be computed independently for different momenta and energies, a parallel calculation using MPI (message passing interface) is straightforward. As shown in Fig. 3b-d (Ref. [1]), the system is found in a nonequilibrium Weyl semimetallic phase for all three quenches. This topologically nontrivial phase is indicated by the appearing of Weyl cones in the bulk band structure between L and Γ. This emergence of nonthermal WSM order by ultrafast optical control of the magnetic order parameter is the central result of this work.

In the last part of this work the minimum lifetime of the photoinduced Weyl fermions is investigated. In a real experiment the pump-induced reduction of the effective electronic interaction U and thus of the magnetic order is, due to relaxation processes, only a transient effect. In particular, the coupling of the electronic subsystem to the environment (substrate, phonons, etc.) provides an important dissipative channel in real materials. Therefore, a continuously time-dependent Hubbard parameter $U \to U(t)$ is assumed. It starts at the original value in the AFI phase, decreases to a minimum of the strongest quench value, and finally relaxes back to its initial value (see Fig. 4a of Ref. [1]). This way a dissipative case is realised, where the renormalisation of $U(t)$ instantaneously follows a hypothetical femtosecond pump envelope. The magnetisation dynamics are depicted in Fig. 4b (Ref. [1]). The magnetisation $m(t)$ reaches the initial value about 50 fs later than the time-dependent interaction $U(t)$. This persistence of time-dependent effects beyond the driving time scale is the final important finding of this project. This effect is considered in more detail by calculating time-resolved ARPES measurements at various times before, during and after the temporal change of $U(t)$. The probe at $t_p = 150$ fs clearly demonstrates this delay-effect (see Fig. 4g of Ref. [1])) by the persistence of the Weyl cone and thus the nonequilibrium WSM phase outside the FWHM (full width at half maximum) of $U(t)$. This increased lifetime of the transient WSM phase beyond the driving-timescale is governed by the nonthermal character of the nonequilibrium states, which hinders the system to thermalise rapidly.

In summary, it is shown by a combination of TDDFT+U and mean-field magnetic model calculations that by strong laser-induced quenches of the local electronic interactions a transient Weyl semimetallic phase can be induced in pyrochlore iridates. The nonthermal character of the transient phase allows the stabilisation of Weyl fermions in a wide region of effective temperatures and beyond the time scale of the pump duration.

6.2 Publication II

Charge density wave melting in one-dimensional wires with femtosecond subgap excitation This project is a theoretical investigation of the experimental results presented in publication **II** (Ref. [2]). Within the experiment, the laser-induced melting of a CDW phase by a mid-IR (mid-infrared) driving pulse in one-dimensional indium wires is probed. The details of the numerical approach, which led to the presented model results (Ref. [2]), are analyzed. The referred functions are listed in Appendix B.2. A complete version of the code can be accessed at https://github.com/Fizztopp/InSi.git.

In the experiment, the laser-induced phase transition is tracked by tr-ARPES measurements of the time-dependent band structure before, during, and after the pump pulse (see Fig. 2a-e of Ref. [2]). The melting dynamics are analysed by an investigation of the spectroscopic data, which is presented in Fig. 3a-d (Ref. [2]). At a critical field strength of 0.9 MV/cm a time-dependent shift of spectral weight into the CDW gap on a time scale of less then 300 fs indicates an ultrafast laser-induced transition by photo-doping of charge carriers above the energy gap. The theoretical investigations, which are presented in the following, explore these dynamics within a model simulation.

For the nonequilibrium model calculations, an effective DFT-fitted tight-binding Hamiltonian, as originally introduced in the work of Jeckelmann et al. [57], is used. The real space Hamiltonian includes local on-site potentials and the nearest-neighbour hopping within and between two inner and two outer Indium chains that build the wire. For each In-atom one Wannier orbital is considered. Generally, by an appropriate choice of the hopping parameters, the single-particle electronic properties of both the high-symmetry metallic phase and the broken-symmetry CDW phase can be described. In agreement with the experiment, the starting point is the low-temperature insulating phase. Here, an increased 4×2 unit cell has to be employed in order to restore translational symmetry. Its eight-atom basis is defined by the vectors $\mathbf{b_1} = (0, 0)$, $\mathbf{b_2} = (1/2, \sqrt{3}/2)$, $\mathbf{b_3} = (1, \sqrt{3})$, $\mathbf{b_4} = (3/2, 3\sqrt{3}/2)$, $\mathbf{b_5} = (5/2, 3\sqrt{3}/2)$, $\mathbf{b_6} = (2, \sqrt{3})$, $\mathbf{b_7} = (3/2, \sqrt{3}/2)$, and $\mathbf{b_8} = (1, 0)$. The basis vectors are defined in units of the lattice constant of the uniform phase, $a_0 = 3.84$ Å. The unit cell together with the electronic hopping is depicted in Fig. 7 (see supplement material of Ref. [2]).

As stated in the manuscript, slightly adjusted electronic parameters are used in order to reproduce the experimentally measured equilibrium low-temperature ARPES bands, in particular

the reported 300 meV band gap at the boundaries of the reduced zone. Periodic Born-von Karman boundary conditions within the x-direction yield an one-dimensional reciprocal unit cell $[-\pi/2a, \pi/2a)$, which is sampled by a grid of 1024 k-points. The mid-infrared laser pulse is implemented via a time-dependent external gauge field, $\mathbf{A}(t) = A_{\max} p_{\sigma_p}(t) \sin(\Omega t)\mathbf{e}_{\mathrm{x}}$, via Peierls substitution. Here, the femtosecond pulse is included by a Gaussian envelope $p_{\sigma_p}(t) = \exp(-(t - t_0)^2/(2\sigma_p^2))$. The parameters of the external driving field are adjusted to the laser field at the sample. The electronic Hamiltonian is implemented as function 8 (see Appendix B.2). In the first part, the diagonal elements, which correspond to the local potentials, are set. In the second part the hopping elements are set. These include intracell and intercell hopping processes. By diagonalisation of the Hamiltonian matrix, the band structure shown in Fig. 8 (see supplemental material of Ref. [2]) is calculated.

Since for the estimation of the total absorbed energy a closed system is considered, the propagation of the system density operator is unitary. As the Hamiltonian does generally not commute with itself at different points in time, a correct time-ordering has to be considered. This is achieved by a discretisation of the real-time axis and a consecutive multiplication of the evolution time-step operators. Using the Euler mid-point rule, the unitary propagator for one time step δt is given by $U_{\mathbf{k}}(t + \delta t, t) = \exp[-iH_{\mathbf{k}}(t + \delta t/2)\delta t]$. The initial density operator is set in the eigenbasis of the initial Hamiltonian. The Fermi functions define the diagonal matrix elements. In agreement with the experimental parameters the initial temperature is set to $T = 40$ K. The time-dependent density matrix at each time step is calculated by $\rho(\mathbf{k}, t + \delta t) = U_{\mathbf{k}}(t + \delta t, t)\rho(\mathbf{k}, t)U_{\mathbf{k}}^{\dagger}(t + \delta t, t)$ in the k-dependent orbital basis. The time-propagation of the density matrix is implemented as function 9 (see Appendix B.2). From the propagated density matrix, the time-dependent total energy of the system per unit cell can be calculated by $E_{\mathrm{cell}}(t) = 2/N \sum_{\mathbf{k}} \mathrm{Tr}\{\rho(\mathbf{k}, t)H(\mathbf{k}, t)\}$. The factor of two includes the spin degeneracy, which is crucial for a comparison of the absorbed energy with the condensation energy, reported by DFT investigations [69].

The time-dependent total energy is depicted in Fig. 4a of Ref. [2] for different driving amplitudes. In the code, the vector potential is implemented in units of $1/a_0$ of the inverse lattice constant of the 4×1 unit cell. The peak electric field strength can be calculated by $E_{\max} = \Omega A_{\max}$. In this simplified model, the amount of absorbed energy is approximated by the difference between the final total energy and the initial total energy, $\Delta E = E_{\mathrm{f}} - E_{\mathrm{i}}$. A log-log plot of the absorbed energy as a function of the peak driving intensity shows a quadratic dependency in a region close to the condensation energy, $E_{\mathrm{cond}} = 32$ meV (Fig. 4b of Ref. [2]). This quadratic dependence indicates two-photon absorption as the dominant absorption process. This agrees with the Keldysh parameter ($\gamma = 1.6$), which is calculated from the experimental parameters. The Keldysh parameter is defined by the square root of the ratio of the energy gap and the ponderomotive energy ($\gamma = \sqrt{E_{\mathrm{gap}}/U_{\mathrm{p}}}$). This ratio gives an estimated distinction between the

multi-photon absorption regime ($\gamma < 1$) and the tunneling-ionisation regime ($\gamma > 1$). The peak electric field amplitude of $E_{\max} \approx 1$ MV/cm that is necessary to reach the condensation energy and thus induce a melting of the charge-density-wave order is in good agreement with the experimentally found threshold of $E_{\max} \approx 0.9$ MV/cm.

The key-finding of the experiment is the identification of multi-photon absorption as dominant process for the CDW melting. Supporting this interpretation, by identifying two-photon absorption as dominant melting process, is the central result of this theoretical investigation.

6.3 Publication III

Topological Floquet engineering of twisted bilayer graphene After having explored the interaction-controlled topology in pyrochlore iridates with magnetic mean-field model simulations (Ref. [1]), in this project the light-induced topological properties of weakly-interacting intermediate-angle twisted bilayer graphene are investigated on basis of the Floquet formalism. The details of the numerical approach that led to the results, presented in publication **III** (Ref. [3]), are analyzed. The referred functions are listed in Appendix B.3. A complete version of the code can be accessed at `https://github.com/Fizztopp/TBG_FLOQUET.git`.

The employed tight-binding model Hamiltonian (Eq. 1 of Ref. [3]) describes the local potentials and the electronic hopping between the carbon atoms, which define the crystal lattice. The computation of the atomic positions within the angle-dependent real-space supercell is the first critical task in this project. The original `Fortan90` code for the calculation of the atomic positions within the bilayer graphene supercell was provided by Lede Xian. Here, a reformulated `Python` version is used. A commensurate supercell can be represented by the integer tuple (n, m), which defines the two commensurate supercell vectors $\mathbf{t} = n\mathbf{a_1} + m\mathbf{a_2}$ and $\mathbf{t}' = -m\mathbf{a_1} + (n+m)\mathbf{a_2}$ of the two layers. The vectors $\mathbf{a_1}, \mathbf{a_2}$ define the two-atom single-layer basis. The supercell has a total number of sites, $N = 4(n^2 + nm + m^2)$. More details about the crystal lattice can be found in the works of Laissardière et al. [62, 63]. If not explicitly stated otherwise, a supercell with the indices $(n, n+1) = (4, 5)$ is used. This supercell consists of total number of $N = 244$ atoms with an intermediate twist angle of $\Theta \approx 7.34°$. Here, 'intermediate' means that the twist angle lies above the highest magic angle ($1.05°$) and below $30°$. The calculation of the atomic positions is implemented by function 10 (see Appendix B.3). The resulting atomic Moiré superlattice structure is shown in Fig. 1a of Ref. [3].

After the computation of the atomic positions within the supercell, the electronic Hamiltonian can be constructed. An effective Hamiltonian is employed, which only takes account of the electrons in the p_z-orbitals. These lie energetically close to the Fermi surface and are well separated from the other orbitals [62]. In contrast to the magic-angle regime, for intermediate twist angles the kinetic energy of the charge carriers, which is directly connected to the electronic bandwidth, is the dominant energy scale [70]. As correlation effects are in this regime

of minor importance [70–72], electronic interactions are neglected here. The resulting noninteracting Hamiltonian is bilinear and can be represented by a quadratic matrix. Again, using the translational symmetry of the Bravais lattice and introducing periodic Born-von-Karman boundary conditions, the Hamiltonian is transformed to the momentum-dependent orbital basis. An external time-dependent gauge field $\mathbf{A}(t)$ is introduced by Peierls substitution. This field adds time-dependent phase factors to the hopping matrix elements (see Eq. B1 of Ref. [3]). The components of the time-dependent gauge potential are implemented as functions 11 (see Appendix B.3). The field amplitudes `Ax/Ay/Az_peierls` and the driving frequency `w_peierls` are defined separately by global constants. Via the gauge field, the Hamilton operator becomes explicitly time dependent. The Hamiltonian matrix is generated by function 12 of Appendix B.3. The first and second part of the function set the bottom and top layer matrix elements. The values for the backgate voltage `VV` and the sublattice potential `dgap` are defined by globally set constants. The p_z-orbitals within the same plane are coupled by $V_{pp\pi}$-hopping only. The last part describes the interlayer hopping, which also includes $V_{pp\sigma}$-hopping elements. By running the loops over the indices `m` and `n`, the hopping to the eight next-neighbour unit cells is considered via translational shifts by the Bravais lattice vectors.

In order to investigate the electronic groundstate properties of the zero-field Hamiltonian, the momentum-dependent eigenenergies along the Γ-K-M high-symmetry path through the Brillouin zone are investigated. The relative twist angle between the two sublattices results in a geometrically alternating arrangement of AA-stacked and AB-stacked regions [62, 63]. As in the AA-regions the atoms are stacked exactly on top of each other, the effective interlayer hopping is much stronger than in the AB regions. This periodic modulation of the effective coupling strength locally confines the electronic density of states close to the Fermi level within the AA-regions. This results in an angle-dependent reduction of the bandwidth that is accompanied by a renormalisation of the Fermi velocity [62, 63]. In Fig. 2b of Ref. [3], which compares the equilibrium band structures of monolayer and intermediate-angle twisted bilayer graphene ($\Theta - 7.34°$), the reduction of the electronic bandwidth and the Fermi velocity is shown. In Fig.2c (Ref. [3]) the angle-dependent renormalisation of the bandwidth is depicted.

In order to investigate the topological properties of the initial Hamiltonian, the momentum-local band Berry curvature is calculated. The Berry curvature at a discrete point in momentum space can be defined by the accumulated phase along the eigenstates of an infinitesimally small loop around that point [73]. This phase defines the Berry phase. Divided by the enclosed area, this yields the momentum-local Berry curvature. A discretised formula for the Berry curvature is defined by Eqs. C1 and C2 (Ref. [3]). The details of the discretised loop are shown in Fig. 8 of Ref. [3]. The numerical computation of the Berry curvature is implemented by function 13 (see Appendix B.3). The starting point of the loop through momentum space is defined by `k0`. After the calculation of the eigenvectors along the loop, the Berry phase for each band is calculated

and divided by the enclosed area in momentum space.

In the spirit of the Haldane model [61], the equilibrium Berry curvature of the two valence bands in close proximity to the Dirac points is investigated. The local Berry curvature for different choices of inversion-symmetry breaking local potentials is depicted in Fig.2 of Ref. [3]. The curvature has a strong peak at the Dirac points. The integrated valence band Berry curvature close to the Dirac points vanishes independently of the chosen potential. In analogy to monolayer graphene the system is a topologically trivial insulator with an Chern number $C = 0$. Importantly, by changing the symmetry and amplitude of the local potentials, the Berry curvature of the valence bands can be switched between a finite value and zero within one valley. The topologically trivial nature of the equilibrium system for twist angles above the magic-angle regime is the first important result of this work.

In the following, the effect of a time-periodic external gauge field on the electronic states is investigated. The vector potential and thus the electric field imprints its periodicity onto the solutions of the time-dependent Schrödinger equation. Exploiting this discrete translational symmetry by one time-period $T = 2\pi/\Omega$, where Ω is the frequency of the drive, the time-dependent Hamiltonian can be mapped onto an effective and time-independent Floquet Hamiltonian [13, 74–76], as described by Eqn. B2 and B3 in the published work [3]. By diagonalisation of the truncated Floquet matrix, the photon-dressed eigenstates and their corresponding Floquet eigenenergies can be computed. The calculation of the Floquet matrix is implemented as function 14 (see Appendix B.3). The Floquet matrix has a block-structure, where the indices `m` and `n` define the photon sector and the indices `i` and `j` identify the atomic sites. Following Eq. B2 of Appendix B in [3] the integration over one time period T is performed. Afterwards, the eigenvectors and eigenenergies of the Floquet matrix are computed. By diagonalisation of the original Hamiltonian, its eigenvectors are computed. Finally, the squared overlap of the Floquet states with the original eigenstates is computed. The overlap for each band and quasimomentum lies within the real interval [0,1]. It offers the possibility to identify photon-dressed states that emerge from the undressed ('bare') original bands. The Floquet band structure for a circularly polarised driving field with a frequency tuned to the bandwidth of the low-energy manifold at the Γ point is depicted for different choices of on-site potentials (see Fig. 3a of Ref. [3]). The major effect of the chiral driving field is the breaking of time-reversal symmetry. This opens an energy band gap at the Dirac points. Additionally, smaller band gaps open at quasi-momentum points different from K and K'. These side gaps result from the resonant coupling of lower and higher lying bands through the driving field.

The topological properties of the Floquet Hamiltonian and thus of the light-dressed states are investigated in the same way as for the equilibrium Hamiltonian. For the calculation of the Berry phase the eigenstates of the original Hamiltonian have to be replaced by the Floquet eigenstates. The local Berry curvature of the Floquet bands in close proximity to the Dirac points

is depicted in Fig. 4 of Ref. [3]. The major effect of the external driving field is an exchange of Berry curvature between the valence and conduction bands of one Dirac point. This results in a finite integrated Berry curvature of the valence bands close to the Fermi energy, which corresponds to an effective winding number analogous to a Chern insulator with Chern number, $C = 4$. The closing and subsequent reopening of the Dirac-point energy gap upon varying the circular driving field amplitude, which is accompanied by a topological phase transition into a Chern-like phase, is the central result of this work. The phase transition can be controlled by the backgate voltage. For a finite backgate voltage, a critical field strength is necessary to reach the topologically nontrivial phase. The tunability of the phase transition becomes more obvious in Fig. 5c and d (Ref. [3]) in which the Floquet topological phase is depicted as a function of the driving amplitude and the local potential. In Fig. 4a (Ref. [3]), the field-induced gap is plotted as a function of the driving amplitude. For single-layer graphene, the high-frequency expansion of the Floquet Hamiltonian shows a quadratic dependency of the topological gap at the Dirac points on the Fermi velocity, as shown by Aoka et al. [13]. Interestingly, here almost the same scaling with the bare Fermi velocity is found for the intermediate angle of $7.34°$. In Fig. 4b it is shown that for smaller twist angles the size of the gap lies in-between the values expected from the bare monolayer Fermi velocity and the value which is naively calculated from the angle-dependent renormalised velocity. This intermediate scaling can be understood by the in-plane polarisation of the driving field, which is only weakly affected by the size of the effective interlayer coupling. This is the final important result of this work.

In conclusion, the presented work highlights laser-light as a viable tool for the effective engineering of the topological properties of intermediate-angle twisted bilayer graphene. Starting from topologically trivial equilibrium, it is shown that the breaking of time-reversal symmetry by a circularly polarized laser-field offers an ultrafast pathway to a topological phase with a nonvanishing valley Berry curvature close to the Fermi energy. The closing and subsequent reopening of the gap is tracked by the Floquet-band structure. Furthermore, it is shown that the critical field strength, which is necessary to induce a topologically nontrivial phase, can be tuned to finite values by a backgate voltage. As a final result it is shown that the size of the field-induces energy gap is higher than the naive expectation from the renormalised Fermi velocity.

7 Comprehensive discussion

In the work at hand, three published projects are presented that analyse different aspects of ultrafast laser-induced control over nonequilibrium phases of matter in different materials, namely pyrochlore iridates, indium wires, and twisted bilayer graphene. For these materials, tailored pathways are provided, how to dynamically manipulate their intrinsic microscopic properties in order to engineer their macroscopic response.

Pyrochlore iridates are correlated materials. In this kind of materials particle interactions set the dominant energy scale. The presented TDDFT simulations show that this energy scale can be accessed by the laser-control of the dynamical electronic screening. In the presented model calculations, the ultrafast manipulation of the effective Hubbard repulsion offers a tuning knob to dynamically change the magnetic order parameter, and to ultimately induce a topological Weyl semimetallic phase. As an instantaneous quench is a maximally nonadiabatic process, it is intrinsically accompanied by strong heating effects. The extracted effective temperatures of the nonequilibrium states clearly indicate the nonthermal character of the transient Weyl phase. While this property of nonthermality is not imperative for the shown emergence of Weyl fermions, it holds important implications for a potential experimental realisation of the presented pathway. First, it is found that Weyl fermions can be stabilised in a wide region of effective temperatures and interactions. This indicates that, in the proposed nonequilibrium experiment, precise fine-tuning of the pump-field might not be necessary. This facilitates the search for sweet spots of minimal absorption. Moreover, heating effects seem to be less destructive for a nonequilibrium Weyl phase than in thermal equilibrium. Second, as discussed within the manuscript, the trapping in a nonthermal state can lead to delayed thermalisation of the order parameter. Therefore, the time window for a potential detection of Weyl fermions by e.g. tr-ARPES measurements is ultimately limited by relaxation effects, which are induced by the coupling to the environment. The laser-induced reduction of the electronic correlations takes place on a time scale of tens of femtoseconds. Assuming phononic decay as a dominant dissipative channel, the relaxation of the correlations can be estimated to take place on a time scale of hundreds of femtoseconds up to picoseconds. This increased life time of the transient WSM phase allows the utilisation of very short pump pulses. This way pump-induced heating can be significantly reduced. This is an important advantage compared to Floquet-induced phase changes in weakly interacting materials, where all field-induced effects vanish with the pump field. The presented findings of this project emphasise the important role of the ultrafast control of electronic interactions as a novel and promising route towards the engineering of topological properties in correlated materials. As discussed by Berke et al. [77], the main limitation of the employed Hartree-Fock Hamiltonian is the omission of fluctuations. While in the 3D materials fluctuations are often of minor importance, it would be interesting to investigate their impact on the nonequilibrium stabilisation of Weyl

fermions by methods beyond the employed mean-field ansatz and in nonequilibrium experiments. A major difficulty regarding the experimental realisation of the proposed experiment is the material structure of pyrochlore iridates. The quality of ARPES measurements crucially depends on the availability of a well-cleaved surface. Apparently this is very challenging to realize experimentally in these materials. Particularly, in a nonequilibrium setup, due to naturally finite time windows, the quality of the probe material might be important.

In a recent investigation of the two-dimensional transition metal dichalcogenide T_d−$MoTe_2$, a crucial role of local Coulomb interaction for the topological properties of the material was shown. By a combination of SX-ARPES (soft x-ray ARPES) measurements and DFT+U simulations a correlation-driven novel hybrid Weyl semimetallic phase was proposed for this material. Signatures of a pump-induced Lifshitz transition were experimentally found via tr-ARPES measurements by Crepaldi et al. [78]. These works support the important role of interactions within the field of topological control.

For the Peierls transition of one-dimensional indium-wires electronic interactions are expected to be of minor importance. In equilibrium, the condensation energy E_{cond} defines the dominant energy scale for the metal-to-insulator transition here. It is a measure for the amount of energy which is saved due to the transition to the low-symmetry CDW phase. In a simplified picture, this transition can be reversed by photodoping of quasi-particles above the energy band gap, as the amount of saved energy in the electronic system is reduced. Within the presented simulations, the condensation energy is compared to the time-dependent change of total electronic energy due to a sub-resonant external driving field. This comparison yields an approximate threshold for the driving amplitude that is necessary to melt the CDW order. Moreover, the relation between the change in energy and the field intensity allows a qualitative interpretation of two-photon absorption as the dominant process. While the good agreement with the experimental findings generally validate this ansatz, the used approximation neglects several effects. These effects might have an impact on the quantitative details of the final result. Generally, the observed ultrafast phase transition is a collective response of the total system, including electronic and nuclear degrees of freedom. Changes in the nuclear degrees of freedom are neglected in the dynamical calculations of the presented work. Moreover, the condensation energy as well as the CDW gap generally depend on the electronic density which is a time-dependent object in the multiband simulations performed here. As the external driving field results in an increased effective electronic temperature, the CDW gap and the condensation energy are expected to decrease during the pump. In this view a slightly reduced threshold for the peak electrical field can be expected. These issues are investigated in more detail in a subsequent project via an optically driven Su-Schrieffer-Heeger model with Ehrenfest dynamics of the nuclear system. Within this approach the lattice order is tracked via the atomic displacement which impacts the electronic energy landscape similarly to the magnetic order parameter in the pyrochlore model.

Further details and preliminary results are presented in Sec. 8.1.

Twisted bilayer graphene is the third material under investigation. In this material the internal energy landscape crucially depends on the twist angle. In the magic-angle regime the electronic bandwidth is reduced to a few meV and the Fermi velocity drops to zero. In this regime of strongly reduced kinetic energy the electronic interaction becomes a dominant energy scale. This was demonstrated by the measurement of superconductivity in close proximity to a strongly-correlated insulating phase at a very low temperature [65, 66].

While the electronic and topological properties at these tiny angles are still heavily debated, the investigations in this thesis focus on the intermediate angle regime at twist angles larger than the highest magic angle. In this regime the kinetic energy dominate over correlation effects. For this reason, the electronic and topological properties of the system are well described in terms of noninteracting Bloch states. The kinetic energy scale can be controlled by the twist angle. This offers the opportunity to tailor the electronic band structure in order to reduce unintended heating effects. At least for intermediate twist angles there exists no simple tuning knob to adjust the topological properties in equilibrium. In the presented work it is demonstrated that a circularly polarised laser field allows direct access to the topological properties of twisted bilayer graphene. By breaking time-reversal symmetry, a controllable nonequilibrium phase transition towards a topologically nontrivial phase is realised. From the Berry curvature of the Floquet-dressed states a winding number analogous to a Chern (C=4) insulator is found close to the Dirac points. Within an ultrafast Hall-current experiment this presumably allows the measurement of a more-or-less quantised Hall conductivity. However, as discussed before, the Chern number is an integrated object of the Berry curvature of the occupied bands. Thus, only in the case of vanishing time-dependent fields and resonant electronic excitations, the system strictly corresponds to a Chern insulator. Despite the possibility of tuning the electronic energy scales, population effects can in reality never be entirely avoided. This is not taken into account by the employed Floquet description, since only the effect of the field on the electronic states but not their occupations is incorporated here. In the static Floquet picture this would mean that the Berry curvature of the smaller side band gaps, which result from the resonantly coupled states, might obtain a nonzero weight for the computation of the Chern number. This issue of electronic heating and topology is investigated by means of a dissipative real-time calculation in a follow-up project, introduced in Sec. 8.2. Finally, the scaling of the light-induced topological gap with the driving amplitude might be interesting for envisioned nonequilibrium experiments at the magic angle. In this set-up, despite a vanishing Fermi velocity, a finite gap might be expected.

In a subsequent work, the Floquet-band topology of twisted-bilayer graphene in the magic-angle regime was investigated [79]. Within that work, the predictions about the topology of the high-frequency circularly driven system confirm the results of the work at hand. Moreover, very recently the Floquet-engineering of nontrivial flat bands near the magic-angle regime was

discussed by Katz et al. [80]. These works highlight the viability of Floquet-engineering for the nonequilibrium control of quantum materials.

Taken together, the here presented work supports the outstanding role of ultrafast experiments as a platform for the tailored engineering of material properties on demand. It is shown that pulsed laser light provides a precise tuning knob to dynamically access the intrinsic energy scales of a material, to manipulate them, and thus to ultimately gain control over the macroscopic properties of matter. Moreover, the nonequilibrium aspect of dynamically induced phase transitions can lead to new states of matter with transient properties which can not be deduced from equilibrium intuition.

Apart from purely scientific insights, the ultrafast control of material properties has an increasing applied importance which is fostered by the rapid technical progress in nanoscale electronics and quantum computation circuits. For example, laser-controlled optoelectronic switches might in the near future complement conventional transistors that are naturally limited by the time scales of their macroscopic current dynamics. The presented insight of this work provide an important contribution for fostering a fundamental understanding about the prerequisites for ultrafast control of existing and future quantum materials.

8 Subsequent projects

In this section selected followup projects are introduced and first results are discussed. As this is work in progress, the shown data is not revised via a peer-review process and should generally be understood as preliminary.

8.1 SP II: Ehrenfest dynamics of the optically driven Su-Schrieffer-Heeger model

This project is a continuation of the work presented in publication **II** (Ref. [2]). In this follow-up project the time-dependent interplay between electronic and nuclear order as well as its impact on the melting dynamics is investigated. A complete version of the latest version of the code can be accessed at https://github.com/Fizztopp/SSH.git. We use units where $e = \hbar = c = 1$. Starting point is the Su-Schrieffer-Heeger Hamiltonian, which was originally introduced for the exploration of soliton excitations in polyacetylene [81]. Assuming a perfectly uniform dimerisation, the tight-binding Hamiltonian is of the general form

$$\hat{H}_{\mathsf{SSH}} = -2\sum_{n}\left[t_0 + 2\alpha(-1)^n u\right](\hat{c}^{\dagger}_{n+1}\hat{c}_n + \hat{c}^{\dagger}_{n}\hat{c}_{n+1}) + 2NKu^2 + \frac{N}{2M}p^2.$$

For a vanishing coupling between the electronic and the nuclear subsystem, $\alpha = 0$, the electronic energy is described by a nearest-neighbor hopping term with a bare hopping parameter, t_0. The nuclear degrees are described by a set of N classical harmonic oscillators with a spring energy, Ku^2, and a kinetic energy, $p^2/(2M)$, per oscillator. The variable u defines the nuclear dimerisation, p the nuclear momentum. For a finite coupling $\alpha \neq 0$, a finite dimerisation results in a π-periodic change of the electronic hopping. This can be interpreted as a periodic modulation of the bond order. The concomitant breaking of translational symmetry can be incorporated by doubling the size of the unit cell from one to two atoms. Assuming periodic boundary conditions, this yields a reduced Brillouin zone $Z_B = [-\pi/(2a_0), \pi/(2a_0)]$, where $a_0 = 3.84$ Å defines the approximate distance between to In-atoms along the x-direction. According to Su et al. [81], the electronic Hamiltonian can then be written in the form

$$\hat{H}_{\mathsf{el}}[u] = \sum_{k\in Z_{\mathsf{B}},s}\begin{pmatrix}\hat{c}^{v\dagger}_k\\ \hat{c}^{c\dagger}_k\end{pmatrix}^{\mathsf{T}}\begin{pmatrix}-\epsilon_k & \Delta_k[u]\\ \Delta_k[u] & \epsilon_k\end{pmatrix}\begin{pmatrix}\hat{c}^{v}_k\\ \hat{c}^{c}_k\end{pmatrix},$$

where $\epsilon_k = 2J_0\cos(ka)$ and $\Delta_k[u] = 4\alpha u\sin(ka)$. The operators $\hat{c}^{v/c}_k$ refer to the valence (v) and conduction (c) band. The $\Delta_k[u]$ term induces transitions between the two bands which are strongest at the reduced-zone boundaries. The spin index s results in a trivial factor of 2 in the following. The initial value for the dimerisation u and thus for the initial state can be determined

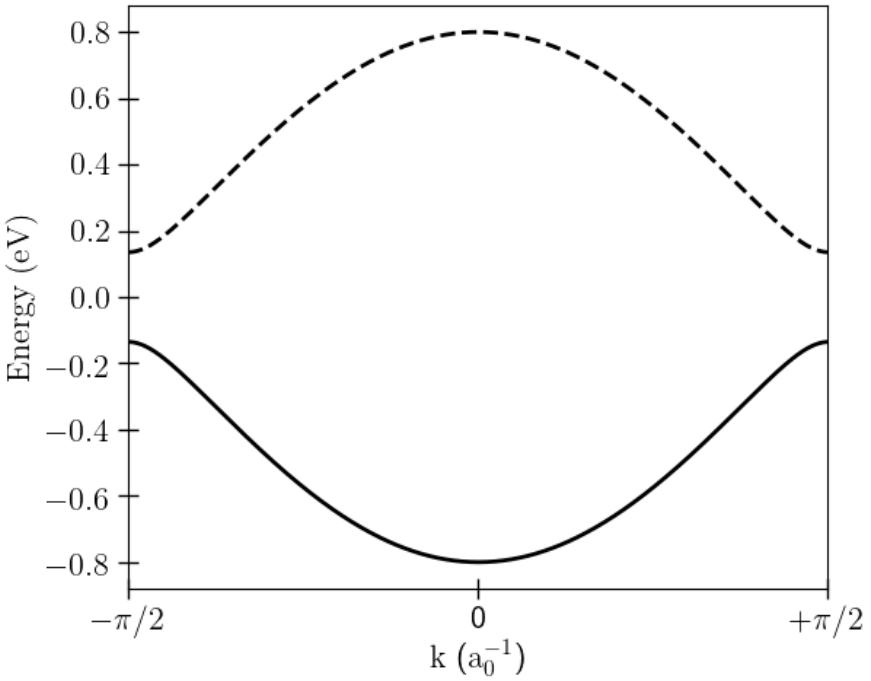

Figure 1: Equilibrium band structure of the SSH model Hamiltonian for parameters $t_0 = 0.4$ eV, $\alpha = 0.28$ eV/Å, $K = 0.55$ eV/Å^2, and $\Omega_0 = 28$ cm^{-1}.

by a self-consistent minimisation

$$\begin{aligned} \frac{\partial E(u)}{\partial u} &= \left\langle \frac{\partial \hat{H}_{\text{el}}[u]}{\partial u} \right\rangle_{eq} + 4KNu \stackrel{!}{=} 0 \\ \Leftrightarrow u &= -\frac{1}{2KN} \sum_{k \in Z_{\text{B}}} \left\langle \begin{pmatrix} \hat{c}_k^{v\dagger} \\ \hat{c}_k^{c\dagger} \end{pmatrix}^{\mathsf{T}} \begin{pmatrix} 0 & 4\alpha \sin(ka) \\ 4\alpha \sin(ka) & 0 \end{pmatrix} \begin{pmatrix} \hat{c}_k^{v} \\ \hat{c}_k^{c} \end{pmatrix} \right\rangle_{eq} . \end{aligned}$$

The self-consistent nature arises from the fact that the expectation value in the above equation is calculated on the basis of the density matrix which itself depends on u. This self-consistent calculation is implemented by the function 15 (see Appendix B.4). Referring to a system of indium wires, for all following calculations microscopic parameters, as suggested within the supplementary material of Ref. [82], are used for the model: $t_0 = 0.4$ eV, $\alpha = 0.28$ eV/Å, $K = 0.55$ eV/Å^2. In a simplified picture of an one-dimensional Peierls distortion, the bare (q=0)-phonon (q=π in original zone) frequency is set to $\Omega_0 = 28$ cm^{-1} (≈ 3.5 meV) which corresponds to the experimentally found energy of the shear mode in indium wires [69]. The band structure of the corresponding zero-temperature equilibrium Hamiltonian is shown in Fig. 1. The found dimerisation of $u = 0.12$ Å opens a gap of size $\Delta_E = 8\alpha u \approx 270$ meV at the zone boundaries. This value is in good agreement with the experimentally found energy gap for indium wires [56, 83]. As the size of the Peierls gap is proportional to the dimerisation, u can be identified as order parameter of both the nuclear and the electronic order.

Having identified the initial state, the next step is to add dynamics to the system in order

to induce the melting. In accordance to the simulations presented in project **II** (Ref. [2]), this is done via a linearly polarised gauge potential $\mathbf{A}(t) = A_{\text{max}} p_{\sigma_p}(t) \sin(\Omega t) \mathbf{e}_x$ with a Gaussian envelope $p_{\sigma_p}(t) = \exp(-(t-t_0)^2/(2\sigma_p^2))$. This time-dependent external potential is coupled to the electronic system by Peierls substitution. This introduces a time-dependent gauge shift $\hat{H}^k{}_{\text{el}}[u] \rightarrow \hat{H}^{k+A(t)}_{\text{el}}[u]$. While the closed electronic quantum dynamics are described by the Schrödinger equation (here the von-Neumann equation is solved in view of a future implementation of open dynamics) the nuclear dynamics are treated classically (Ehrenfest dynamics). In the classical equations of motion for the nuclear harmonic oscillators the electronic system appears as an additional potential. The nuclear dynamics are defined by the equations

$$\begin{aligned} \dot{u}(t) &= \frac{p(t)}{M}, \\ \dot{p}(t) &= -\frac{1}{N} \left\langle \frac{\partial \hat{H}_{\text{SSH}}[u(t)]}{\partial u(t)} \right\rangle_t - 4Ku(t). \end{aligned}$$

The nuclear dynamics act back on the electronic subsystem by adding an additional time-dependency $\hat{H}^{k+A(t)}_{\text{el}}[u] \rightarrow \hat{H}^{k+A(t)}_{\text{el}}[u(t)]$. For the solution of the electronic and the nuclear equations of motion the two-step Adams-Bashforth method is used. The propagation scheme is implemented as 16 (see Appendix B.4). An example for the resulting dynamics from a driving pulse with an energy of $\omega = 190$ meV, a peak amplitude of $A_{\text{max}} = 0.08\ a_0^{-1}$ and a FWHM of the intensity profile of 300 fs is plotted in Fig. 2. These parameters are chosen in reference to the weak-driving scenario of the indium-wires experiment. The time-dependent field induces an increase in the electronic energy, E_{el}. Since the field energy is chosen sub-resonant, this absorption is, in agreement with the former calculations [2], presumably governed by two-photon absorption. By the finite coupling to the nuclear subsystem, this excitation induces a finite force on the nuclei. This is indicated by an increasing nuclear momentum p. The change in p is followed by a $\pi/2$-phase shifted response of the displacement u which acts back on the electronic subsystem. After the driving pulse has vanished, the system oscillates with a renormalised frequency $\Omega > \Omega_0$.

In the next step the driving-dependent melting of the nuclear order u and thus of the Peierls gap is investigated. In Fig. 3 the minimum of the time-dependent oscillation $u(t)$ divided by the initial displacement u_0 is shown as a function of the peak driving amplitude. The data clearly indicates a phase transition at a critical electrical field $E_{\text{max}} = 0.5$ MV/cm. Approaching this driving amplitude from below, the time-dependent order $u(t)$ drops to zero and changes its sign. In order to further investigate this critical point, in Fig. 4 the change of the oscillation frequency of the nuclear system is investigated. At the same point shortly before $E_{\text{max}} = 0.5$ MV/cm there is a strong softening of the (q=0)-phonon mode. This confirms the interpretation of a nonequilibrium phase-transition taking place. The softening can be understood by the change of the overall energy potential of the whole system from a double-well potential to a quadratic potential with one minimum. At the transition point the effective free energy becomes flat. In an

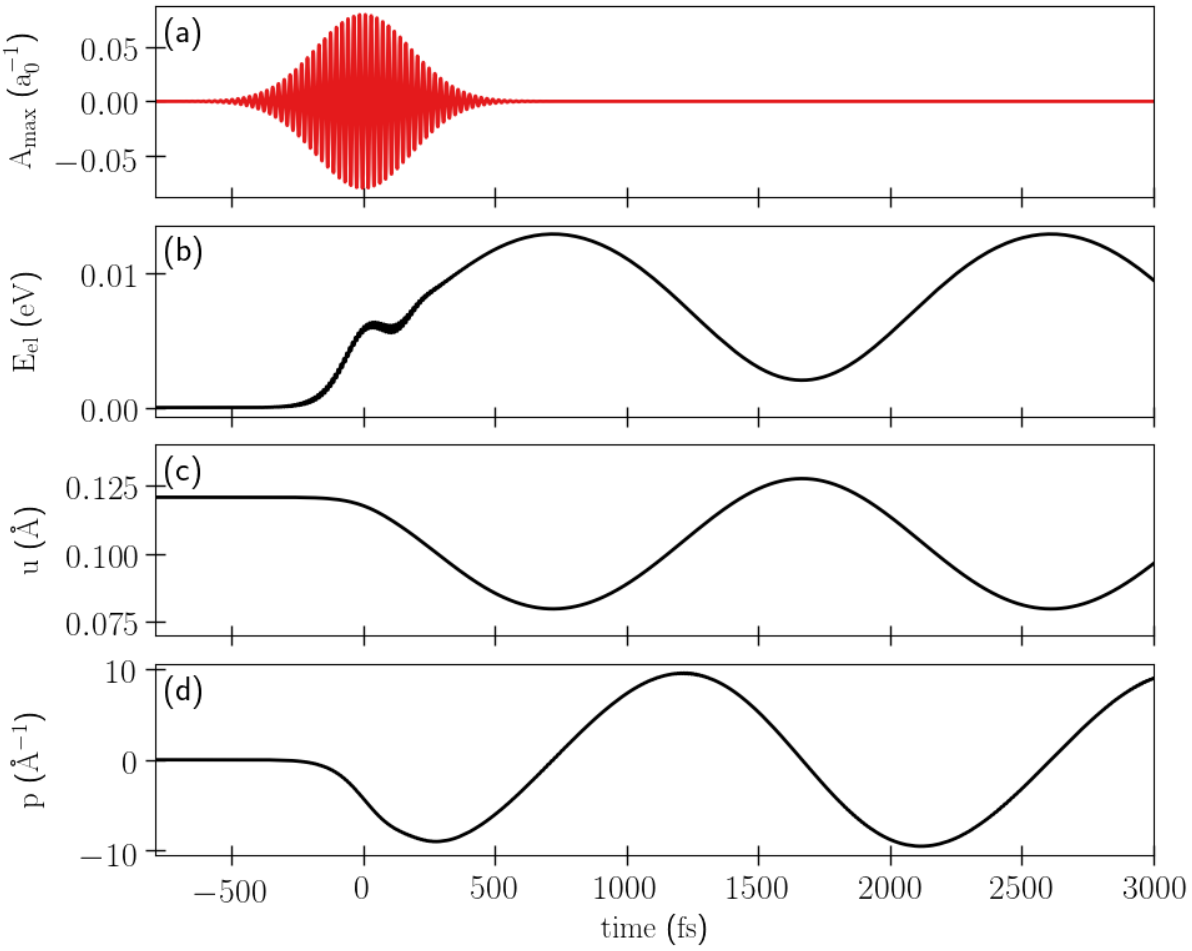

Figure 2: Dynamics of the electronically driven system for driving parameters $\omega = 190$ meV, $A_{\max} = 0.08\ a_0^{-1}$, and a FWHM of 300 fs of the intensity profile. (a) Time-dependent driving field. (b) Time-dependent electronic energy per unit cell. (c) Time-dependent nuclear displacement. (d) Time-dependent nuclear momentum.

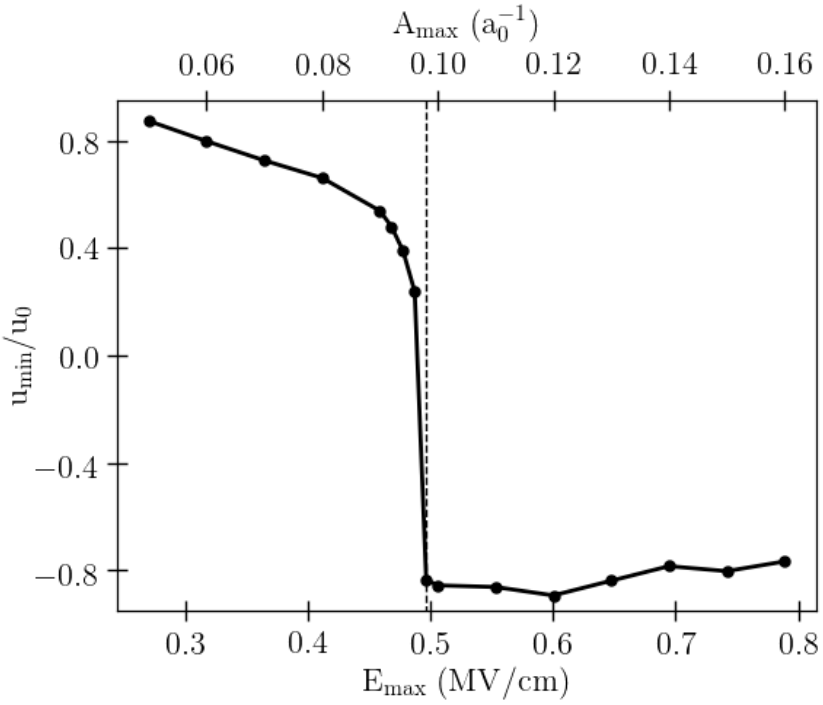

Figure 3: Change of nuclear displacement as function of driving amplitude (upper horizontal axis indicates amplitude of the vector potential, lower axis of the corresponding peak electrical field) for driving energy $\omega = 190$ meV, and a FWHM of 300 fs of the intensity profile. The critical field is indicated by a dashed line.

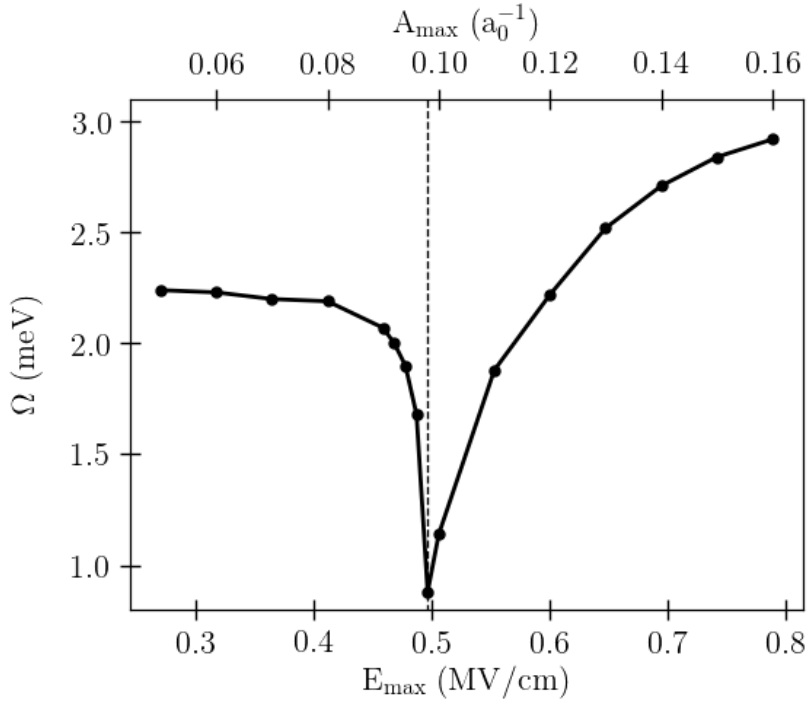

Figure 4: Softening of (q=0)-phonon mode as function of driving amplitude (upper horizontal axis indicates amplitude of the vector potential, lower axis of the corresponding peak electrical field) for driving energy $\omega = 190$ meV, and a FWHM of 300 fs of the intensity profile. The critical field is indicated by a dashed line.

approximated static picture this results in a critical slowing down of the amplitude mode which is proportional to the dynamics of u. The subsequent hardening of the frequency can be explained in a similar way. The additional amount of energy that is pumped into the system increases the steepness of the free energy potential, which results in a faster oscillation of the order parameter.

A quantitative comparison with the results from the driven indium-wires eight-band model is, due to the employed simplifications, not possible. Nevertheless, the reduced threshold, compared to the numerical findings of the second project [2], of the critical amplitude from $E_{\max} = 1.0$ MV/cm to $E_{\max} = 0.5$ MV/cm agrees with the intuition about a dynamically reduced Peierls gap. As already mentioned, an advancement would be to investigate relaxation and dissipation effects. The implementation of Lindblad-type open dynamics, as used for the pyrochlore model, would be straightforward. Another potential approach includes the consideration of both electron-phonon and electron-electron interactions. Finally, by a multitrajectory Ehrenfest approach [84], the impact of nuclear fluctuations on the melting process could be taken into account.

Taken together, the inclusion of time-dependent nuclear effects via Ehrenfest dynamics provides a more realistic theoretical description of the ultrafast melting of a CDW order in one-dimensional indium wires. Presumably, the actual impact of the nuclear dynamics on the quantitative results will crucially depend on the model details, e.g the time and energy scales of the driving field. This has to be carefully investigated by additional studies.

Declaration of contrinution **G. E. Topp** wrote the `C++` code, ran the simulations and created the presented figures. The results were discussed by **G. E. Topp**, M. A. Sentef, and A. Rubio.

8.2 SP III: Dissipative real-time calculations for laser-driven twisted bilayer graphene

This project is a continuation of the work presented in publication **III**, (Ref. [3]). In order to provide a realistic theoretical description of laser-driven systems, electronic relaxation and dissipation processes have to be included. These processes naturally compete with the laser-induced heating and have direct impact on the resulting dynamics. As discussed by Sato et al. in [24] for graphene, population effects play an important role regarding the anomalous Hall response under a circularly polarised driving field. These effects originate from resonant heating of the electronic system via the coupled laser mode. In this subsequent project Sato's work is taken into consideration and the anomalous Hall conductivity in twisted bilayer graphene is investigated by means of dissipative real-time simulations. The numerical approach and first preliminary results of this currently ongoing project are discussed in the following. A complete and up-to-date version of the code can be accessed at `https://github.com/Fizztopp/TBG_REALTIME.git`.

The numerical challenge regarding the dynamical propagation of the full electronic density operator for twisted bilayer graphene is the mere size of the atomic supercell. For small twist

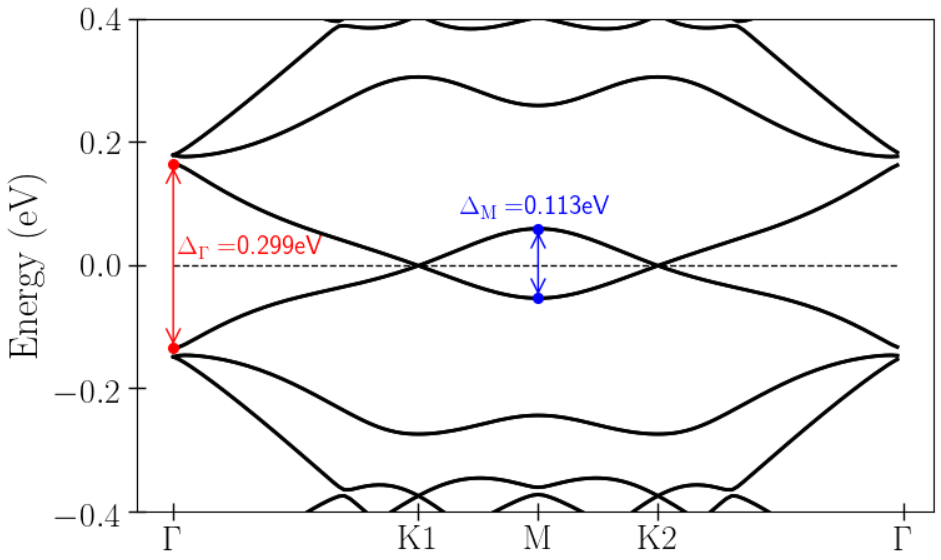

Figure 5: Low-energy equilibrium band structure of twisted bilayer graphene for a twist angle of $\Theta = 2.13°$. The symmetry path through the Brillouin zone is taken along the two Dirac points K1 and K2. The electronic bandwidth at Γ and M is indicated by colored arrows.

angles the unit cell has a size of several thousand atoms. Small angles around $2°$ and below are of peculiar interest for ultrafast transport measurements under mid-IR laser driving, since in this regime the electronic bandwidth is of the order of hundreds to several tens of meV. A real-time study of this regime by the investigation of ultrafast laser-induced current dynamics is the ultimate goal of this project. The electronic equilibrium band structure for a twist angle of $\Theta = 2.13°$ together with the associated energy scales is presented in Fig. 5. As the envisioned time-dependent current simulations additionally require a fine sampling of the reciprocal unit cell, an appropriate approximation of the high-dimensional Hamiltonian has to be employed. In the following, such an approximated approach is presented. For this purpose, the system dimension is effectively reduced via a Taylor expansion for small external fields and a subsequent band truncation of the Hamiltonian. Importantly, this approach is not restricted to the presented model but can generally be exploited for other high-dimensional tight-binding models, whose dynamics are induced by a time-dependent gauge field. Here, an in-plane polarization of the external field is assumed $\mathbf{A}(t) = (A_\mathrm{x}(t), A_\mathrm{y}(t))$.

We use units where $e = \hbar = c = 1$. The starting point is the tight-binding Hamiltonian that describes the p_z-orbitals of the bilayer-graphene supercell. This Hamiltonian was already introduced and discussed in Sec. 6.3. The first step is a Taylor expansion of the Peierls-substituted Hamiltonian $H_k[\mathbf{A}]$ in the momentum-dependent orbital basis at vanishing field amplitudes, $\mathbf{A}_0 \equiv (0,0)^T$. This Taylor expansion is defined as

$$T\left\{H_\mathbf{k}[\mathbf{A}], \mathbf{A}_0\right\} \equiv \sum_{n=0}^{\infty} \frac{1}{n!} \left((\mathbf{A} - \mathbf{A}_0) \cdot \nabla_\mathbf{A}\right)^n H_\mathbf{k}[\mathbf{A}_0].$$

This infinite series is in practice approximated by a truncation after a finite order and convergence in the cutoff is checked for each calculation. In the following, terms up to the order $n = 3$ are considered. The Taylor-expanded Hamiltonian is of the explicit form

$$\begin{aligned} T\left\{H_{\mathbf{k}}[\mathbf{A}], \mathbf{A}_0\right\} &= H_{\mathbf{k}}[\mathbf{A}_0] \\ &+ A_x \frac{\partial H_{\mathbf{k}}}{\partial A_x}[\mathbf{A}_0] + A_y \frac{\partial H_{\mathbf{k}}}{\partial A_y}[\mathbf{A}_0] \\ &+ \frac{1}{2}\left[A_x^2 \frac{\partial^2 H_{\mathbf{k}}}{\partial A_x^2}[\mathbf{A}_0] + 2A_x A_y \frac{\partial^2 H_{\mathbf{k}}}{\partial A_x A_y}[\mathbf{A}_0] + A_y^2 \frac{\partial^2 H_{\mathbf{k}}}{\partial A_y^2}[\mathbf{A}_0]\right] \\ &+ \frac{1}{6}\left[A_x^3 \frac{\partial^3 H_{\mathbf{k}}}{\partial A_x^3}[\mathbf{A}_0] + 3A_x^2 A_y \frac{\partial^3 H_{\mathbf{k}}}{\partial A_x^2 A_y}[\mathbf{A}_0]\right. \\ &\quad \left. + 3A_x A_y^2 \frac{\partial^3 H_{\mathbf{k}}}{\partial A_x A_y^2}[\mathbf{A}_0] + A_y^3 \frac{\partial^3 H_{\mathbf{k}}}{\partial A_y^3}[\mathbf{A}_0]\right] \\ &\equiv H_{\mathbf{k}}^{\text{Taylor}}. \end{aligned}$$

The matrix derivatives appearing in the above equation are set by the implemented function 17 (see Appendix B.5).

In order to reduce the dimension of the Hamiltonian, a truncation in the energy eigenbasis of the unperturbed Hamiltonian is performed. Therefore, an appropriate energy-window ΔE for the truncation of the matrices has to be set. This window is chosen symmetrically around the Fermi energy. The size of the energy window is ultimately governed by the driving amplitude and driving frequency and has to be chosen such that the dynamics of the system are well approximated. Therefore, the unperturbed Hamiltonian, $H_{\mathbf{k}}[\mathbf{A}_0]$, is transformed to the initial energy eigenbasis. This basis is defined by the eigenequation $H_{\mathbf{k}}[\mathbf{A}_0]\,|\mathbf{k}, \alpha\rangle = \epsilon_{\mathbf{k}\alpha}\,|\mathbf{k}, \alpha\rangle$ (with quasimomentum $\mathbf{k}$ and a band index α). Afterwards, the index-positions of the ordered energy eigenvalues for the lower and upper energy boundary are identified. This is implemented by function 18 (see Appendix B.5). The energy cutoff is set by a globally defined constant `lim`. The limits are set in units of the driving frequency which defines the dominant energy scale of the dynamical calculations.

Having identified the window for the energy cutoff, all Taylor expansion matrices are transformed to the initial band basis of the unperturbed Hamiltonian. Afterwards, the transformed matrices are truncated according to the previously calculated energy window. This truncation procedure is implemented by function 19 (see Appendix B.5). The corresponding time-dependent Hamiltonian is set by function 20 (see Appendix B.5). Here, the gauge potential appears via the time-dependent prefactors `AX` and `AY` which are multiplied by the expansion matrices in the truncated initial band basis.

The initial density operator is defined in the truncated band basis with the temperature-dependent Fermi functions appearing as diagonal entries. The energy arguments of the Fermi distributions correspond to the energy eigenvalues within the chosen window. For the time propagation the Adams-Bashforth multistep procedure, which was already introduced in Sec. 6.1,

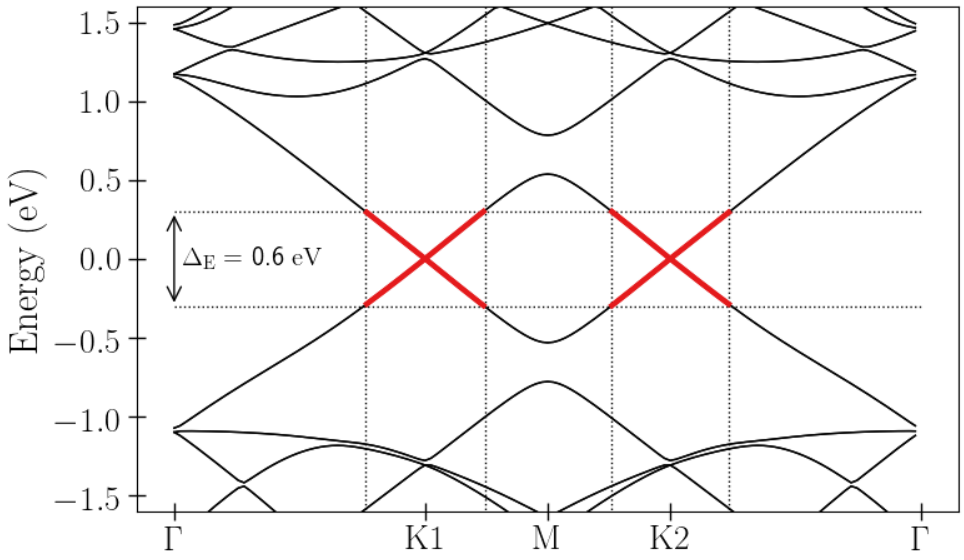

Figure 6: Equilibrium band structure of twisted bilayer graphene for a twist angle of $\Theta = 7.34°$. The symmetry path through the Brillouin zone is taken along the two Dirac points K1 and K2. The horizontal dotted lines indicate the chosen window for the energy cutoff (0.6 eV). The remaining band energies of the truncated Hamiltonian are indicated by red color. The vertical dotted lines indicate the corresponding area of the reciprocal unit cell, which are sampled for the dynamical simulations within a circle of radius $|K1 - K2|/4$ around the Dirac points.

is used. The full propagation is performed in the initial truncated band basis. The time-dependent current operators are defined by the derivatives of the Taylor-expanded Hamiltonian by the spatial components of the time-dependent gauge potential

$$\hat{J}^{\mathbf{k}}_{\mathrm{x}}(t) = -\frac{\partial \hat{H}^{\mathrm{Taylor}}_{\mathbf{k}}(t)}{\partial A_{\mathrm{x}}(t)}, \quad \hat{J}^{\mathbf{k}}_{\mathrm{y}}(t) = -\frac{\partial \hat{H}^{\mathrm{Taylor}}_{\mathbf{k}}(t)}{\partial A_{\mathrm{y}}(t)}.$$

The current operators are implemented by the functions 21 and 22 (see Appendix B.5). As the total Hamiltonian is block-diagonal regarding the quasi-momentum $\mathbf{k}$, a `MPI`-parallel calculation of the above discussed procedure for the different points of the Brillouin zone is straightforward. This is inevitable due to the slow convergence of the Hall current with respect to the k-grid.

In the following, simulations of a time-dependent Hall current as result of a small longitudinal source-drain field in x-direction and a circularly polarized mid-IR ($\omega = 190$ meV) in-plane field are presented. For this first proof of principle, an intermediate angle $\Theta = 7.34$ (in accordance with project **III**, Ref. [3]) is chosen. The equilibrium band structure along the Dirac-points is presented in Fig. 6. The horizontal lines indicate the chosen energy window $\Delta E = 0.6$ eV. The red lines indicate the remaining subset of energy states, which is considered for the following simulations of the the dynamical response of the system. For weak fields and the chosen pulse energy, the electronic dynamics are well approximated by this choice (convergence has been checked).

For the source-drain field in x-direction the following time-profile is employed (in accordance

to Ref. [14])

$$\mathbf{E}_{\mathrm{SD}} = E_{\mathrm{SD}}\mathbf{e}_{\mathrm{x}} f(t),$$

where the switch-on function $f(t)$ is defined as

$$f(x) = \begin{cases} 1, & 1 < t \\ 3t^2 - 2t^3, & 0 < t \leq 1 \\ 0, & \text{otherwise.} \end{cases}$$

The circular light pulse is implemented by

$$\mathbf{A}(t) = A_{\mathrm{max}} \left[\sin\left(\frac{\pi t}{T_{\mathrm{circ}}}\right)\right]^2 \left[\tau_{\mathrm{circ}}\mathbf{e}_{\mathrm{x}} \sin(\omega t) + \mathbf{e}_{\mathrm{y}} \cos(\omega t)\right].$$

Here, T_{circ} is the full duration of the pulse, $\mathbf{e_x}$ and $\mathbf{e_y}$ are the spatial basis vectors, and $\tau_{\mathrm{circ}} = \pm 1$ defines the chirality of the pulse.

The peak electrical amplitude for the source-drain field is set to $E_{SD} = 0.01$ MV/m. The amplitude of the circular electrical field is set to $E_{\mathrm{max}} = 5$ MV/m (related to A_{max} in units of the inverse monolayer lattice constant $a_0^{-1} = 1/2.445$ Å^{-1} by $E_{\mathrm{max}} = \omega A_{\mathrm{max}}$). A total pump duration $T_{\mathrm{circ}} = 300$ fs is employed. For the system-bath coupling, the longitudinal relaxation time is set to $T_1 = 100$ fs, the transverse relaxation time is set to $T_2 = 20$ fs (for details see Ref. [14]). The reciprocal unit cell is sampled within a circle of radius $|K1 - K2|/4$ around the Dirac points with a total number of 39586 sampling points. As the reciprocal cell is not periodic in this setup, a time-dependent correction has to be added to the currents. This correction subtracts the instantaneous equilibrium current from the total time-dependent current (for details see Ref. [14]).

The calculated current dynamics are shown in Fig. 7. In Fig. 7a the time profiles of the source-drain field and the circular pump field are depicted. Fig. 7b shows the corrected current signal in x-direction. The sign-flip between the two chiralities in the x-component of the driving field is imprinted onto the current signal. Fig. 7c shows the time-dependent current in y-direction, in transverse direction to the source-drain field. The anomalous Hall current is defined by the difference between the currents in y-direction that are generated by the right and left circularly polarized field

$$J_{\mathrm{Hall}}(t) = \frac{1}{2}\left[J_{\mathrm{y}}^{\mathrm{R}}(t) - J_{\mathrm{y}}^{\mathrm{L}}(t)\right].$$

The time-dependent Hall current is presented in Fig. 7d. The red and black line indicate the Hall currents for an opposite choice of the source-drain field. The expected sign flip of the Hall current, which originates from the symmetry of the system, is reproduced. Compared to the peak position of the circular driving field, the Hall current shows a delayed increase. This delay is

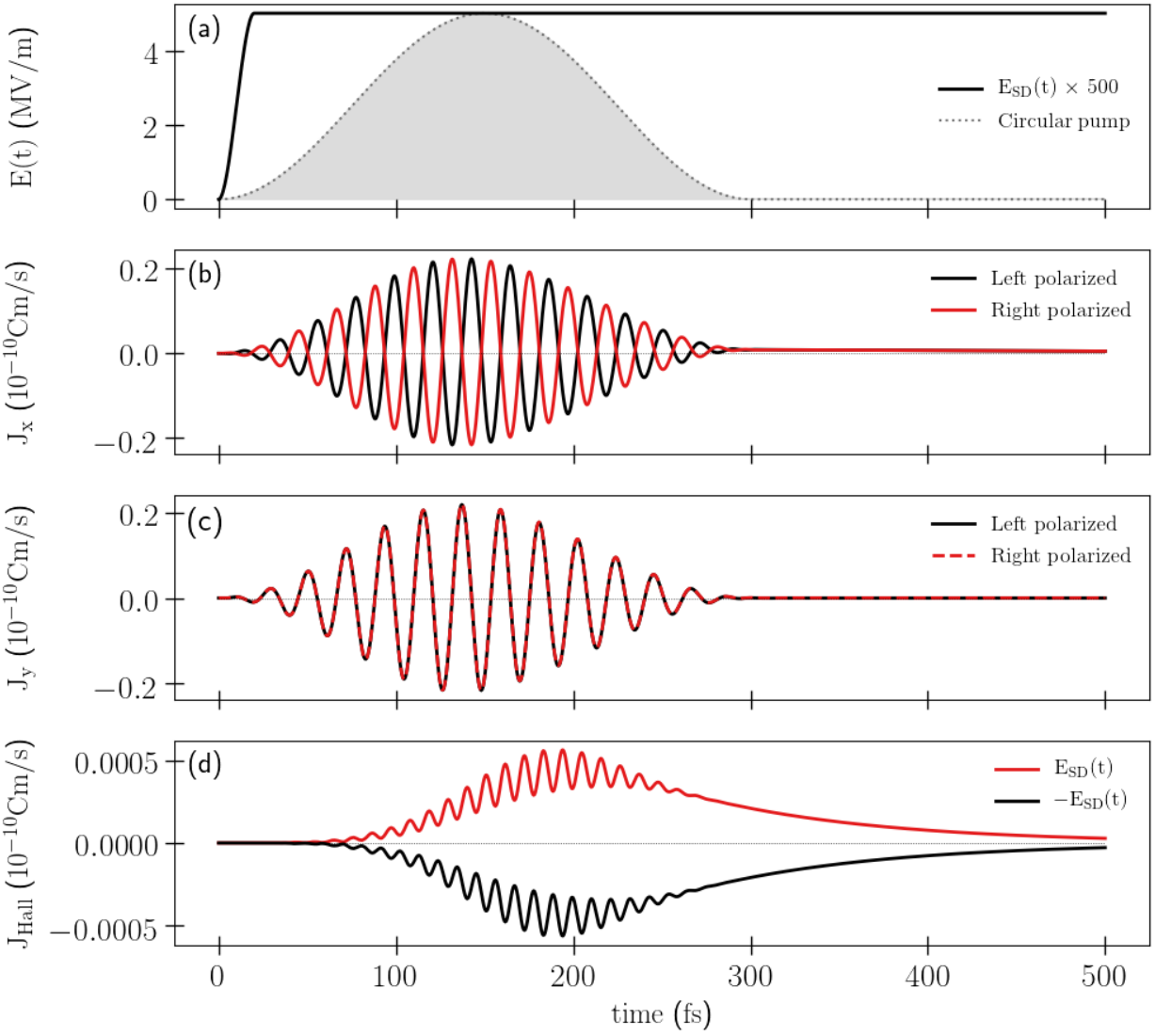

Figure 7: Light-induced Hall current (a) The black solid line indicates the source-drain field in x-direction. The grey shaded area shows the time-envelope of the circular pump pulse. (b) Time-dependent current in x-direction for left ($\tau_{\mathrm{circ}} = 1$) and right ($\tau_{\mathrm{circ}} = -1$) polarization. (c) Time-dependent current in y-direction (transverse to source-drain field) for left ($\tau_{\mathrm{circ}} = 1$) and right ($\tau_{\mathrm{circ}} = -1$) polarization. (d) Time-dependent Hall current (black line indicates reversed source-drain field).

assumed to have its origin in the ratio between the pump duration T_{circ} and the relaxation time scales T_1 and T_2.

The finding of an anomalous light-induced Hall current in intermediate-angle twisted bilayer graphene is the first central result of this ongoing project. By the ratio of the peak field amplitudes and the source-drain field amplitude, an anomalous Hall conductivity $\sigma_{xy} = J_{\mathrm{Hall}}/E_{\mathrm{SD}}$ can be defined. The next step for this project is to investigate this Hall conductivity as a function of the chemical potential (for the shown results charge neutrality was employed) and for different circular field amplitudes. Moreover, the impact of the twist angle on the Hall conductivity will be investigated. Therefore, as discussed above, smaller twist angles might be of particular interest.

Declaration of contribution L. Xian provided a `Fortan90` code, containing a DFT-fitted implementation of the original twisted bilayer graphene equilibrium Hamiltonian and a method for the generation of the crystal lattice. **G. E. Topp** translated this code to `Python` and `C++`. **G. E. Topp** extended the code by the truncation, and propagation methods. **G. E. Topp** performed the presented simulations, analyzed the data, and created the presented plots. The results were discussed by **G. E. Topp**, M. A. Sentef, S. Sato, L. Xian, G. Jotz, J. McIver and A. Rubio.

References

1. **G. E. Topp**, N. Tancogne-Dejean, A. F. Kemper, A. Rubio, and M. A. Sentef. All-optical nonequilibrium pathway to stabilising magnetic Weyl semimetals in pyrochlore iridates. *Nature Communications*, 9(1):4452, Oct 2018. URL https://www.nature.com/articles/s41467-018-06991-8.

2. M. Chávez-Cervantes, **G. E. Topp**, S. Aeschlimann, R. Krause, S. A. Sato, M. A. Sentef, and I. Gierz. Charge density wave melting in one-dimensional wires with femtosecond subgap excitation. *Phys. Rev. Lett.*, 123:036405, Jul 2019. URL https://link.aps.org/doi/10.1103/PhysRevLett.123.036405.

3. **G. E. Topp**, G. Jotzu, J. W. McIver, L. Xian, A. Rubio, and M. A. Sentef. Topological Floquet engineering of twisted bilayer graphene. *Phys. Rev. Research*, 1:023031, Sep 2019. URL https://link.aps.org/doi/10.1103/PhysRevResearch.1.023031.

4. R. Singla, G. Cotugno, S. Kaiser, M. Först, M. Mitrano, H. Y. Liu, A. Cartella, C. Manzoni, H. Okamoto, T. Hasegawa, S. R. Clark, D. Jaksch, and A. Cavalleri. Thz-frequency modulation of the Hubbard U in an organic Mott insulator. *Phys. Rev. Lett.*, 115:187401, Oct 2015. URL https://link.aps.org/doi/10.1103/PhysRevLett.115.187401.

5. E. Pomarico, M. Mitrano, H. Bromberger, M. A. Sentef, A. Al-Temimy, C. Coletti, A. Stöhr, S. Link, U. Starke, C. Cacho, R. Chapman, E. Springate, A. Cavalleri, and I. Gierz. Enhanced electron-phonon coupling in graphene with periodically distorted lattice. *Phys. Rev. B*, 95 (2):024304, Jan 2017. URL http://link.aps.org/doi/10.1103/PhysRevB.95.024304.

6. N. Tancogne-Dejean, M. A. Sentef, and A. Rubio. Ultrafast modification of Hubbard U in a strongly correlated material: Ab initio high-harmonic generation in NiO. *Phys. Rev. Lett.*, 121:097402, Aug 2018. URL https://link.aps.org/doi/10.1103/PhysRevLett.121.097402.

7. D. Fausti, R. I. Tobey, N. Dean, S. Kaiser, A. Dienst, M. C. Hoffmann, S. Pyon, T. Takayama, H. Takagi, and A. Cavalleri. Light-induced superconductivity in a stripe-ordered cuprate. *Science*, 331(6014):189–191, Jan 2011. URL http://www.sciencemag.org/content/331/6014/189.

8. M. Mitrano, A. Cantaluppi, D. Nicoletti, S. Kaiser, A. Perucchi, S. Lupi, P. Di Pietro, D. Pontiroli, M. Riccò, S. R. Clark, D. Jaksch, and A. Cavalleri. Possible light-induced superconductivity in K_3C_{60} at high temperature. *Nature*, 530(7591):461–464, Feb 2016. URL http://www.nature.com/nature/journal/v530/n7591/full/nature16522.html.

9. M. Rini, R. Tobey, N. Dean, J. Itatani, Y. Tomioka, Y. Tokura, R. W. Schoenlein, and A. Cavalleri. Control of the electronic phase of a manganite by mode-selective vibrational excitation. *Nature*, 449(7158):72–74, Sep 2007. URL http://www.nature.com/nature/journal/v449/n7158/abs/nature06119.html.

10. L. Stojchevska, I. Vaskivskyi, T. Mertelj, P. Kusar, D. Svetin, S. Brazovskii, and D. Mihailovic. Ultrafast switching to a stable hidden quantum state in an electronic crystal. *Science*, 344 (6180):177–180, Apr 2014. URL http://science.sciencemag.org/content/344/6180/177.

11. M. Claassen, D. M. Kennes, M. Zingl, M. A. Sentef, and A. Rubio. Universal optical control of chiral superconductors and Majorana modes. *Nature Physics*, page 1, May 2019. URL https://www.nature.com/articles/s41567-019-0532-6.

12. N. Tsuji, M. Eckstein, and P. Werner. Nonthermal antiferromagnetic order and nonequilibrium criticality in the Hubbard model. *Phys. Rev. Lett.*, 110:136404, Mar 2013. URL https://link.aps.org/doi/10.1103/PhysRevLett.110.136404.

13. T. Oka and H. Aoki. Photovoltaic Hall effect in graphene. *Phys. Rev. B*, 79(8):081406, Feb 2009. URL https://link.aps.org/doi/10.1103/PhysRevB.79.081406.

14. S. A. Sato, P. Tang, M. A. Sentef, U. De Giovannini, H. Hübener, and H. Rubio. Light-induced anomalous Hall effect in massless Dirac fermion systems and topological insulators with dissipation. *New Journal of Physics*, 21(9):093005, Sep 2019. URL https://doi.org/10.1088%2F1367-2630%2Fab3acf.

15. J. W. McIver, B. Schulte, F.-U. Stein, T. Matsuyama, G. Jotzu, G. Meier, and A. Cavalleri. Light-induced anomalous Hall effect in graphene. *Nature Physics*, pages 1–4, 2019. URL https://www.nature.com/articles/s41567-019-0698-y.

16. D. Hsieh, Y. Xia, D. Qian, L. Wray, J. H. Dil, F. Meier, J. Osterwalder, L. Patthey, J. G. Checkelsky, N. P. Ong, A. V. Fedorov, H. Lin, A. Bansil, D. Grauer, Y. S. Hor, R. J. Cava, and M. Z. Hasan. A tunable topological insulator in the spin helical Dirac transport regime. *Nature*, 460(7259):1101–1105, 2009. URL https://www.nature.com/articles/nature08234.

17. J. Li, T. Neupert, Z. Wang, A. H. MacDonald, A. Yazdani, and B. A. Bernevig. Two-dimensional chiral topological superconductivity in Shiba lattices. *Nature Communications*, 7(1):1–7, 2016. URL https://www.nature.com/articles/ncomms12297.

18. G. Li, A. Luican, J. M. B. Lopes dos Santos, A. H. Castro Neto, A. Reina, J. Kong, and E. Y. Andrei. Observation of Van Hove singularities in twisted graphene layers. *Nature Physics*, 6 (2):109–113, Feb 2010. URL https://www.nature.com/articles/nphys1463.

19. W. Qin, L. Li, and Z. Zhang. Chiral topological superconductivity arising from the interplay of geometric phase and electron correlation. *Nature Physics*, 15(8):796–802, 2019. URL https://www.nature.com/articles/s41567-019-0517-5.

20. M. A. Sentef, M. Ruggenthaler, and A. Rubio. Cavity quantum-electrodynamical polaritonically enhanced electron-phonon coupling and its influence on superconductivity. *Science Advances*, 4(11):eaau6969, Nov 2018. URL http://advances.sciencemag.org/content/4/11/eaau6969.

21. J. B. Curtis, Z. M. Raines, A. A. Allocca, M. Hafezi, and V. M. Galitski. Cavity quantum eliashberg enhancement of superconductivity. *Phys. Rev. Lett.*, 122(16):167002, Apr 2019. URL https://link.aps.org/doi/10.1103/PhysRevLett.122.167002.

22. X. Wang, E. Ronca, and M. A. Sentef. Cavity quantum electrodynamical chern insulator: Towards light-induced quantized anomalous Hall effect in graphene. *Phys. Rev. B*, 99:235156, Jun 2019. URL https://link.aps.org/doi/10.1103/PhysRevB.99.235156.

23. A. Thomas, E. Devaux, K. Nagarajan, T. Chervy, S. Seidel, D. Hagenmüller, S. Schütz, J. Schachenmayer, C. Genet, G. Pupillo, and T. W. Ebbesen. Exploring superconductivity under strong coupling with the vacuum electromagnetic field, 2019. arXiv: 1812.08776.

24. S. A. Sato, J. W. McIver, M. Nuske, P. Tang, G. Jotzu, B. Schulte, H. Hübener, U. De Giovannini, L. Mathey, M. A. Sentef, A. Cavalleri, and A. Rubio. Microscopic theory for the light-induced anomalous Hall effect in graphene. *Phys. Rev. B*, 99(21):214302, Jun 2019. URL https://link.aps.org/doi/10.1103/PhysRevB.99.214302.

25. Hermann Weyl. Elektron und Gravitation. i. *Zeitschrift für Physik*, 56(5):330–352, 1929. URL https://doi.org/10.1007/BF01339504.

26. X. Wan, A. M. Turner, A. Vishwanath, and S. Y. Savrasov. Topological semimetal and Fermi-arc surface states in the electronic structure of pyrochlore iridates. *Phys. Rev. B*, 83 (20):205101, 2011. URL https://link.aps.org/doi/10.1103/PhysRevB.83.205101.

27. S.-Y. Xu, I. Belopolski, N. Alidoust, M. Neupane, G. Bian, C. Zhang, R. Sankar, G. Chang, Z. Yuan, C.-C. Lee, S.-M. Huang, H. Zheng, J. Ma, D. S. Sanchez, B. Wang, A. Bansil, F. Chou, P. P. Shibayev, H. Lin, S. Jia, and M. Z. Hasan. Discovery of a weyl fermion semimetal and topological fermi arcs. *Science*, 349(6248):613–617, Aug 2015. URL https://science.sciencemag.org/content/349/6248/613.

28. L. Lu, Z. Wang, D. Ye, L. Ran, L. Fu, J. D. Joannopoulos, and M. Soljačić. Experimental observation of Weyl points. *Science*, 349(6248):622–624, Aug 2015. URL https://science.sciencemag.org/content/349/6248/622.

29. L. X. Yang, Z. K. Liu, Y. Sun, H. Peng, H. F. Yang, T. Zhang, B. Zhou, Y. Zhang, Y. F. Guo, M. Rahn, D. Prabhakaran, Z. Hussain, S.-K. Mo, C. Felser, B. Yan, and Y. L. Chen. Weyl semimetal phase in the non-centrosymmetric compound TaAs. *Nature Physics*, 11(9): 728–732, Aug 2015. URL https://www.nature.com/articles/nphys3425.

30. J. Xiong, S. K. Kushwaha, T. Liang, J. W. Krizan, M. Hirschberger, W. Wang, R. J. Cava, and N. P. Ong. Evidence for the chiral anomaly in the dirac semimetal Na_3Bi. *Science*, 350(6259): 413–416, 2015. URL https://science.sciencemag.org/content/350/6259/413.

31. W. Witczak-Krempa and Y. B. Kim. Topological and magnetic phases of interacting electrons in the pyrochlore iridates. *Phys. Rev. B*, 85:045124, Jan 2012. URL https://link.aps.org/doi/10.1103/PhysRevB.85.045124.

32. W. Witczak-Krempa, A. Go, and Y. B. Kim. Pyrochlore electrons under pressure, heat, and field: Shedding light on the iridates. *Phys. Rev. B*, 87(15):155101, 2013. URL https://link.aps.org/doi/10.1103/PhysRevB.87.155101.

33. R. Wang, A. Go, and A. J. Millis. Electron interactions, spin-orbit coupling, and intersite correlations in pyrochlore iridates. *Phys. Rev. B*, 95(4):045133, 2017. URL https://link.aps.org/doi/10.1103/PhysRevB.95.045133.

34. A. Go, W. Witczak-Krempa, G. S. Jeon, K. Park, and Y. Kim. Correlation effects on 3d topological phases: From bulk to boundary. *Physical Review Letters*, 109(6):066401, 2012. URL https://link.aps.org/doi/10.1103/PhysRevLett.109.066401.

35. N. Taira, M. Wakeshima, and Y. Hinatsu. Magnetic properties of iridium pyrochlores $R_2Ir_2O_7$ (R = Y, Sm, Eu and Lu). *J. Phys.: Condens. Matter*, 13(23):5527, 2001. URL http://stacks.iop.org/0953-8984/13/i=23/a=312.

36. K. Matsuhira, M. Wakeshima, R. Nakanishi, T. Yamada, A. Nakamura, W. Kawano, S. Takagi, and Y. Hinatsu. Metal–insulator transition in pyrochlore iridates $Ln_2Ir_2O_7$ (Ln=Nd, Sm, and Eu). *J. Phys. Soc. Jpn.*, 76(4):043706, 2007. URL http://journals.jps.jp/doi/10.1143/JPSJ.76.043706.

37. S. M. Disseler, Chetan Dhital, T. C. Hogan, A. Amato, S. R. Giblin, Clarina de la Cruz, A. Daoud-Aladine, Stephen D. Wilson, and M. J. Graf. Magnetic order and the electronic ground state in the pyrochlore iridate $Nd_2Ir_2O_7$. *Phys. Rev. B*, 85:174441, May 2012. URL https://link.aps.org/doi/10.1103/PhysRevB.85.174441.

38. S. M. Disseler, Chetan Dhital, A. Amato, S. R. Giblin, Clarina de la Cruz, Stephen D. Wilson, and M. J. Graf. Magnetic order in the pyrochlore iridates $A_2Ir_2O_7$ (A = Y, Yb). *Phys. Rev. B*, 86:014428, Jul 2012. URL https://link.aps.org/doi/10.1103/PhysRevB.86.014428.

39. A. B. Sushkov, J. B. Hofmann, G. S. Jenkins, J. Ishikawa, S. Nakatsuji, S. Das Sarma, and H. D. Drew. Optical evidence for a weyl semimetal state in pyrochlore $Eu_2Ir_2O_7$. *Phys. Rev. B*, 92:241108, Dec 2015. URL https://link.aps.org/doi/10.1103/PhysRevB.92.241108.

40. K. Tomiyasu, K. Matsuhira, K. Iwasa, M. Watahiki, S. Takagi, M. Wakeshima, Y. Hinatsu, M. Yokoyama, K. Ohoyama, and K. Yamada. Emergence of magnetic long-range order in frustrated pyrochlore $Nd_2Ir_2O_7$ with metal–insulator transition. *Journal of the Physical Society of Japan*, 81(3):034709, 2012. URL https://doi.org/10.1143/JPSJ.81.034709.

41. H. Sagayama, D. Uematsu, T. Arima, K. Sugimoto, J. J. Ishikawa, E. O'Farrell, and S. Nakatsuji. Determination of long-range all-in-all-out ordering of Ir^{4+} moments in a pyrochlore iridate $Eu_2Ir_2O_7$ by resonant x-ray diffraction. *Phys. Rev. B*, 87:100403, Mar 2013. URL https://link.aps.org/doi/10.1103/PhysRevB.87.100403.

42. S. M. Disseler. Direct evidence for the all-in/all-out magnetic structure in the pyrochlore iridates from muon spin relaxation. *Phys. Rev. B*, 89:140413, Apr 2014. URL https://link.aps.org/doi/10.1103/PhysRevB.89.140413.

43. H. Guo, C. Ritter, and A. C. Komarek. Direct determination of the spin structure of $Nd_2Ir_2O_7$ by means of neutron diffraction. *Phys. Rev. B*, 94:161102, Oct 2016. URL https://link.aps.org/doi/10.1103/PhysRevB.94.161102.

44. N. Tancogne-Dejean, M. J. T. Oliveira, and A. Rubio. Self-consistent DFT+U method for real-space time-dependent density functional theory calculations. *Phys. Rev. B*, 96:245133, Dec 2017. URL https://link.aps.org/doi/10.1103/PhysRevB.96.245133.

45. C. Blumenstein, J. Schäfer, S. Mietke, S. Meyer, A. Dollinger, M. Lochner, X. Y. Cui, L. Patthey, R. Matzdorf, and R. Claessen. Atomically controlled quantum chains hosting a Tomonaga–Luttinger liquid. *Nature Physics*, 7(10):776–780, 2011. URL https://www.nature.com/articles/nphys2051.

46. S. C. Erwin and F. J. Himpsel. Intrinsic magnetism at silicon surfaces. *Nature Communications*, 1(1):1–6, 2010. URL https://www.nature.com/articles/ncomms1056.

47. G. Li, P. Höpfner, J. Schäfer, C. Blumenstein, S. Meyer, A. Bostwick, E. Rotenberg, R. Claessen, and W. Hanke. Magnetic order in a frustrated two-dimensional atom lattice at a semiconductor surface. *Nature Communications*, 4(1):1–6, 2013. URL https://www.nature.com/articles/ncomms2617.

48. W. Kohn. Image of the Fermi surface in the vibration spectrum of a metal. *Phys. Rev. Lett.*, 2:393–394, May 1959. URL https://link.aps.org/doi/10.1103/PhysRevLett.2.393.

49. H. W. Yeom, S. Takeda, E. Rotenberg, I. Matsuda, K. Horikoshi, J. Schaefer, C. M. Lee, S. D. Kevan, T. Ohta, T. Nagao, and S. Hasegawa. Instability and charge density wave of metallic quantum chains on a silicon surface. *Phys. Rev. Lett.*, 82:4898–4901, Jun 1999. URL https://link.aps.org/doi/10.1103/PhysRevLett.82.4898.

50. H. W. Yeom, K. Horikoshi, H. M. Zhang, K. Ono, and R. I. G. Uhrberg. Nature of the broken-symmetry phase of the one-dimensional metallic In/Si(111) surface. *Phys. Rev. B*, 65:241307, May 2002. URL https://link.aps.org/doi/10.1103/PhysRevB.65.241307.

51. J. R. Ahn, J. H. Byun, H. Koh, E. Rotenberg, S. D. Kevan, and H. W. Yeom. Mechanism of gap opening in a triple-band Peierls system: In atomic wires on Si. *Phys. Rev. Lett.*, 93: 106401, Aug 2004. URL https://link.aps.org/doi/10.1103/PhysRevLett.93.106401.

52. S. J. Park, H. W. Yeom, S. H. Min, D. H. Park, and I. W. Lyo. Direct evidence of the charge ordered phase transition of indium nanowires on Si(111). *Phys. Rev. Lett.*, 93:106402, Sep 2004. URL https://link.aps.org/doi/10.1103/PhysRevLett.93.106402.

53. C. González, F. Flores, and J. Ortega. Soft phonon, dynamical fluctuations, and a reversible phase transition: Indium chains on silicon. *Phys. Rev. Lett.*, 96:136101, Apr 2006. URL https://link.aps.org/doi/10.1103/PhysRevLett.96.136101.

54. C. González, Jiandong Guo, J. Ortega, F. Flores, and H. H. Weitering. Mechanism of the band gap opening across the order-disorder transition of Si(111)4x1-In. *Phys. Rev. Lett.*, 102: 115501, Mar 2009. URL https://link.aps.org/doi/10.1103/PhysRevLett.102.115501.

55. G. Lee, S.-Y. Yu, H. Kim, and J.-Y. Koo. Defect-induced perturbation on Si(111)4x1-In: Period-doubling modulation and its origin. *Phys. Rev. B*, 70:121304, Sep 2004. URL https://link.aps.org/doi/10.1103/PhysRevB.70.121304.

56. S.-W. Kim and J.-H. Cho. Origin of the metal-insulator transition of indium atom wires on Si(111). *Phys. Rev. B*, 93:241408, Jun 2016. URL https://link.aps.org/doi/10.1103/PhysRevB.93.241408.

57. E. Jeckelmann, S. Sanna, W. G. Schmidt, E. Speiser, and N. Esser. Grand canonical Peierls transition in In/Si(111). *Phys. Rev. B*, 93:241407, Jun 2016. URL https://link.aps.org/doi/10.1103/PhysRevB.93.241407.

58. M. Chávez-Cervantes, R. Krause, S. Aeschlimann, and I. Gierz. Band structure dynamics in indium wires. *Phys. Rev. B*, 97:201401, May 2018. URL https://link.aps.org/doi/10.1103/PhysRevB.97.201401.

59. S. Wall, B. Krenzer, S. Wippermann, S. Sanna, F. Klasing, A. Hanisch-Blicharski, M. Kammler, W. G. Schmidt, and M. Horn-von Hoegen. Atomistic picture of charge density wave formation at surfaces. *Phys. Rev. Lett.*, 109:186101, Nov 2012. URL https://link.aps.org/doi/10.1103/PhysRevLett.109.186101.

60. T. Frigge, B. Hafke, T. Witte, B. Krenzer, C. Streubühr, A. Samad Syed, V. Mikšić Trontl, I. Avigo, P. Zhou, M. Ligges, D. von der Linde, U. Bovensiepen, M. Horn-von Hoegen, S. Wippermann, A. Lücke, S. Sanna, U. Gerstmann, and W. G. Schmidt. Optically excited structural transition in atomic wires on surfaces at the quantum limit. *Nature*, 544:207, 2017. URL https://doi.org/10.1038/nature21432.

61. F. D. M. Haldane. Model for a quantum Hall effect without Landau levels: Condensed-matter realization of the "parity anomaly". *Phys. Rev. Lett.*, 61(18):2015–2018, Oct 1988. URL http://link.aps.org/doi/10.1103/PhysRevLett.61.2015.

62. G. Trambly de Laissardière, D. Mayou, and L. Magaud. Localization of Dirac electrons in rotated graphene bilayers. *Nano Lett.*, 10(3):804–808, Mar 2010. URL https://doi.org/10.1021/nl902948m.

63. G. Trambly de Laissardière, D. Mayou, and L. Magaud. Numerical studies of confined states in rotated bilayers of graphene. *Phys. Rev. B*, 86(12):125413, Sep 2012. URL https://link.aps.org/doi/10.1103/PhysRevB.86.125413.

64. R. Bistritzer and A. H. MacDonald. Moiré bands in twisted double-layer graphene. *PNAS*, 108(30):12233–12237, Jul 2011. URL https://www.pnas.org/content/108/30/12233.

65. Y. Cao, V. Fatemi, A. Demir, S. Fang, S. L. Tomarken, J. Y. Luo, J. D. Sanchez-Yamagishi, K. Watanabe, T. Taniguchi, E. Kaxiras, R. C. Ashoori, and P. Jarillo-Herrero. Correlated insulator behaviour at half-filling in magic-angle graphene superlattices. *Nature*, 556(7699):80–84, Apr 2018. URL https://www.nature.com/articles/nature26154.

66. Y. Cao, V. Fatemi, S. Fang, K. Watanabe, T. Taniguchi, E. Kaxiras, and P. Jarillo-Herrero. Unconventional superconductivity in magic-angle graphene superlattices. *Nature*, 556(7699):43–50, Apr 2018. URL https://www.nature.com/articles/nature26160.

67. H. P. Breuer and F. Petruccione. *The theory of open quantum systems*. Oxford University Press, 2002.

68. Makoto Yamaguchi, Tatsuro Yuge, and Tetsuo Ogawa. Markovian quantum master equation beyond adiabatic regime. *Phys. Rev. E*, 95:012136, Jan 2017. URL https://link.aps.org/doi/10.1103/PhysRevE.95.012136.

69. S. Wippermann and W. G. Schmidt. Entropy explains metal-insulator transition of the Si(111)-in nanowire array. *Phys. Rev. Lett.*, 105:126102, Sep 2010. URL https://link.aps.org/doi/10.1103/PhysRevLett.105.126102.

70. Y. Xie, B. Lian, B. Jäck, X. Liu, C.-L. Chiu, K. Watanabe, T. Taniguchi, B. A. Bernevig, and A. Yazdani. Spectroscopic signatures of many-body correlations in magic-angle twisted bilayer graphene. *Nature*, 572(7767):101–105, 2019. URL https://www.nature.com/articles/s41586-019-1422-x.

71. Y. Choi, J. Kemmer, Y. Peng, Al. Thomson, H. Arora, R. Polski, Y. Zhang, H. Ren, J. Alicea, G. Refael, F. von Oppen, K. Watanabe, T. Taniguchi, and S. Nadj-Perge. Electronic correlations in twisted bilayer graphene near the magic angle. *Nature Physics*, 15(11):1174–1180, Nov 2019. URL https://www.nature.com/articles/s41567-019-0606-5.

72. A. Kerelsky, L. J. McGilly, D. M. Kennes, L. Xian, M. Yankowitz, S. Chen, K. Watanabe, T. Taniguchi, J. Hone, C. Dean, A. Rubio, and A. N. Pasupathy. Maximized electron interactions at the magic angle in twisted bilayer graphene. *Nature*, 572(7767):95–100, Aug 2019. URL https://www.nature.com/articles/s41586-019-1431-9.

73. R. Resta and D. Vanderbilt. Theory of Polarization: A Modern Approach. In *Physics of Ferroelectrics*, volume 105, pages 31–68. Springer Berlin Heidelberg, Berlin, Heidelberg, 2007. ISBN 978-3-540-34590-9. URL http://link.springer.com/10.1007/978-3-540-34591-6_2.

74. H. Sambe. Steady States and Quasienergies of a Quantum-Mechanical System in an Oscillating Field. *Phys. Rev. A*, 7(6):2203–2213, Jun 1973. URL https://link.aps.org/doi/10.1103/PhysRevA.7.2203.

75. M. A. Sentef, M. Claassen, A. F. Kemper, B. Moritz, T. Oka, J. K. Freericks, and T. P. Devereaux. Theory of Floquet band formation and local pseudospin textures in pump-probe photoemission of graphene. *Nature Communications*, 6:7047, May 2015. URL https://www.nature.com/articles/ncomms8047.

76. H. Hübener, M. A. Sentef, U. De Giovannini, A. F. Kemper, and A. Rubio. Creating stable Floquet–Weyl semimetals by laser-driving of 3d Dirac materials. *Nature Communications*, 8:13940, 2017. URL http://www.nature.com/ncomms/2017/170117/ncomms13940/full/ncomms13940.html.

77. C. Berke, P. Michetti, and C. Timm. Stability of the Weyl-semimetal phase on the pyrochlore lattice. *New Journal of Physics*, 20(4):043057, Apr 2018. URL https://doi.org/10.1088%2F1367-2630%2Faab881.

78. A. Crepaldi, G. Autès, G. Gatti, S. Roth, A. Sterzi, G. Manzoni, M. Zacchigna, C. Cacho, R. T. Chapman, E. Springate, E. A. Seddon, Ph. Bugnon, A. Magrez, H. Berger, I. Vobornik, M. Kalläne, A. Quer, K. Rossnagel, F. Parmigiani, O. V. Yazyev, and M. Grioni. Enhanced ultrafast relaxation rate in the Weyl semimetal phase of $MoTe_2$ measured by time- and angle-resolved photoelectron spectroscopy. *Phys. Rev. B*, 96:241408, Dec 2017. URL https://link.aps.org/doi/10.1103/PhysRevB.96.241408.

79. Y Li, H. A. Fertig, and B. Seradjeh. Floquet-engineered topological flat bands in irradiated twisted bilayer graphene, 2019. URL https://arxiv.org/abs/1910.04711. arXiv: 1910.04711.

80. O. Katz, G. Refael, and N. H. Lindner. Floquet flat-band engineering of twisted bilayer graphene, 2019. URL https://arxiv.org/abs/1910.13510. arXiv: 1910.13510.

81. W. P. Su, J. R. Schrieffer, and A. J. Heeger. Soliton excitations in polyacetylene. *Phys. Rev. B*, 22:2099–2111, Aug 1980. URL https://link.aps.org/doi/10.1103/PhysRevB.22.2099.

82. S. Cheon, T.-H. Kim, S.-H. Lee, and H. W. Yeom. Chiral solitons in a coupled double Peierls chain. *Science*, 350(6257):182–185, 2015. URL https://science.sciencemag.org/content/350/6257/182.

83. S. Chandola, K. Hinrichs, M. Gensch, N. Esser, S. Wippermann, W. G. Schmidt, F. Bechstedt, K. Fleischer, and J. F. McGilp. Structure of si(111)-in nanowires determined from the midinfrared optical response. *Phys. Rev. Lett.*, 102:226805, Jun 2009. URL https://link.aps.org/doi/10.1103/PhysRevLett.102.226805.

84. N. M. Hoffmann, C. Schäfer, A. Rubio, A. Kelly, and H. Appel. Capturing vacuum fluctuations and photon correlations in cavity quantum electrodynamics with multitrajectory ehrenfest dynamics. *Phys. Rev. A*, 99:063819, Jun 2019. URL https://link.aps.org/doi/10.1103/PhysRevA.99.063819.

85. J. Nagamatsu, N. Nakagawa, T. Muranaka, Y. Zenitani, and J. Akimitsu. Superconductivity at 39 K in magnesium diboride. *Nature*, 410(6824):63–64, 2001. URL https://www.nature.com/articles/35065039.

86. S. L. Bud'ko, G. Lapertot, C. Petrovic, C. E. Cunningham, N. Anderson, and P. C. Canfield. Boron isotope effect in superconducting MgB_2. *Phys. Rev. Lett.*, 86:1877–1880, Feb 2001. URL https://link.aps.org/doi/10.1103/PhysRevLett.86.1877.

87. T. Yildirim, O. Gülseren, J. W. Lynn, C. M. Brown, T. J. Udovic, Q. Huang, N. Rogado, K. A. Regan, M. A. Hayward, J. S. Slusky, T. He, M. K. Haas, P. Khalifah, K. Inumaru, and R. J. Cava. Giant anharmonicity and nonlinear electron-phonon coupling in MgB_2: A combined

first-principles calculation and neutron scattering study. *Phys. Rev. Lett.*, 87:037001, Jun 2001. URL https://link.aps.org/doi/10.1103/PhysRevLett.87.037001.

88. H. J. Choi, D. Roundy, H. Sun, M. L. Cohen, and S. G. Louie. The origin of the anomalous superconducting properties of MgB_2. *Nature*, 418(6899):758–760, Aug 2002. URL https://yonsei.pure.elsevier.com/en/publications/the-origin-of-the-anomalous-superconducting-properties-of-mgb2.

89. J. A. Alarco, P. C. Talbot, and I. D. R. Mackinnon. Phonon anomalies predict superconducting T_c for AlB_2 type structures. *Phys. Chem. Chem. Phys.*, 17(38):25090–25099, 2015. URL https://pubs.rsc.org/en/content/articlelanding/2015/cp/c5cp04402b.

90. T. Muranaka and J. Akimitsu. Superconductivity in MgB_2. *Zeitschfrift für Kristallographie*, 226(4):385–394, Apr 2011.

91. K. Kunc, I. Loa, Syassen. K., R. K. Kremer, and K. Ahn. MgB_2 under pressure: phonon calculations, raman spectroscopy, and optical reflectance. *Journal of Physics: Condensed Matter*, 13(44):9945–9962, Oct 2001. URL https://iopscience.iop.org/article/10.1088/0953-8984/13/44/310/meta.

Appendices

A Implementation of basic mathematical operations

This section briefly introduces the basic mathematical operation which are used for most parts of the code. The programming language is C++.

- Type definitions

```
// Complex numbers
typedef complex<double> cdouble;
// Vectors of real double values
typedef vector<double> dvec;
// Vectors of complex double values
typedef vector<cdouble> cvec;
// Complex i
cdouble II(0,1);
```

- Matrix diagonalisation
  This function is imported from the LAPACK library. A more detailed documentation can be found on http://www.netlib.org/lapack/explore-3.1.1-html/zheev.f.html

```
extern "C" {
/**
 *  Computes the eigenvalues and, optionally, the eigenvectors for a
     Hermitian matrices H
 */
    void zheev_(char* jobz, char* uplo, int* N, cdouble* H, int* LDA,
        double* W, cdouble* work, int* lwork, double* rwork, int *info);
}
//'N','V': Compute eigenvalues only, and eigenvectors
char    jobz = 'V';
//'U','L': Upper, Lower triangle of H is stored
char    uplo = 'U';
// The order of the matrix H. DIM >= 0
int     matsize = DIM;
// The leading dimension of the array H. lda >= max(1,DIM)
int     lda = DIM;
// The length of the array work. lwork >= max(1,2*DIM-1)
int     lwork = 2*DIM-1;
```

```
// Dimension (max(1, 3*DIM-2))
double rwork[3*DIM-2];
// dDimension (MAX(1,LWORK))
cdouble work[2*DIM-1];
// Info
int      info;

void diagonalize(cvec &Hk, dvec &evals)
{
/**
 *  Diagonalisation of matrix Hk. Stores eigenvalues in real vector evals
     and eigenvectors in complex vector Hk
 */
    zheev_(&jobz, &uplo, &matsize, &Hk[0], &lda, &evals[0], &work[0],
        &lwork, &rwork[0], &info);
   assert(!info);
}
```

- Wrapper function for two dimensional array indices

```
inline int fq(int i, int j, int N)
/**
 *  MAT[i,j] = Vec[fq(i,j,N)] with row index i and column index j
 */
{
    return i*N+j;
}
```

- Wrapper function for block structured Hamiltonian (Pyrochlore)

```
inline int fq(int a, int b, int i, int j)
/**
 *  MAT[a, b, i, j] = Vec[fq(a,b,i,j)] element; a,b in {0,1,2,3} chooses
     site; i,j in {0,1} chooses spin coordinate,
 */
{
   return 8*a + b + 32*i + 4*j;
}
```

- Wrapper function for Floquet Hamiltonian

```
inline int f_FL(int m, int n, int i, int j)
/**
 * Wrapper for Floquet matrix MAT[m, n, i, j],
    (2*m_max+1)x(2*n_max+1)xNATOM*NATOM block matrix element where i,j in
    {0,..,NATOM-1}, m in {-m,...,0,...+m}, n in {-n,...,0,...+n}
 */
{
   return (2*n_max+1)*NATOM*NATOM*m + NATOM*n + (2*n_max+1)*NATOM*i + j;
}
```

- Delta function

```
inline double delta(int a, int b)
{
   if (a==b)
      return 1.;
   else
      return 0.;
}
```

- Matrix product of quadratic matrices: $C = A \cdot B$

```
template <class Vec>
void times(Vec &A, Vec &B, Vec &C)
{
    int dim = sqrt(A.size());
   Vec TEMP(dim*dim);
    // Transposition gives speed up due to avoided line break
   for(int i=0; i<dim; i++) {
       for(int j=0; j<dim; j++) {
          TEMP[fq(j,i,dim)] = B[fq(i,j,dim)];
         }
    }
#ifndef NO_OMP
    #pragma omp parallel for
#endif
   for(int i=0; i<dim; ++i)
   {
      for(int j=0; j<dim; ++j)
```

```
      {
         C[fq(i,j,dim)] = 0.;
         for(int k=0; k<dim; ++k)
         {
            C[fq(i,j,dim)] += A[fq(i,k,dim)]*TEMP[fq(j,k,dim)];
         }
      }
   }
}
```

- Matrix product with Hermitian conjugation of first factor: $C = A^\dagger \cdot B$

```
template <class Vec>
void times_dn(Vec &A, Vec &B, Vec &C)
{
   int dim = sqrt(A.size());
   Vec TEMP1(dim*dim);
   Vec TEMP2(dim*dim);
   // Transposition gives speed up due to avoided line break
   for(int i=0; i<dim; i++) {
      for(int j=0; j<dim; j++) {
         TEMP1[fq(j,i,dim)] = A[fq(i,j,dim)];
         TEMP2[fq(j,i,dim)] = B[fq(i,j,dim)];
      }
   }
#ifndef NO_OMP
   #pragma omp parallel for
#endif
   for(int i=0; i<dim; ++i)
   {
      for(int j=0; j<dim; ++j)
      {
         C[fq(i,j,dim)] = 0.;
         for(int k=0; k<dim; ++k)
         {
            C[fq(i,j,dim)] += conj(TEMP1[fq(i,k,dim)])*TEMP2[fq(j,k,dim)];
         }
      }
   }
}
```

- Matrix product with Hermitian conjugation of second factor: $C = A \cdot B^{\dagger}$

```
template <class Vec>
void times_nd(Vec &A, Vec &B, Vec &C)
{
 int dim = sqrt(A.size());
#ifndef NO_OMP
   #pragma omp parallel for
#endif
   for(int i=0; i<dim; ++i)
   {
      for(int j=0; j<dim; ++j)
      {
         C[fq(i,j,dim)] = 0.;
         for(int k=0; k<dim; ++k)
         {
               C[fq(i,j,dim)] += A[fq(i,k,dim)]*conj(B[fq(j,k,dim)]);
         }
      }
   }
}
```

B Implementation of important functions

B.1 Publication I

Listing 1: Hamiltonian in k-dependent orbital basis

```
void set_Hk(dvec &kvec, dvec &M, cvec &Hk, dvec &MAT_BASIS, double time)
/**
 *  Set k-dependent Hamiltonian
 *  -kvec: Real vector of the 3d irreducible Brilluoin zone
 *  -M: Real[12] vector contains the 4 mean-field 3d pseudpspin vectors
 *  -Hk: Complex vector[64] to store Hamiltonian
 *  -MAT_BASIS: Basis vectors in array of dim[12]
 *  -time: Real time coordinate
 */
{
   // Microscopicly motivated hopping parameters
```

```
double tp = -2.*ts/3.;
double tss = ts*0.08;
double tps = tp*0.08;
double t1 = 0.53 + 0.27*ts;
double t2 = 0.12 + 0.17*ts;
double t1s = 233./2916.*tss - 407./2187.*tps;
double t2s = 1./1458.*tss + 220./2187.*tps;
double t3s = 25./1458.*tss + 460./2187.*tps;

for(int i=0; i<64; i++)
{
   Hk[i] = 0.;
}

for(int a=0; a<4; a++)
{
    // Spin up-up
   Hk[fb(a,a,0,0)] += -U_ramp(time)*( M[fq(2,a,4)] -
       (M[fq(0,a,4)]*M[fq(0,a,4)] + M[fq(1,a,4)]*M[fq(1,a,4)] +
       M[fq(2,a,4)]*M[fq(2,a,4)]));
   // Spin up-down
   Hk[fb(a,a,0,1)] += -U_ramp(time)*( M[fq(0,a,4)] - II*M[fq(1,a,4)]);
   // Spin down-up
   Hk[fb(a,a,1,0)] += -U_ramp(time)*( M[fq(0,a,4)] + II*M[fq(1,a,4)]);

   // Spin down-down
   Hk[fb(a,a,1,1)] += -U_ramp(time)*(-M[fq(2,a,4)] -
       (M[fq(0,a,4)]*M[fq(0,a,4)] + M[fq(1,a,4)]*M[fq(1,a,4)] +
       M[fq(2,a,4)]*M[fq(2,a,4)]));
   for(int b=0; b<4; b++)
   {
       // Nearest-neighbour hopping
       \mathcal{H}^{\mathrm{NN}}_{ab}(\mathbf{k})
      for(int c=0; c<4; c++)
      {
          // Next-nearest-neighbour hopping
          \mathcal{H}^{\mathrm{NNN}}_{abc}(\mathbf{k})
      }
   }
}
```

```
}.
```

Listing 2: Mean-field pseudospin vectors

```
void M_MF(int num_kpoints_BZ, double num_kpoints_BZ_full, vector<cvec> &RHO_0,
    dvec &M, vector<dvec> &kweights, int &numprocs, int &myrank)
/**
 *  Calculation of mean-field pseudospin vectors
 *  -num_kpoints_BZ: # of k-points in BZ_IRR
 *  -num_kpoints_BZ_full: # of k-points of full BZ
 * -RHO_0: Vector of complex vectors[64] for intital desity matrix
 *  -M: Real[12] vector contains the 4 mean-field 3d pseudospin vectors
 *  -kweights: Weights of k-points
 *  -numprocs: # of processes
 *  -myrank: Rank of process
 */
{
   for(int i=0; i<12; i++)
      M[i] = 0.;

   for(int k=myrank; k<num_kpoints_BZ; k+=numprocs)
   {
      for(int a=0; a<NORB; a++)
      {
          // j^x
         M[fq(0,a,4)] += real(1./(num_kpoints_BZ_full*2.)*(RHO_0[k][fb(a, a, 0,
             1)]+RHO_0[k][fb(a, a, 1, 0)]))*(kweights[k][0]);
         // j^y
         M[fq(1,a,4)] += real(1./(num_kpoints_BZ_full*2.)*(-II)*(RHO_0[k][fb(a,
             a,1, 0)]-RHO_0[k][fb(a, a, 0, 1)]))*(kweights[k][0]);
         // j^z
         M[fq(2,a,4)] += real(1./(num_kpoints_BZ_full*2.)*(RHO_0[k][fb(a, a, 0,
             0)]-RHO_0[k][fb(a, a, 1, 1)]))*(kweights[k][0]);
      }
   }
}
```

Listing 3: Self-consistency loop

```
void groundstate(vector<dvec> &kweights, vector<cvec> &RHO_0, dvec &M, cvec &Hk,
```

```
    dvec &evals, vector<dvec> &BZ_IRR, dvec &MAT_BASIS, double &mu, int
    &numprocs, int &myrank)
/**
 * Computes the initial pseudospin vectors and density matrix in a
     self-consistent loop
 *  -kweights: Real vector containing weights of k-points (in case reduced cell
     is used unequal 1)
 * -RHO_0: Vector of complex vectors[64] for intital desity matrix
 *  -M: Real[12] vector contains the 4 mean-field 3d pseudospin vectors
 *  -Hk: Complex vector[64] to store Hamiltonian
 *  -evals: Real vector[8] of eigenvalues
 *  -BZ_IRR: k-points of reduced reciprocal cell
 *  -MAT_BASIS: Vector of real vectors containing basis vectors
 *  -mu: Chemical potential
 *  -numprocs: Total number of processes (MPI)
 *  -myrank: Rank of process (MPI)
 */
{
    // # of k-vectors from sampling of irreducible BZ
   int num_kpoints_BZ = BZ_IRR.size();

   // k-oints of full Brillouin zone
   double num_kpoints_BZ_full = 0.;
   for(int k=0; k<kweights.size(); k++)
      num_kpoints_BZ_full += kweights[k][0];

   int count = 0;
   double m = 0.0;
   double m_old;
   double deviation = 1.0;
   double N_tot, E_tot;
   cvec TEMP(64,0.);

   // Set chemical potential to initial value
   mu = mu_init;

   while(deviation > dev)
   {
      count++;
      m_old = m;
```

```
      N_tot = 0.;
      E_tot = 0.;

      // Calculate particle number per k-point
      for(int k=myrank; k<num_kpoints_BZ; k+=numprocs)
      {
          // Set Hamiltonian matrix
         set_Hk(BZ_IRR[k], M, Hk, MAT_BASIS, 0.0);
         // Diagonalize Hamiltonian matrix
         diagonalize(Hk, evals);
         // Set density matrix in eigenenergy basis and calculate total particel
             number
         for(int i=0; i<8; i++){
            for(int j=0; j<8; j++)
            {
               RHO_0[k][fq(i,j,8)] = fermi(evals[i], mu)*delta(i,j);
               N_tot += fermi(evals[i], mu)*delta(i,j)*kweights[k][0];
               E_tot += N_tot*evals[i];
            }
         }
         times(RHO_0[k], Hk, TEMP);
           times_dn(Hk, TEMP, RHO_0[k]);
      }

      // Calculation of mean-field pseudospin vectors
      M_MF(num_kpoints_BZ, num_kpoints_BZ_full, RHO_0, M, kweights, numprocs,
          myrank);

#ifndef NO_MPI
      MPI_Allreduce(MPI_IN_PLACE, &N_tot, 1, MPI_DOUBLE, MPI_SUM, MPI_COMM_WORLD);
      MPI_Allreduce(MPI_IN_PLACE, &E_tot, 1, MPI_DOUBLE, MPI_SUM, MPI_COMM_WORLD);
      MPI_Allreduce(MPI_IN_PLACE, &M[0], 12, MPI_DOUBLE, MPI_SUM, MPI_COMM_WORLD);
#endif
      // Adjust chemical potential
      mu += -DELTA*(N_tot-num_kpoints_BZ_full*filling);

        // Calculation of magnetic order parameter
      m = 0.;
      for(int a=0; a<4; a++)
      {
```

```
        m += 0.25*sqrt(M[fq(0,a,4)]*M[fq(0,a,4)] + M[fq(1,a,4)]*M[fq(1,a,4)] +
            M[fq(2,a,4)]*M[fq(2,a,4)]);
      }

      // Deviation from former loop -> exit condition
      deviation = abs(m-m_old);
   }
```

Listing 4: Time derivative of density matrix

```
void set_dRHOdt(cvec &TEMP1, cvec &TEMP2, cvec &RHO_t_tk, cvec &dRHO_dt, cvec
    &Hk, dvec &evals, double &mu, double time)
/*
 *  Calculation of the time-derivative of the density matrix
 *  -TEMP1, TEMP2: Complex helper matrix
 *  -RHO_t_tk:Complex vector[64] of k- and time-dependent density matrix
 *  -dRHO_dt: Complex vector[64] of temporal change of density matrix
 *  -Hk: Complex vector[64] to store Hamiltonian
 *  -evals: Real vector[8] of eigenvalues
 *  -mu: chemical potential
 *  -time: double real time coordinate
 */
{
   // Unitary part
   times(Hk, RHO_t_tk, TEMP1);
   times(RHO_t_tk, Hk, TEMP2);
   for(int i=0; i<64; i++)
   {
      dRHO_dt[i] = -II*(TEMP1[i]-TEMP2[i]);
   }
   // Non-unitary part
#ifndef NO_DISS
    diagonalize(Hk, evals);

   for(int i=0; i<64; i++)
      TEMP1[i] = RHO_t_tk[i];

    // Transform Rho(k): orbital basis -> instantaneous energy eigenbasis
   times_nd(TEMP1, Hk, TEMP2);
   times(Hk, TEMP2, TEMP1);
```

```
   // Calculate dRho
   for(int a=0; a<8; a++)
   {
      for(int b=0; b<8; b++)
      {
         TEMP2[fq(a,b,8)] = -2.*J0*(TEMP1[fq(a,b,8)]-fermi_bath(evals[a],
             mu))*delta(a,b) - 2.*J0*TEMP1[fq(a,b,8)]*(1.-delta(a,b));
      }
   }
   // Transform dRho(k): instantaneous energy eigenbasis -> orbital basis
   times(TEMP2, Hk, TEMP1);
   times_dn(Hk, TEMP1, TEMP2);

   for(int i=0; i<64; i++)
   {
      dRHO_dt[i] += TEMP2[i];
   }
#endif
}
```

Listing 5: Two-step Adams-Bashforth propagator

```
void AB2_propatation(dvec &mu_t, dvec &evals, vector<dvec> &kweights,
    vector<cvec> &RHO_0, vector<cvec> &dRHO_dt0, vector<cvec> &dRHO_dt1, dvec &M,
    cvec &Hk, vector<dvec> &BZ_IRR, dvec &MAT_BASIS, vector<cvec*> RHO_t,
    vector<dvec*> M_t, double &mu, int &numprocs, int &myrank)
/**
 * Two-step Adams-Bashforth linear multistep propagator:
 * -mu_t: Real vector to store t.-d. chemical potential
 * -E_TOT: Vector[timesteps] of real vectors[3] to store t.-d. energies
 *  -evals: Real vector[8] of eigenvalues
 * -kweights: Real vector containing weights of k-points (in case reduced cell
     is used unequal 1)*
 * -RHO_0: Vector of complex vectors[64] for intital desity matrix
 * -dRHO_dt0, dRHO_dt1: Vector of complex vectors[64] to store change of density
     matrix
 *  -M: Real[12] vector contains the 4 mean-field 3d pseudospin vectors
 *  -Hk: Complex vector[64] to store Hamiltonian
 * -BZ_IRR: k-points of reduced reciprocal cell
```

```
 * -MAT_BASIS: Real vector[12] of basis vectors
 * -RHO_t_tk: Vector[3] of complex vector pointers[64] to store density matrix
     at 3 subsequent time steps
 * -mu: Chemical potential
 * -numprocs: Total number of processes (MPI)
 * -myrank: Rank of process (MPI)
 */
{
    // # of k-vectors from sampling of irreducible BZ
   int num_kpoints_BZ = BZ_IRR.size();
   // k-oints of full Brillouin zone
   int num_kpoints_BZ_full = 0;
   for(int k=0; k<kweights.size(); k++)
      num_kpoints_BZ_full += kweights[k][0];

   // Temporary variables
   cvec DENSt(16,0.);
   cvec TEMP1(64,0.);
   cvec TEMP2(64,0.);
   cvec TEMP3(64,0.);
   double n_tot;
   dvec N_TOT(timesteps);

   // Pointers for multistep method
   cvec *temp0, *temp1, *temp2;

   // Stepsize
   double h = (endtime-starttime)/timesteps;

   // Initial magnetisation
   for(int i=0; i<12; i++)
   {
      (*M_t[0])[i] = M[i];
   }
   // Read in initial density matrix
   for(int k=0; k<num_kpoints_BZ; k++)
   {
      for(int i=0; i<64; i++)
         (*RHO_t[fq(0, k, num_kpoints_BZ)])[i] = RHO_0[k][i];
   }
```

```
   // Set initial chemical potential
   mu_t[0] = mu;
   N_TOT[0] = filling;

   double time;
   // Propagation
   for(int t=0; t<timesteps-1; t++)
   {
      for(int i=0; i<3; i++)
         E[i] = 0.0;
      // 1st Euler step: y_{n+1} = y_n + hf(t_{n},y_{n})
      if(t==0)
      {
         for(int k=myrank; k<num_kpoints_BZ; k+=numprocs)
         {
            set_Hk(BZ_IRR[k], M, Hk, MAT_BASIS, 0.0);
            set_dRHOdt(TEMP1, TEMP2, RHO_t[fq(0,k,num_kpoints_BZ)][0],
                dRHO_dt0[k], Hk, evals, mu_t[0], 0.0);
            for(int i=0; i<64; i++)
            {
               (*RHO_t[fq(1,k,num_kpoints_BZ)])[i] =
                   (*RHO_t[fq(0,k,num_kpoints_BZ)])[i] + h*dRHO_dt0[k][i];
               RHO_0[k][i] = (*RHO_t[fq(1,k,num_kpoints_BZ)])[i];
            }
         }
         M_MF(num_kpoints_BZ, num_kpoints_BZ_full, RHO_0, M, kweights, numprocs,
             myrank);
         Dens_MF(num_kpoints_BZ, num_kpoints_BZ_full, RHO_0, DENSt, kweights,
             numprocs, myrank);
#ifndef  NO_MPI
         MPI_Allreduce(MPI_IN_PLACE, &M[0], 12, MPI_DOUBLE, MPI_SUM,
             MPI_COMM_WORLD);
         MPI_Allreduce(MPI_IN_PLACE, &DENSt[0], 16, MPI_DOUBLE_COMPLEX, MPI_SUM,
             MPI_COMM_WORLD);
#endif
         for(int i=0; i<12; i++)
         {
            (*M_t[1])[i] = M[i];
         }
         n_tot = 0.0;
```

```
        for(int a=0; a<4; a++)
        {
           n_tot += real(DENSt[fq(a,0,4)]+DENSt[fq(a,3,4)]);
        }
        N_TOT[t+1] = n_tot;
        mu_t[t+1] = mu_t[t]*(N_TOT[0]/N_TOT[t+1]);
     }
     // Two-step Adams-Bashforth method
     else
     {  // 2-step Adams predictor
        for(int k=myrank; k<num_kpoints_BZ; k+=numprocs)
        {
           set_Hk(BZ_IRR[k], M_t[t-1][0], Hk, MAT_BASIS, h*double(t-1));
           set_dRHOdt(TEMP1, TEMP2, RHO_t[fq(0,k,num_kpoints_BZ)][0],
              dRHO_dt0[k], Hk, evals, mu_t[t-1], h*double(t-1));
           set_Hk(BZ_IRR[k], M_t[t][0], Hk, MAT_BASIS, h*double(t));
           set_dRHOdt(TEMP1, TEMP2, RHO_t[fq(1,k,num_kpoints_BZ)][0],
              dRHO_dt1[k], Hk, evals, mu_t[t], h*double(t));
           // P_{n+1} = y_{n} + 3/2*h*f(t_{n},y_{n}) - 0.5*h*f(t_{n-1},y_{n-1})
           for(int i=0; i<64; i++)
           {
              (*RHO_t[fq(2,k,num_kpoints_BZ)])[i] =
                 (*RHO_t[fq(1,k,num_kpoints_BZ)])[i] + h*(3./2.*dRHO_dt1[k][i] -
                 0.5*dRHO_dt0[k][i]);
              RHO_0[k][i] = (*RHO_t[fq(2,k,num_kpoints_BZ)])[i];
           }
        }
        M_MF(num_kpoints_BZ, num_kpoints_BZ_full, RHO_0, M, kweights, numprocs,
           myrank);
#ifndef  NO_MPI
        MPI_Allreduce(MPI_IN_PLACE, &M[0], 12, MPI_DOUBLE, MPI_SUM,
           MPI_COMM_WORLD);
#endif
        // 2-step Moulton corrector
        for(int k=myrank; k<num_kpoints_BZ; k+=numprocs)
        {
           set_Hk(BZ_IRR[k], M, Hk, MAT_BASIS, h*double(t+1));
           set_dRHOdt(TEMP1, TEMP2, RHO_t[fq(2,k,num_kpoints_BZ)][0],
              dRHO_dt0[k], Hk, evals, mu_t[t], h*double(t+1));
           // y_{n+1} = y_{n} + 1/2*h*(f(t_{n+1},P_{n+1}) + f(t_{n},y_{n}))
```

```
            for(int i=0; i<64; i++)
            {
               (*RHO_t[fq(2,k,num_kpoints_BZ)])[i] =
                   (*RHO_t[fq(1,k,num_kpoints_BZ)])[i] + 0.5*h*(dRHO_dt0[k][i] +
                   dRHO_dt1[k][i]);
               RHO_0[k][i] = (*RHO_t[fq(2,k,num_kpoints_BZ)])[i];
            }
            // Cyclic exchange of pointers
            temp0 = RHO_t[fq(0,k,num_kpoints_BZ)];
            temp1 = RHO_t[fq(1,k,num_kpoints_BZ)];
            temp2 = RHO_t[fq(2,k,num_kpoints_BZ)];

            RHO_t[fq(0,k,num_kpoints_BZ)] = temp1;
            RHO_t[fq(1,k,num_kpoints_BZ)] = temp2;
            RHO_t[fq(2,k,num_kpoints_BZ)] = temp0;
         }
         M_MF(num_kpoints_BZ, num_kpoints_BZ_full, RHO_0, M, kweights, numprocs,
             myrank);
         Dens_MF(num_kpoints_BZ, num_kpoints_BZ_full, RHO_0, DENSt, kweights,
             numprocs, myrank);
#ifndef  NO_MPI
         MPI_Allreduce(MPI_IN_PLACE, &M[0], 12, MPI_DOUBLE, MPI_SUM,
             MPI_COMM_WORLD);
         MPI_Allreduce(MPI_IN_PLACE, &DENSt[0], 16, MPI_DOUBLE_COMPLEX, MPI_SUM,
             MPI_COMM_WORLD);
#endif
         n_tot = 0.0;
         for(int a=0; a<4; a++)
         {
            n_tot += real(DENSt[fq(a,0,4)]+DENSt[fq(a,3,4)]);
         }
         N_TOT[t+1] = n_tot;
      }
      // Adjust chemical potential in order to preserve particle number
      mu_t[t+1] = mu_t[t]*(N_TOT[0]/N_TOT[t+1]);
   }
}
```

Listing 6: Lesser Green's function

```
void Tr_Gless(int k, dvec &mu_t, cvec &Hk, dvec &evals, vector<cvec> &UMATRIX,
    dvec &MAT_BASIS, double &mu, vector<dvec> &K_PATH, vector<cvec> &G_HELP, cvec
    &G_Tr, vector<cvec*> RHO_PATH_t, int &myrank)
/**
 * Calculates the trace of the lesser Grrens funtion Tr{G<(k,t,t')}
 * -k: Integer picks k-point from K_PATH
 * -mu_t: Real vector to store t.-d. chemical potential
 *  -Hk: Complex vector[64] to store Hamiltonian
 *  -evals: Real vector[8] of eigenvalues
 *    -UMATRIX: Vector of complex matrices to store unitary mid-point Euler
    propagators
 *    -MAT_BASIS: Basis vectors in array of dimension [4][3]
 *  -mu: Chemical potential of initial state
 *  -K_PATH: vector of high-symmetry path vectors
 *  -G_HELP: Vector of complex vectors[64] needed in computation process
 *    -G_Tr: Complex vector[TIMESTEPS*TIMESTEPS] to store traco of Glesser
    function
 *    -RHO_PATH_t: Vector of complex vector pointers containing propagated
    density matrices of K_PATH
 *  -myrank: Rank of process (MPI)
 */
{
   dvec M0(12,0.);
   cvec TEMP1(64);
   cvec TEMP2(64);
   vector<dvec> M_t(timesteps, dvec(12));

   // Load time-dependent magnetic order from prior calculation
   ifstream in("M_t.txt");
   if (!in)
   {
      cout << "Cannot open file.\n";
      return;
   }
   for(int t=0; t<timesteps-1; t++)
   {
      for(int i=0; i<12; i++)
      {
         in >> M_t[t][i];
      }
```

```
}
in.close();
in.clear();

// Load time-dependent chemical potential
in.open("mu_t.txt");
if (!in)
{
   cout << "Cannot open file.\n";
   return;
}
for(int t=0; t<timesteps-1; t++)
{
   in >> mu_t[t];
}
in.close();
in.clear();

// Propagation of density matrix
PROP_PATH(k, evals, Hk, K_PATH, MAT_BASIS, M_t, RHO_PATH_t, mu_t);

// Stepsize for reduced number timesteps
double h = (endtime-starttime)/TIMESTEPS;
int time_fac = timesteps/TIMESTEPS;

// Set unitary mid-point Euler propagators in k-dependent orbital basis:
 for(int t=0; t<TIMESTEPS-1; t++)
{
   set_Hk(K_PATH[k], M_t[t*time_fac], TEMP1, MAT_BASIS, h*double(t));
   set_Hk(K_PATH[k], M_t[(t+1)*time_fac], TEMP2, MAT_BASIS, h*double(t+1));
   for(int i=0; i<64; i++)
      Hk[i] = 0.5*(TEMP1[i]+TEMP2[i]);
   diagonalize(Hk, evals);
   for(int i=0; i<8; i++)
   {
      for(int j=0; j<8; j++)
      {
         TEMP1[fq(i,j,8)] = exp(+II*evals[i]*h)*delta(i,j);
      }
   }
```

```
      // Back-transformation to original k-orbital basis
      times(TEMP1, Hk, TEMP2);
      times_dn(Hk, TEMP2, UMATRIX[t]);
   }
   // Clear memeory
   for(int tt=0; tt<TIMESTEPS*TIMESTEPS; tt++)
      G_Tr[tt] = 0.0;

   // Set G<(k,t,tp)
   for(int td=0; td<TIMESTEPS-1; td++)
   {
      // Set diagonal (t==t") value of Greens function: G<(t,t') = i*rho(t)
      for(int i=0; i<64; i++)
      {
         G_HELP[td][i] = II*(*RHO_PATH_t[td*time_fac])[i];
      }
      // Calculate trace
      G_Tr[fq(td, td, TIMESTEPS)] = 0.0;
         for(int i=0; i<8; i++)
            G_Tr[fq(td, td, TIMESTEPS)] += G_HELP[td][fq(i,i,8)];
      // Propagation in t direction
      for(int t=0; t<TIMESTEPS-td-1; t++)
      {
         times(G_HELP[td+t], UMATRIX[td+t], G_HELP[td+t+1]);
         G_Tr[fq(td+t+1, td, TIMESTEPS)] = 0.0;
         for(int i=0; i<8; i++)
            G_Tr[fq(td+t+1, td, TIMESTEPS)] += G_HELP[td+t+1][fq(i,i,8)];
      }
      // Propagation in t' direction
      for(int tp=0; tp<TIMESTEPS-td-1; tp++)
      {
         times_dn(UMATRIX[td+tp], G_HELP[td+tp], G_HELP[td+tp+1]);
         G_Tr[fq(td, td+tp+1, TIMESTEPS)] = 0.0;
         for(int i=0; i<8; i++)
            G_Tr[fq(td, td+tp+1, TIMESTEPS)] += G_HELP[td+tp+1][fq(i,i,8)];
      }
   }
}
```

Listing 7: Energy-resolved photocurrent

```
    double Iphoto(double omega, cvec &G_Tr)
/**
 * Calculate Photo current from Tr_Gless()
 *    -omega: probing frequency
 *  -G_Tr: Complex vector[TIMESTEPS x TIMESTEPS] to store traco of Glesser
     function
 */
{
   double h = (endtime-starttime)/TIMESTEPS;
   double Iph;
   dvec TEMP(TIMESTEPS);

   for(int tp=0; tp<TIMESTEPS; tp++)
   {
      TEMP[tp] = 0.0;
      for(int t=0; t<TIMESTEPS-1; t++)
      {
         if(gauss(double(t)*h, T_PROBE, SIGMA_PROBE)*gauss(double(tp)*h,
             T_PROBE,SIGMA_PROBE)*(2.*PI*pow(SIGMA_PROBE, 2))<weightcutoff)
            continue;
         TEMP[tp] += 0.5*h*imag( gauss(double(t)*h, T_PROBE,
             SIGMA_PROBE)*gauss(double(tp)*h, T_PROBE, SIGMA_PROBE)
                    *exp(-II*omega*double(t-tp)*h)*G_Tr[fq(t, tp, TIMESTEPS)]
                    +gauss(double(t+1)*h, T_PROBE,
                        SIGMA_PROBE)*gauss(double(tp)*h, T_PROBE, SIGMA_PROBE)
                    *exp(-II*omega*double(t+1-tp)*h)*G_Tr[fq(t+1, tp,
                        TIMESTEPS)]);
      }
   }
   Iph = 0.0;
   for(int tp=0; tp<TIMESTEPS-1; tp++)
   {
      Iph += 0.5*h*(TEMP[tp]+TEMP[tp+1]);
   }
   return Iph;
}
```

B.2 Publication II

Listing 8: Hamiltonian in k-dependent orbital basis

```
    void set_Hk(double k, cvec &Hk, double time)
/**
 * Set time-dependent Hamiltonian matrix with Peierls field
 *  -k: Real vector of the reciprocal space
 *  -Hk: Complex vector[NATOM*NATOM] to store Hamiltonian
 *  -time: time variable
 */
{
   for(int i=0; i<8; ++i)
           for(int j=0; j<8; ++j)
               Hk[fq(i,j,8)] = 0.;

    // Diagonal elements
   Hk[fq(0,0,8)] = eO;
   Hk[fq(1,1,8)] = eI;
   Hk[fq(2,2,8)] = eI;
   Hk[fq(3,3,8)] = eO;
   Hk[fq(4,4,8)] = eO;
   Hk[fq(5,5,8)] = eI;
   Hk[fq(6,6,8)] = eI;
   Hk[fq(7,7,8)] = eO;

   // Hopping elements
   // Lower triagonal
   Hk[fq(7,0,8)] += -tOd*exp(-II*Ax_t(time))*exp(+II*k);
   Hk[fq(1,0,8)] +=
       -tIO*exp(+II*(-Ax_t(time)-sqrt(3.)*Ay_t(time))/2.)*exp(+II*k/2.);
   Hk[fq(7,1,8)] +=
       -tIO*exp(+II*(-Ax_t(time)+sqrt(3.)*Ay_t(time))/2.)*exp(+II*k/2.);
   Hk[fq(6,1,8)] += -tI2*exp(-II*Ax_t(time))*exp(+II*k);
   Hk[fq(2,1,8)] +=
       -tI1*exp(+II*(-Ax_t(time)-sqrt(3.)*Ay_t(time))/2.)*exp(+II*k/2.);
   Hk[fq(6,2,8)] +=
       -tI1d*exp(+II*(-Ax_t(time)+sqrt(3.)*Ay_t(time))/2.)*exp(+II*k/2.);
   Hk[fq(5,2,8)] += -tI2*exp(-II*Ax_t(time))*exp(+II*k);
```

```
  Hk[fq(3,2,8)] +=
     -tI0*exp(+II*(-Ax_t(time)-sqrt(3.)*Ay_t(time))/2.)*exp(+II*k/2.);
  Hk[fq(5,3,8)] +=
     -tI0*exp(+II*(-Ax_t(time)+sqrt(3.)*Ay_t(time))/2.)*exp(+II*k/2.);
  Hk[fq(4,3,8)] += -tOd*exp(-II*Ax_t(time))*exp(+II*k);
  Hk[fq(5,4,8)] +=
     -tI0*exp(+II*(+Ax_t(time)+sqrt(3.)*Ay_t(time))/2.)*exp(-II*k/2.);
  Hk[fq(6,5,8)] +=
     -tI1*exp(+II*(+Ax_t(time)+sqrt(3.)*Ay_t(time))/2.)*exp(-II*k/2.);
  Hk[fq(7,6,8)] +=
     -tI0*exp(+II*(+Ax_t(time)+sqrt(3.)*Ay_t(time))/2.)*exp(-II*k/2.);
  Hk[fq(4,3,8)] += -tO*exp(+II*Ax_t(time))*exp(-II*1.*k);
  Hk[fq(4,2,8)] +=
     -tI0*exp(-II*(-Ax_t(time)+sqrt(3.)*Ay_t(time))/2.)*exp(-II*k/2.);
  Hk[fq(5,2,8)] += -tI2*exp(+II*Ax_t(time))*exp(-II*1.*k);
  Hk[fq(5,1,8)] +=
     -tI1d*exp(-II*(-Ax_t(time)+sqrt(3.)*Ay_t(time))/2.)*exp(-II*k/2.);
  Hk[fq(6,1,8)] += -tI2*exp(+II*Ax_t(time))*exp(-II*1.*k);
  Hk[fq(6,0,8)] +=
     -tI0*exp(-II*(-Ax_t(time)+sqrt(3.)*Ay_t(time))/2.)*exp(-II*k/2.);
  Hk[fq(7,0,8)] += -tO*exp(+II*Ax_t(time))*exp(-II*1.*k);

  // Upper triagonal
  (...Hk[fq(j,i,8)]=conj(Hk[fq(i,j,8)]...)
}
```

Listing 9: Mid-point Euler propagator

```
    void Propagation(cvec &Hk, dvec &evals, vector<cvec> &UMATRIX, double &mu,
        dvec &BZ, vector<cvec> &RHO_t, dvec ETOT_t, int &numprocs, int &myrank)
/**
 * Mid-point Euler propagation scheme for density matrix:
 *  -Hk: Complex vector[64] to store Hamiltonian
 *  -evals: Real vector[8] of eigenvalues
 *  -UMATRIX: Vector[TIMESTPES] of complex vectors[64] to store propagators
 *    -mu: chemical potential
 *  -BZ: k-points of reduced 1d reciprocal cell
 * -RHO_t: Vector[TIMESTPES] of complex vector[64] to store t.-d. density matrix
 *  -ETOT_t: Real vector[TIMESTEPS] to store total t.-d. total energy
 * -numprocs: Total number of processes (MPI)
```

```
 * -myrank: Rank of process (MPI)
 */
{
   double h = (endtime-starttime)/TIMESTEPS;

   cvec TEMP1(64);
   cvec TEMP2(64);

   for(int t=0; t<TIMESTEPS; t++)
      ETOT_t[t] = 0.0;

   // Calculation of mid-point Euler propagators U(t+dt,t)
   for(int k=myrank; k<NN; k+=numprocs)
   {
      if(myrank==0) cout << "k = " << k << endl;
      for(int t=0; t<TIMESTEPS-1; t++)
      {
         set_Hk(BZ[k], TEMP1, h*double(t));
         set_Hk(BZ[k], TEMP2, h*double(t+1));
         for(int i=0; i<64; i++)
            Hk[i] = 0.5*(TEMP1[i]+TEMP2[i]);
         diagonalize(Hk, evals);
         for(int i=0; i<8; i++)
         {
            for(int j=0; j<8; j++)
            {
               TEMP1[fq(i,j,8)] = exp(+II*evals[i]*h)*delta(i,j);
            }
         }
         times(TEMP1, Hk, TEMP2);
         times_dn(Hk, TEMP2, UMATRIX[t]);
      }
      // Set initial Density in k-orbital basis
      set_Hk(BZ[k], Hk, starttime);
      diagonalize(Hk, evals);
      for(int i=0; i<8; i++)
      {
         for(int j=0; j<8; j++)
         {
            RHO_t[0][fq(i,j,8)] = fermi(evals[i], mu)*delta(i,j);
```

```
        }
      }
      times(RHO_t[0], Hk, TEMP1);
      times_dn(Hk, TEMP1, RHO_t[0]);

      // Stepwise propagation of initial density operator by unitary midpoint
          propagators
      for(int t=0; t<TIMESTEPS-1; t++)
      {
         times(RHO_t[t], UMATRIX[t], TEMP1);
         times_dn(UMATRIX[t], TEMP1, RHO_t[t+1]);
         set_Hk(BZ[k], Hk, h*double(t));
         times(RHO_t[t], Hk, TEMP1);
         for(int i=0; i<8; i++)
         {
            ETOT_t[t] += real(TEMP1[fq(i,i,8)])/double(NN);
         }
      }
      ETOT_t[TIMESTEPS-1] = ETOT_t[TIMESTEPS-2];
   }
   MPI_Allreduce(MPI_IN_PLACE, &ETOT_t[0], TIMESTEPS, MPI_DOUBLE, MPI_SUM,
       MPI_COMM_WORLD);
}
```

B.3 Publication III

Listing 10: Creation of Moiré lattice

```
// Cell index
ii = 6
N = 4*(ii**2+(ii+1)*ii+(ii+1)**2)
// Lattice constant in Angstroem
lconst = 2.445
// Interlayer distance in Angstroem
dis = 3.364

a = ii+1
b = ii
```

```
angle1 = np.arctan2((b*np.sqrt(3.)/2.),(a+b/2.))
angle2 = angle1 + np.pi/3.

d = np.sqrt(b**2*3./4.+(a+b/2.)**2)
ep2x = a+b/2.+d*np.sin(np.pi/6.-angle1)
ep2y = b*np.sqrt(3.)/2.+d*np.cos(np.pi/6.-angle1)
slope = ep2y/ep2x

// Bravais superlattice vectors
lvec = np.zeros((2,2))
lvec[0,0] = d*np.cos(angle1)
lvec[0,1] = d*np.sin(angle1)
lvec[1,0] = d*np.sin(np.pi/6.-angle1)
lvec[1,1] = d*np.cos(np.pi/6.-angle1)

c1 = int(np.round(ep2x)) + 1
c2 = int(np.round(ep2y/np.sqrt(3.))) + 1
// Array to store atomic positions (x,y,z) and sublattice index (0,1)
MAT_CELL = np.zeros((N,4))

pp=1 # number of set sites-1

// Generate atomic sites
// Generation of lower lattice
for i in range(1,c1+1):
    for j in range(1,c2+1):
        ax=i-1.
        ay=(j-1.)*np.sqrt(3.)
        e1=np.arctan2(ay,ax)
        e2=np.arctan2((ep2y-ay),(ep2x-ax))
        if(e1>angle1 and e1<angle2 and e2<angle2 and e2>angle1 and ax-ep2x<0.0):
            MAT_CELL[pp,:] = np.array([ax,ay,0.0,0.0])
            pp=pp+1
        ax=i-1.
        ay=(j-1.)*np.sqrt(3.)+np.sqrt(3.)/3.
        e1=np.arctan2(ay,ax);
        e2=np.arctan2((ep2y-ay),(ep2x-ax))
        if(e1>angle1 and e1<angle2 and e2<angle2 and e2>angle1 and ax-ep2x<0.0):
            MAT_CELL[pp,:] = np.array([ax,ay,0.0,1.0])
            pp=pp+1
```

```
        ax=i-1.+0.5
        ay=(j-1.)*np.sqrt(3.)+np.sqrt(3.)/3.*1.5
        if (ep2x-ax==0.):
            e2=1.
        else:
            e1=np.arctan2(ay,ax)
            e2=np.arctan2((ep2y-ay),(ep2x-ax))
        if(e1>angle1 and e1<angle2 and e2<angle2 and e2>angle1 and ax-ep2x<0.0):
            MAT_CELL[pp,:] = np.array([ax,ay,0.0,0.0])
            pp=pp+1
        ax=i-1.+0.5
        ay=(j-1.)*np.sqrt(3.)+np.sqrt(3.)/3.*2.5
        e1=np.arctan2(ay,ax);
        e2=np.arctan2((ep2y-ay),(ep2x-ax))
        if(e1>angle1 and e1<angle2 and e2<angle2 and e2>angle1 and ax-ep2x<0.0):
            MAT_CELL[pp,:] = np.array([ax,ay,0.0, 1.0])
            pp=pp+1

// Generation of upper lattice
for i in range(pp,N):
    ax=MAT_CELL[i-pp,0]*(1.-slope**2.)/(1.+slope**2.)
       +MAT_CELL[i-pp,1]*2.*slope/(1.+slope**2.)
    ay=MAT_CELL[i-pp,0]*2.*slope/(1.+slope**2)
       +MAT_CELL[i-pp,1]*(slope**2.-1.)/(1.+slope**2.)
    az=dis/lconst
    sli=MAT_CELL[i-pp,3]
    MAT_CELL[i,:] = np.array([ax,ay,az,sli])
```

Listing 11: Peierls field

```
inline double Ax/Ay/Az_t(double time)
{
/**
 * Peierls field for electrons in Ax/Ay/Az-direction:
 *  -time: Real time coordinate
 */
   return Ax/Ay/Az_peierls*sin(w_peierls*time);
}
```

Listing 12: Set Hamiltonian in k-dependent orbital basis

```
void set_Hk(dvec &kvec, cvec &Hk, const dvec &lvec, vector<dvec> &UNIT_CELL,
    double time)
/**
 * Set time-dependent Hamiltonian matrix with Peierls field
 *  -kvec: Real vector of the reciprocal space
 *  -Hk: Complex vector[NATOM*NATOM] to store Hamiltonian
 *  -lvec: Real vector[4] of superlattice Bravais translational vectors (in
     lconst*Angstroem)
 *  -UNIT_CELL: Vector[NATOM] of real vectors[4] containing atomic positions and
     sublattice info
 *  -time: time variable
 */
{
   const double lcell = lconst*sqrt(pow(lvec[0],2.)+pow(lvec[1],2.));
   const double qq2 = qq1*aa2/aa1 ;
   const double kx = kvec[0];
   const double ky = kvec[1];

    // Bottom layer
#ifndef NO_OMP
    #pragma omp parallel
   {
#endif
   double d, rx, ry, rz;
#ifndef NO_OMP
   #pragma omp for
#endif
   for(int m=0; m<NATOM*NATOM; m++){
       Hk[m] = 0.0;
    }
#ifndef NO_OMP
   #pragma omp for
#endif
   for(int i=0; i<NATOM/2; ++i)
   {
      // Backgate voltage
      Hk[fq(i,i,NATOM)] = VV/2.;
      // Sublattice potential
      if (UNIT_CELL[i][3] < 0.9){
```

```
        Hk[fq(i,i,NATOM)] += -dgap/2.;
       }
       else{
          Hk[fq(i,i,NATOM)] += dgap/2.;
       }
     for(int j=i+1; j<NATOM/2; ++j)
     {
        for(int m=0; m<3; ++m)
        {
           for(int n=0; n<3; ++n)
           {
              rx = UNIT_CELL[i][0]-UNIT_CELL[j][0]+double(m-1)
                   *lvec[0]+double(n-1)*lvec[2];
              ry = double(m-1)*lvec[1]+UNIT_CELL[i][1]
                   -UNIT_CELL[j][1]+double(n-1)*lvec[3];
              rz = UNIT_CELL[i][2]-UNIT_CELL[j][2];
                  d = lconst*sqrt(pow(rx,2.)+pow(ry,2.)+pow(rz,2.));
                  // Vpp_pi term
              Hk[fq(i,j,NATOM)] += t1/RG*exp(qq1*(1.-(d/aa1)))
                                   *exp(II*(kx*lconst*rx+ky*lconst*ry))
                                   *exp(-II*(Ax_t(time)*rx+Ay_t(time)*ry));
           }
        }
        Hk[fq(j,i,NATOM)] = conj(Hk[fq(i,j,NATOM)]);
     }
   }
   // Top layer
#ifndef NO_OMP
   #pragma omp for
#endif
   for(int i=NATOM/2; i<NATOM; ++i)
   {
      // Top-gate voltage
      Hk[fq(i,i,NATOM)] = -VV/2.;
      // Sublattice potential
      if (UNIT_CELL[i][3] < 0.9){
         Hk[fq(i,i,NATOM)] += -dgap/2.;
       }
       else{
          Hk[fq(i,i,NATOM)] += dgap/2.;
```

```
        }
      for(int j=i+1; j<NATOM; ++j)
      {
         for(int m=0; m<3; ++m)
         {
            for(int n=0; n<3; ++n)
            {
               rx = UNIT_CELL[i][0]-UNIT_CELL[j][0]+double(m-1)
                    *lvec[0]+double(n-1)*lvec[2];
               ry = double(m-1)*lvec[1]+UNIT_CELL[i][1]
                    -UNIT_CELL[j][1]+double(n-1)*lvec[3];
               rz = UNIT_CELL[i][2]-UNIT_CELL[j][2]; ;
                   d = lconst*sqrt(pow(rx,2.)+pow(ry,2.)+pow(rz,2.));
                   // Vpp_pi term
               Hk[fq(i,j,NATOM)] += t1/RG*exp(qq1*(1.-(d/aa1)))
                                    *exp(II*(kx*lconst*rx+ky*lconst*ry))
                                    *exp(-II*(Ax_t(time)*rx+Ay_t(time)*ry));
            }
         }
         Hk[fq(j,i,NATOM)] = conj(Hk[fq(i,j,NATOM)]);
      }
   }
   // Inter-layer terms
#ifndef NO_IC
#ifndef NO_OMP
   #pragma omp for
#endif
   for(int i=0; i<NATOM/2; ++i)
   {
      for(int j=NATOM/2; j<NATOM; ++j)
      {
         for(int m=0; m<3; ++m)
         {
            for(int n=0; n<3; ++n)
            {
               rx = UNIT_CELL[i][0]-UNIT_CELL[j][0]+double(m-1)
                    *lvec[0]+double(n-1)*lvec[2];
               ry = double(m-1)*lvec[1]+UNIT_CELL[i][1]
                    -UNIT_CELL[j][1]+double(n-1)*lvec[3];
               rz = UNIT_CELL[i][2]-UNIT_CELL[j][2];
```

```
                d = lconst*sqrt(pow(rx,2.)+pow(ry,2.)+pow(rz,2.));
              // Vpp_pi term
              Hk[fq(i,j,NATOM)] += (1.-pow(aa2/d,2.))*t1/RG*exp(qq1*(1.-(d/aa1)))
                                   *exp(II*(kx*lconst*rx+ky*lconst*ry))
                                   *exp(-II*(Ax_t(time)*rx+Ay_t(time)*ry+Az_t(time)*rz));
              // Vpp_sigma term
              Hk[fq(i,j,NATOM)] += pow(aa2/d,2.)*t2*exp(qq2*(1.-(d/aa2)))
                                   *exp(II*(kx*lconst*rx+ky*lconst*ry))
                                   *exp(-II*(Ax_t(time)*rx+Ay_t(time)*ry+Az_t(time)*rz));
            }
          }
          Hk[fq(j,i,NATOM)] = conj(Hk[fq(i,j,NATOM)]);
        }
      }
#endif
#ifndef NO_OMP
    }
#endif
}
```

Listing 13: Equilibrium Berry curvature

```
void EQ_BC_LOOP(dvec kvec, double kmin, double kmax, int Nk, cvec &Hk, const
    dvec &lvec, vector<dvec> &UNIT_CELL, dvec &evals, dvec &bands_BCs)
/**
 *    Calculate local Berry curvature in equlibrium for single k-point by phase
     along loop around point divided by area
 *  -kvec: Real vector of the reciprocal space
 *    -kmin: Double to set loop around kvec
 *  -kmax: Double to set loop around kvec
 *    -Nk: Nk-1 defines number of used plaquettes (usually 2 --> 1 plaquette)
 *  -Hk: Complex vector[NATOM x NATOM] to store Hamiltonian
 *  -lvec: Real vector[4] of superlattice Bravais translational vectors (in
     lconst*Angstroem)
 *  -UNIT_CELL: Vector[NATOM] of real vectors[4] containing atomic positions and
     sublattice info
 *  -evals: Real vector[NATOM] to store eigenvalues
 *    -bands_BCs: Real vector[NATOM] to store band Berry curvature
 */
{
```

```
double dk = (kmax-kmin)/double(Nk-1);
cdouble temp1, temp2, temp3, temp4;
dvec k0(2);
vector<cvec*> S_ARRAY(Nk*Nk);
for(int n=0; n<Nk*Nk; n++)
   S_ARRAY[n] = new cvec(NATOM*NATOM);

// Set k-point of lower right corner of loop
k0[0] = kvec[0]-0.5*(kmax-kmin);
k0[1] = kvec[1]-0.5*(kmax-kmin);

// Calculate eigenvectors of Hamiltonian at grid points along loop
for(int i=0; i<Nk; i++)
{
   kvec[0] = k0[0]+i*dk;
   for(int j=0; j<Nk; j++)
   {
      kvec[1] = k0[1]+j*dk;
      set_Hk0(kvec, S_ARRAY[fq(i,j,Nk)][0], lvec, UNIT_CELL);
      diagonalize(S_ARRAY[fq(i,j,Nk)][0], evals);
   }
}
// Calculate Berry phase around loop
// Loop over bands
for(int n=0; n<NATOM; n++)
{
   bands_BCs[n] = 0.;
   // Loops over bands point of momentum loop
   for(int i=0; i<Nk-1; i++)
   {
      for(int j=0; j<Nk-1; j++)
      {
         temp1 = 0.;
         temp2 = 0.; https://www.overleaf.com/project/5d4aa39a3598c93ff9455df5
         temp3 = 0.;
         temp4 = 0.;
         // Calculation of Berry phase
         for(int a=0; a<NATOM; ++a)
         {
            temp1 += conj((*S_ARRAY[fq(i,j,Nk)])[fq(n,a,NATOM)])
```

```
                    *(*S_ARRAY[fq(i+1,j,Nk)])[fq(n,a,NATOM)];
            temp2 += conj((*S_ARRAY[fq(i+1,j,Nk)])[fq(n,a,NATOM)])
                    *(*S_ARRAY[fq(i+1,j+1,Nk)])[fq(n,a,NATOM)];
            temp3 += conj((*S_ARRAY[fq(i+1,j+1,Nk)])[fq(n,a,NATOM)])
                    *(*S_ARRAY[fq(i,j+1,Nk)])[fq(n,a,NATOM)];
            temp4 += conj((*S_ARRAY[fq(i,j+1,Nk)])[fq(n,a,NATOM)])
                    *(*S_ARRAY[fq(i,j,Nk)])[fq(n,a,NATOM)];
          }
          bands_BCs[n] += imag(log(temp1*temp2*temp3*temp4))/pow(kmax-kmin,2.);
        }
      }
   }
   for(int n=0; n<Nk*Nk; n++)
   {
      delete S_ARRAY[n];
   }
}
```

Listing 14: Calculation of Floquet eigenstates

```
void Hk_bands_Floquet(dvec &BANDS_FLOQUET, dvec &OVERLAP_FLOQUET, cvec
    &Hk_FLOQUET, dvec &evals_FLOQUET, vector<dvec> &K_PATH, vector<dvec>
    &UNIT_CELL, const dvec &lvec, int &numprocs, int &myrank)
/**
 * Calculate Floquet bands by truncated expansion in Floquet eigenfunctions
 *  -BANDS_FLOQUET: Real vector to store Floquet eigenvalues of all k-points
 *  -OVERLAP_FLOQUET: Real vector[num_kpoints_PATHxNATOMx(2*n_max+1)] to store
     overlap ov Flquet bands with equilibrium bands
 *  -Hk_FLOQUET: Complex vector[(2*m_max+1)x(2*n_max+1)xNATOMxNATOM] to store
     Flqoeut Hamiltonian matrix
 *  -evals_FLOQUET: Real vector[(M_max+1) x NATOM] to store Floquet eigenvalues
 *  -K_PATH: vector of high-symmetry path vectors
 *  -UNIT_CELL: Vector[NATOM] of real vectors[4] containing atomic positions and
     sublattice info
 *  -lvec: Real vector[4] of superlattice bravis translational vectors (in
     lconst*Angstroem)
 * -numprocs: Total number of processes (MPI)
 * -myrank: Rank of process (MPI)
 */
{
```

```
   const int num_kpoints_path = K_PATH.size();
   const double T = 2.*M_PI/w_peierls;
   const double dt = T/double(timesteps_F-1);

   cvec *TEMP1 = new cvec(NATOM*NATOM);
   cvec *TEMP2 = new cvec(NATOM*NATOM);
   double temp;

   cvec H0(NATOM*NATOM);
   dvec evals(NATOM);
   cdouble tempc;

   for(int k=myrank; k<num_kpoints_path; k+=numprocs)
   {
#ifndef NO_OMP
   #pragma omp parallel for collapse(4)
#endif
       // Empty momory
      for(int m=-m_max; m<m_max+1; m++)
      {
         for(int n=-n_max; n<n_max+1; n++)
         {
            for(int i=0; i<NATOM; i++)
            {
               for(int j=0; j<NATOM; j++)
               {
                  Hk_FLOQUET[f_FL(m+m_max, n+n_max, i, j)] = 0.0;
               }
            }
         }
      }
      if(myrank==0) cout << endl;
      if(myrank==0) cout << "k = " << k << endl;
      // Perform integration over one period T
      for(double t=0; t<T-dt/2.; t+=dt)
      {
         if(myrank==0) cout << "time step: " << t/dt << endl;

         set_Hk(K_PATH[k], TEMP1[0], lvec, UNIT_CELL, t);
         set_Hk(K_PATH[k], TEMP2[0], lvec, UNIT_CELL, t+dt);
```

```
        for(int m=-m_max; m<m_max+1; m++)
        {
           for(int n=-n_max; n<n_max+1; n++)
           {
#ifndef NO_OMP
        #pragma omp parallel for
#endif
              for(int i=0; i<NATOM; i++)
              {
                 for(int j=0; j<NATOM; j++)
                 {
                 Hk_FLOQUET[f_FL(m+m_max, n+n_max, i, j)] +=
                     0.5/T*(exp(II*w_peierls*double(m-n)*t)*(*TEMP1)[fq(i,j,NATOM)]
                     +
                     exp(II*w_peierls*double(m-n)*(t+dt))*(*TEMP2)[fq(i,j,NATOM)])*dt
                     +
                     double(m)*w_peierls*delta(i,j)*delta(m,n)/double(timesteps_F-1);
                 }
              }
           }
        }
     }
     // Diagonalize Floquet Hamiltonian --> eigenvalues and eigenvectors
     diagonalize_F(Hk_FLOQUET, evals_FLOQUET);
     for(int jj=0; jj<NATOM*(2*n_max+1); jj++)
     {
        BANDS_FLOQUET[fq(k,jj,NATOM*(2*n_max+1))] = evals_FLOQUET[jj];
     }
     // Calculate squared overlap with equilibrium states
     set_Hk0(K_PATH[k], H0, lvec, UNIT_CELL);
     diagonalize(H0, evals);
     for(int i=0; i<NATOM*(2*n_max+1); ++i)
     {
        temp = 0.;
        for(int w=0; w<NATOM; ++w)
        {
           tempc = 0.;
           for(int j=0; j<NATOM; ++j)
           {
              tempc += Hk_FLOQUET[fq(i,NATOM*n_max-1+j,NATOM*(2*n_max+1))]
```

```
                        *conj(H0[fq(w,j,NATOM)]);
            }
            temp += real(tempc*conj(tempc));
          }
          OVERLAP_FLOQUET[fq(k,i,NATOM*(2*n_max+1))] = temp;
      }
    }
    delete TEMP1, TEMP2;
#ifndef NO_MPI
      MPI_Allreduce(MPI_IN_PLACE, &BANDS_FLOQUET[0],
          NATOM*(2*n_max+1)*num_kpoints_path, MPI_DOUBLE, MPI_SUM,
          MPI_COMM_WORLD);
      MPI_Allreduce(MPI_IN_PLACE, &OVERLAP_FLOQUET[0],
          NATOM*(2*n_max+1)*num_kpoints_path, MPI_DOUBLE, MPI_SUM,
          MPI_COMM_WORLD);
#endif
```

B.4 SP II

Listing 15: Self-consistent calculation of initial state

```
void groundstate(double &u, double &p, dvec &evals, cvec &Hk, dvec &BZ,
    vector<cvec> &RHO_0, vector<dvec> &E_TOT, int &numprocs, int &myrank)
/**
 * Calculate initial displacement u0
 *  -u: nuclear displacement
 *  -p: nuclear momentum
 *  -evals: Real vector[2] of eigenvalues
 *  -Hk: Complex vector[4] to store Hamiltonian
 *  -BZ: Real vector[NN/2] of 1d reduced Brilluoin zone
 *  -RHO_0: Vector[num_k] of real vectors[4] to store density matrix
 *  -numprocs: Total number of processes (MPI)
 *  -myrank: Rank of process (MPI)
 */
{
   int count = 0;                                          // count # of
       loops of self-consistency
   u = u_init;
```

```
   double N_tot;
   double u_old;
   double deviation = 1.0;

   double E_tot;
   double E_nuc;

   cvec TEMP(4);

   while(deviation > dev)
   {
      count++;
      u_old = u;
      N_tot = 0.;
      E_tot = 0.;

        // Calculation of density-matrix in orbital basis
      set_Rhok(u, evals, Hk, BZ, RHO_0, numprocs, myrank);
      // Calculation of deimerisation u from density matrix
      SET_u0(u, Hk, BZ, RHO_0, numprocs, myrank);

      deviation = abs(u-u_old);

      for(int k=myrank; k<NN/2; k+=numprocs)
      {
         // Calculation of total electronic energy per unit cell (1 electron per
            unit cell)
         set_Hk0(BZ[k], u, Hk);
         times(RHO_0[k], Hk, TEMP);
         E_tot += real(TEMP[fq(0,0,2)]+TEMP[fq(1,1,2)])/(double(NN)/2.);
         N_tot += real(RHO_0[k][fq(0,0,2)]+RHO_0[k][fq(1,1,2)])/(double(NN)/2.);
      }
#ifndef NO_MPI
      MPI_Allreduce(MPI_IN_PLACE, &E_tot, 1, MPI_DOUBLE, MPI_SUM, MPI_COMM_WORLD);
      MPI_Allreduce(MPI_IN_PLACE, &N_tot, 1, MPI_DOUBLE, MPI_SUM, MPI_COMM_WORLD);
#endif
      // Energy of nuclear system per unit cell (2 atoms per unit cell)
      E_nuc = 2.*2.*K*u*u;
   }
   E_TOT[0][0] = E_tot;
```

```
   E_TOT[0][1] = E_nuc;
   p=0.0;
}
```

Listing 16: Ehrenfest propagation with Two-step Adams-Bashforth method

```
void set_dRHOdt(cvec &TEMP1, cvec &TEMP2, cvec &RHO_t_tk, cvec &dRHO_dt, cvec
    &Hk)
/**
 *  Calculation of the time-derivative of the density matrix
 *  -TEMP1, TEMP2: Complex helper matrix
 *  -RHO_t_tk: Complex vector[4] of k- and time-dependent density matrix
 *  -dRHO_dt: Complex vector[4] of temporal change of density matrix
 *  -Hk: Complex vector[4] to store Hamiltonian matrix
 */
{
   // COHERENT PART
   times(Hk, RHO_t_tk, TEMP1);
   times(RHO_t_tk, Hk, TEMP2);
   for(int i=0; i<4; i++)
   {
      dRHO_dt[i] = -II*(TEMP1[i]-TEMP2[i]);
   }
   // HERE OPEN DYNAMICS CAN BE ADDED
}
%-------------------------------------------------------------------------
void set_dudp(double &u, double &p, double &du, double &dp, cvec &TEMP, cvec
    &RHO_t_tk, cvec &dHkdu)
/**
 *  Calculate t.d. change of nuclear displacement u and momentum p
 *  -TEMP1, TEMP2: Complex helper matrix
 *  -RHO_t_tk: Complex vector[4] of k- and time-dependent density matrix
 *  -dRHO_dt: Complex vector[4] of temporal change of density matrix
 *  -Hk: Complex vector[4] to store Hamiltonian matrix
 */
{
   du = p/(4.*K/pow(w0,2.));
   times(RHO_t_tk, dHkdu, TEMP);
   dp += -2./double(NN)*real(TEMP[fq(0,0,2)]+TEMP[fq(1,1,2)]) -
      4.*K*u/(double(NN)/2.);
```

```
}
%-------------------------------------------------------------------
void AB2_propatation(vector<dvec> &E_TOT, dvec &evals, vector<cvec> &RHO_0,
    vector<cvec> &dRHO_dt0, vector<cvec> &dRHO_dt1, double &u, double &p, cvec
    &Hk, dvec &BZ, vector<cvec*> RHO_t, vector<dvec> &ORDER_t, int &numprocs, int
    &myrank)
/**
 * Two-step Adams-Bashforth prdictor corrector method for propagation of full
     (el+nuc) system
 *  -E_TOT: Vector[timesteps] of real vectors[2] to store enrgies
 *  -evals: Real vector[2] of eigenvalues
 *  -RHO_0: Vector[num_k] of real vectors[4] to store density matrix
 *  -dRHO_dt0, dRHO_dt1: Vector of complex vectors[64] to store change of density
     matrix
 *  -u: nuclear displacement
 *  -p: nuclear momentum
 *  -Hk: Complex vector[4] to store Hamiltonian
 *  -BZ: Real vector[NN/2] of 1d reduced Brilluoin zone
 *  -RHO_t_tk: Vector[4] ofcomplex vector pointers to store t.-d. density matrix
 *  -ORDER_t: Vector[timesteps] of real vectors[2] to store t.-d. u(t) and p(t)
 *  -numprocs: Total number of processes (MPI)
 *  -myrank: Rank of process (MPI)
 */
{
   double du0, du1, dp0, dp1, uu, E_tot, E_nuc, time, h;
   cvec *temp0, *temp1, *temp2;
    h = (endtime-starttime)/timesteps;

    cvec TEMP1(4,0.);
   cvec TEMP2(4,0.);

    //p=10.;

   // Initial Order
   ORDER_t[0][0] = u;
   ORDER_t[0][1] = p;

   for(int k=myrank; k<NN/2; k+=numprocs)
   {
      for(int i=0; i<4; i++)
```

```
      {
         (*RHO_t[fq(0, k, NN/2)])[i] = RHO_0[k][i];
      }
   }

   // Propagation
   for(int t=0; t<timesteps-1; t++)
   {
      // 1st Euler step
      if(t==0)
      {
         dp0 = 0.;
         for(int k=myrank; k<NN/2; k+=numprocs)
         {
            set_dHkdu(BZ[k], ORDER_t[0][0], Hk, h*double(t));
            set_dudp(ORDER_t[0][0], ORDER_t[0][1], du0, dp0, TEMP1, RHO_t[fq(0,
                k, NN/2)][0], Hk);
            set_Hk(BZ[k], ORDER_t[0][0], Hk, h*double(t));
            set_dRHOdt(TEMP1, TEMP2, RHO_t[fq(0,k,NN/2)][0], dRHO_dt0[k], Hk);
            for(int i=0; i<4; i++)
            {
               (*RHO_t[fq(1,k,NN/2)])[i] = (*RHO_t[fq(0,k,NN/2)])[i] +
                  h*dRHO_dt0[k][i];
               RHO_0[k][i] = (*RHO_t[fq(1,k,NN/2)])[i];
            }
         }

#ifndef  NO_MPI
         MPI_Allreduce(MPI_IN_PLACE, &dp0, 1, MPI_DOUBLE, MPI_SUM,
             MPI_COMM_WORLD);
#endif
         //cout << "dp0: " << dp0 << endl;
         ORDER_t[t+1][0] = ORDER_t[t][0] + h*du0*SWITCH_OFF;
         ORDER_t[t+1][1] = ORDER_t[t][1] + h*dp0*SWITCH_OFF;

         E_tot = 0.0;
         for(int k=myrank; k<NN/2; k+=numprocs)
         {
            // Calculation of total electronic energy per unit cell
            set_Hk(BZ[k], ORDER_t[t+1][0], Hk, h*double(t+1));
```

```
      times(RHO_0[k], Hk, TEMP1);
      for(int i=0; i<2; i++)
      {
         E_tot += real(TEMP1[fq(i,i,2)])/(double(NN)/2.);
      }
   }
   MPI_Allreduce(MPI_IN_PLACE, &E_tot, 1, MPI_DOUBLE, MPI_SUM,
       MPI_COMM_WORLD);
   E_nuc = 2.*(2.*K*pow(ORDER_t[t][0],2.)+
       pow(ORDER_t[t][2],2)/(2.*4.*K/pow(w0,2.)));
   E_TOT[t+1][0] = E_tot;
   E_TOT[t+1][1] = E_nuc;
}
else
{  // 2-step Adams predictor
   dp0 = 0.;
   dp1 = 0.;
   for(int k=myrank; k<NN/2; k+=numprocs)
   {
      set_dHkdu(BZ[k], ORDER_t[0][0], Hk, h*double(t-1));
      set_dudp(ORDER_t[t-1][0], ORDER_t[t-1][1], du0, dp0, TEMP1,
          RHO_t[fq(0, k, NN/2)][0], Hk);
      set_dHkdu(BZ[k], ORDER_t[0][0], Hk, h*double(t));
      set_dudp(ORDER_t[t][0], ORDER_t[t][1], du1, dp1, TEMP1, RHO_t[fq(1,
          k, NN/2)][0], Hk);
      set_Hk(BZ[k], ORDER_t[t-1][0], Hk, h*double(t-1));
      set_dRHOdt(TEMP1, TEMP2, RHO_t[fq(0,k,NN/2)][0], dRHO_dt0[k], Hk);
      set_Hk(BZ[k], ORDER_t[t][0], Hk, h*double(t));
      set_dRHOdt(TEMP1, TEMP2, RHO_t[fq(1,k,NN/2)][0], dRHO_dt1[k], Hk);

      for(int i=0; i<4; i++)
      {
         // P_{n+1} = y_{n} + 3/2*h*f(t_{n},y_{n}) -
             0.5*h*f(t_{n-1},y_{n-1})
         (*RHO_t[fq(2,k,NN/2)])[i] = (*RHO_t[fq(1,k,NN/2)])[i] +
             h*(3./2.*dRHO_dt1[k][i] - 0.5*dRHO_dt0[k][i]);
         RHO_0[k][i] = (*RHO_t[fq(2,k,NN/2)])[i];
      }
   }
```

```
#ifndef  NO_MPI
        MPI_Allreduce(MPI_IN_PLACE, &dp0, 1, MPI_DOUBLE, MPI_SUM,
            MPI_COMM_WORLD);
        MPI_Allreduce(MPI_IN_PLACE, &dp1, 1, MPI_DOUBLE, MPI_SUM,
            MPI_COMM_WORLD);
#endif
        ORDER_t[t+1][0] = ORDER_t[t][0] + h*(3./2.*du1 - 0.5*du0)*SWITCH_OFF;
        ORDER_t[t+1][1] = ORDER_t[t][1] + h*(3./2.*dp1 - 0.5*dp0)*SWITCH_OFF;

        // 2-step Moulton corrector
        dp0 = 0.;
        for(int k=myrank; k<NN/2; k+=numprocs)
        {
           set_dHkdu(BZ[k], ORDER_t[0][0], Hk, h*double(t));
           set_dudp(ORDER_t[t+1][0], ORDER_t[t+1][1], du0, dp0, TEMP1,
               RHO_t[fq(2, k, NN/2)][0], Hk);
           set_Hk(BZ[k], ORDER_t[t+1][0], Hk, h*double(t+1));
           set_dRHOdt(TEMP1, TEMP2, RHO_t[fq(2,k,NN/2)][0], dRHO_dt0[k], Hk);
           for(int i=0; i<4; i++)
           {
              // y_{n+1} = y_{n} + 1/2*h*(f(t_{n+1},P_{n+1}) + f(t_{n},y_{n}))
              (*RHO_t[fq(2,k,NN/2)])[i] = (*RHO_t[fq(1,k,NN/2)])[i] +
                  0.5*h*(dRHO_dt0[k][i] + dRHO_dt1[k][i]);
              RHO_0[k][i] = (*RHO_t[fq(2,k,NN/2)])[i];
           }

           // Cyclic exchange of pointers
           temp0 = RHO_t[fq(0,k,NN/2)];
           temp1 = RHO_t[fq(1,k,NN/2)];
           temp2 = RHO_t[fq(2,k,NN/2)];

           RHO_t[fq(0,k,NN/2)] = temp1;
           RHO_t[fq(1,k,NN/2)] = temp2;
           RHO_t[fq(2,k,NN/2)] = temp0;
        }

#ifndef  NO_MPI
        MPI_Allreduce(MPI_IN_PLACE, &dp0, 1, MPI_DOUBLE, MPI_SUM,
            MPI_COMM_WORLD);
#endif
```

```
        ORDER_t[t+1][0] = ORDER_t[t][0] + 0.5*h*(du0 + du1)*SWITCH_OFF;
        ORDER_t[t+1][1] = ORDER_t[t][1] + 0.5*h*(dp0 + dp1)*SWITCH_OFF;

        E_tot = 0.0;
        for(int k=myrank; k<NN/2; k+=numprocs)
        {
           // Calculation of total electronic energy per unit cell
           set_Hk(BZ[k], ORDER_t[t+1][0], Hk, h*double(t+1));
           times(RHO_0[k], Hk, TEMP1);
           for(int i=0; i<2; i++)
           {
              E_tot += real(TEMP1[fq(i,i,2)])/(double(NN)/2.);
           }
        }
        MPI_Allreduce(MPI_IN_PLACE, &E_tot, 1, MPI_DOUBLE, MPI_SUM,
            MPI_COMM_WORLD);
        E_nuc = 2.*(2.*K*pow(ORDER_t[t][0],2.)+
            pow(ORDER_t[t][2],2)/(2.*4.*K/pow(w0,2.)));
        E_TOT[t+1][0] = E_tot;
        E_TOT[t+1][1] = E_nuc;
     }
   }
}
```

B.5 SP III

Listing 17: Taylor-expanded Hamiltonian in k-orbital basis

```
void set_Hk_Taylor(dvec &kvec, vector<cvec*> Hk_Taylor, const dvec &lvec,
    vector<dvec> &UNIT_CELL)
/**
 * Sets matrizes of Taylor expansion of Hk in k-orbital basis for small fields
     A(t)-->0
 *  -kvec: Real vector of the reciprocal space
 *  -Hk_Taylor: Vector of complex matrices[10][NATOM*NATOM] to store Taylor
     matrices
 *  -lvec: Real vector[4] of superlattice bravis translational vectors (in
     lconst*Angstroem)
```

```
 *  -UNIT_CELL: Vector[NATOM] of real vectors[4] containing atomic positions and
     sublattice info
 */
{
   const double lcell = lconst*sqrt(pow(lvec[0],2.)+pow(lvec[1],2.));
   const double qq2 = qq1*aa2/aa1 ;
   const double kx = kvec[0];
   const double ky = kvec[1];

    // bottom layer
#ifndef NO_OMP
    #pragma omp parallel
   {
#endif
   double d, rx, ry, rz;
#ifndef NO_OMP
   #pragma omp for
#endif
   for(int m=0; m<NATOM*NATOM; m++){
      for(int n=0; n<10; n++) {
         (*Hk_Taylor[n])[m] = 0.0;
      }
    }
#ifndef NO_OMP
   #pragma omp for
#endif
   for(int i=0; i<NATOM/2; ++i)
   {
      // Backgate voltage
      (*Hk_Taylor[0])[fq(i,i,NATOM)] = VV/2.;
      // Sublattice potential
      if (UNIT_CELL[i][3] < 0.9){
         (*Hk_Taylor[0])[fq(i,i,NATOM)] += -dgap/2.;
        }
        else{
            (*Hk_Taylor[0])[fq(i,i,NATOM)] += dgap/2.;
        }
      for(int j=i+1; j<NATOM/2; ++j)
      {
         for(int m=0; m<3; ++m)
```

```
{
   for(int n=0; n<3; ++n)
   {
      rx = UNIT_CELL[i][0]-UNIT_CELL[j][0]+double(m-1)*lvec[0]
      +double(n-1)*lvec[2];
      ry = double(m-1)*lvec[1]+UNIT_CELL[i][1]-UNIT_CELL[j][1]
      +double(n-1)*lvec[3];
      rz = UNIT_CELL[i][2]-UNIT_CELL[j][2];
          d = lconst*sqrt(pow(rx,2.)+pow(ry,2.)+pow(rz,2.));
           // 0th order
      (*Hk_Taylor[0])[fq(i,j,NATOM)] +=
          t1/RG*exp(qq1*(1.-(d/aa1)))*exp(II*(kx*lconst*rx+ky*lconst*ry));
      // 1st order
      (*Hk_Taylor[1])[fq(i,j,NATOM)] +=
          t1/RG*exp(qq1*(1.-(d/aa1)))*exp(II*(kx*lconst*rx+ky*lconst*ry))
      *(-II*rx*lconst);
      (*Hk_Taylor[2])[fq(i,j,NATOM)] +=
          t1/RG*exp(qq1*(1.-(d/aa1)))*exp(II*(kx*lconst*rx+ky*lconst*ry))
      *(-II*ry*lconst);
      // 2nd order
      (*Hk_Taylor[3])[fq(i,j,NATOM)] +=
          t1/RG*exp(qq1*(1.-(d/aa1)))*exp(II*(kx*lconst*rx+ky*lconst*ry))
      *(-rx*rx*lconst*lconst);
      (*Hk_Taylor[4])[fq(i,j,NATOM)] +=
          t1/RG*exp(qq1*(1.-(d/aa1)))*exp(II*(kx*lconst*rx+ky*lconst*ry))
      *(-rx*ry*lconst*lconst);
      (*Hk_Taylor[5])[fq(i,j,NATOM)] +=
          t1/RG*exp(qq1*(1.-(d/aa1)))*exp(II*(kx*lconst*rx+ky*lconst*ry))
      *(-ry*ry*lconst*lconst);
      // 3rd order
      (*Hk_Taylor[6])[fq(i,j,NATOM)] +=
          t1/RG*exp(qq1*(1.-(d/aa1)))*exp(II*(kx*lconst*rx+ky*lconst*ry))
      *(II*rx*rx*rx*lconst*lconst*lconst);
      (*Hk_Taylor[7])[fq(i,j,NATOM)] +=
          t1/RG*exp(qq1*(1.-(d/aa1)))*exp(II*(kx*lconst*rx+ky*lconst*ry))
      *(II*rx*rx*ry*lconst*lconst*lconst);
      (*Hk_Taylor[8])[fq(i,j,NATOM)] +=
          t1/RG*exp(qq1*(1.-(d/aa1)))*exp(II*(kx*lconst*rx+ky*lconst*ry))
      *(II*rx*ry*ry*lconst*lconst*lconst);
```

```
            (*Hk_Taylor[9])[fq(i,j,NATOM)] +=
               t1/RG*exp(qq1*(1.-(d/aa1)))*exp(II*(kx*lconst*rx+ky*lconst*ry))
            *(II*ry*ry*ry*lconst*lconst*lconst);

         }
      }
      for(int nn=0; nn<10; nn++) {
         (*Hk_Taylor[nn])[fq(j,i,NATOM)]=
            conj((*Hk_Taylor[nn])[fq(i,j,NATOM)]);
      }
   }
}
// Top layer
#ifndef NO_OMP
   #pragma omp for
#endif
   for(int i=NATOM/2; i<NATOM; ++i)
   {
      // Top-gate voltage
      (*Hk_Taylor[0])[fq(i,i,NATOM)] = -VV/2.;
      // Sublattice potential
      if (UNIT_CELL[i][3] < 0.9){
         (*Hk_Taylor[0])[fq(i,i,NATOM)] += -dgap/2.;
       }
       else{
          (*Hk_Taylor[0])[fq(i,i,NATOM)] += dgap/2.;
       }
      for(int j=i+1; j<NATOM; ++j)
      {
         for(int m=0; m<3; ++m)
         {
            for(int n=0; n<3; ++n)
            {
               rx = UNIT_CELL[i][0]-UNIT_CELL[j][0]+double(m-1)*lvec[0]
               +double(n-1)*lvec[2];
               ry = double(m-1)*lvec[1]+UNIT_CELL[i][1]-UNIT_CELL[j][1]
               +double(n-1)*lvec[3];
               rz = UNIT_CELL[i][2]-UNIT_CELL[j][2];
                   d = lconst*sqrt(pow(rx,2.)+pow(ry,2.)+pow(rz,2.));
                    // 0th order
```

```
            (*Hk_Taylor[0])[fq(i,j,NATOM)] +=
               t1/RG*exp(qq1*(1.-(d/aa1)))*exp(II*(kx*lconst*rx+ky*lconst*ry));
            // 1st order
            (*Hk_Taylor[1])[fq(i,j,NATOM)] +=
               t1/RG*exp(qq1*(1.-(d/aa1)))*exp(II*(kx*lconst*rx+ky*lconst*ry))
            *(-II*rx*lconst);
            (*Hk_Taylor[2])[fq(i,j,NATOM)] +=
               t1/RG*exp(qq1*(1.-(d/aa1)))*exp(II*(kx*lconst*rx+ky*lconst*ry))
            *(-II*ry*lconst);
            // 2nd order
            (*Hk_Taylor[3])[fq(i,j,NATOM)] +=
               t1/RG*exp(qq1*(1.-(d/aa1)))*exp(II*(kx*lconst*rx+ky*lconst*ry))
            *(-rx*rx*lconst*lconst);
            (*Hk_Taylor[4])[fq(i,j,NATOM)] +=
               t1/RG*exp(qq1*(1.-(d/aa1)))*exp(II*(kx*lconst*rx+ky*lconst*ry))
            *(-rx*ry*lconst*lconst);
            (*Hk_Taylor[5])[fq(i,j,NATOM)] +=
               t1/RG*exp(qq1*(1.-(d/aa1)))*exp(II*(kx*lconst*rx+ky*lconst*ry))
            *(-ry*ry*lconst*lconst);
            // 3rd order
            (*Hk_Taylor[6])[fq(i,j,NATOM)] +=
               t1/RG*exp(qq1*(1.-(d/aa1)))*exp(II*(kx*lconst*rx+ky*lconst*ry))
            *(II*rx*rx*rx*lconst*lconst*lconst);
            (*Hk_Taylor[7])[fq(i,j,NATOM)] +=
               t1/RG*exp(qq1*(1.-(d/aa1)))*exp(II*(kx*lconst*rx+ky*lconst*ry))
            *(II*rx*rx*ry*lconst*lconst*lconst);
            (*Hk_Taylor[8])[fq(i,j,NATOM)] +=
               t1/RG*exp(qq1*(1.-(d/aa1)))*exp(II*(kx*lconst*rx+ky*lconst*ry))
            *(II*rx*ry*ry*lconst*lconst*lconst);
            (*Hk_Taylor[9])[fq(i,j,NATOM)] +=
               t1/RG*exp(qq1*(1.-(d/aa1)))*exp(II*(kx*lconst*rx+ky*lconst*ry))
            *(II*ry*ry*ry*lconst*lconst*lconst);
         }
      }
      for(int nn=0; nn<10; nn++) {
         (*Hk_Taylor[nn])[fq(j,i,NATOM)]=
             conj((*Hk_Taylor[nn])[fq(i,j,NATOM)]);
      }
   }
}
```

```
   // Inter-layer terms
#ifndef NO_IC
#ifndef NO_OMP
   #pragma omp for
#endif
   for(int i=0; i<NATOM/2; ++i)
   {
      for(int j=NATOM/2; j<NATOM; ++j)
      {
         for(int m=0; m<3; ++m)
         {
            for(int n=0; n<3; ++n)
            {
               rx = UNIT_CELL[i][0]-UNIT_CELL[j][0]+double(m-1)*lvec[0]
               +double(n-1)*lvec[2];
               ry = double(m-1)*lvec[1]+UNIT_CELL[i][1]-UNIT_CELL[j][1]
               +double(n-1)*lvec[3];
               rz = UNIT_CELL[i][2]-UNIT_CELL[j][2];
                   d = lconst*sqrt(pow(rx,2.)+pow(ry,2.)+pow(rz,2.));
                   // 0th order
               (*Hk_Taylor[0])[fq(i,j,NATOM)] +=
                   (1.-pow(aa2/d,2.))*t1/RG*exp(qq1*(1.-(d/aa1)))
               *exp(II*(kx*lconst*rx+ky*lconst*ry));
               (*Hk_Taylor[0])[fq(i,j,NATOM)] +=
                   pow(aa2/d,2.)*t2*exp(qq2*(1.-(d/aa2)))
               *exp(II*(kx*lconst*rx+ky*lconst*ry));
               // 1st order
               (*Hk_Taylor[1])[fq(i,j,NATOM)] +=
                   (1.-pow(aa2/d,2.))*t1/RG*exp(qq1*(1.-(d/aa1)))
               *exp(II*(kx*lconst*rx+ky*lconst*ry))*(-II*rx*lconst);
               (*Hk_Taylor[1])[fq(i,j,NATOM)] +=
                   pow(aa2/d,2.)*t2*exp(qq2*(1.-(d/aa2)))
               *exp(II*(kx*lconst*rx+ky*lconst*ry))*(-II*rx*lconst);

               (*Hk_Taylor[2])[fq(i,j,NATOM)] +=
                   (1.-pow(aa2/d,2.))*t1/RG*exp(qq1*(1.-(d/aa1)))
               *exp(II*(kx*lconst*rx+ky*lconst*ry))*(-II*ry*lconst);
               (*Hk_Taylor[2])[fq(i,j,NATOM)] +=
                   pow(aa2/d,2.)*t2*exp(qq2*(1.-(d/aa2)))
               *exp(II*(kx*lconst*rx+ky*lconst*ry))*(-II*ry*lconst);
```

```
// 2nd order
(*Hk_Taylor[3])[fq(i,j,NATOM)] +=
   (1.-pow(aa2/d,2.))*t1/RG*exp(qq1*(1.-(d/aa1)))
*exp(II*(kx*lconst*rx+ky*lconst*ry))*(-rx*rx*lconst*lconst);
(*Hk_Taylor[3])[fq(i,j,NATOM)] +=
   pow(aa2/d,2.)*t2*exp(qq2*(1.-(d/aa2)))
*exp(II*(kx*lconst*rx+ky*lconst*ry))*(-rx*rx*lconst*lconst);

(*Hk_Taylor[4])[fq(i,j,NATOM)] +=
   (1.-pow(aa2/d,2.))*t1/RG*exp(qq1*(1.-(d/aa1)))
*exp(II*(kx*lconst*rx+ky*lconst*ry))*(-rx*ry*lconst*lconst);
(*Hk_Taylor[4])[fq(i,j,NATOM)] +=
   pow(aa2/d,2.)*t2*exp(qq2*(1.-(d/aa2)))
*exp(II*(kx*lconst*rx+ky*lconst*ry))*(-rx*ry*lconst*lconst);

(*Hk_Taylor[5])[fq(i,j,NATOM)] +=
   (1.-pow(aa2/d,2.))*t1/RG*exp(qq1*(1.-(d/aa1)))
*exp(II*(kx*lconst*rx+ky*lconst*ry))*(-ry*ry*lconst*lconst);
(*Hk_Taylor[5])[fq(i,j,NATOM)] +=
   pow(aa2/d,2.)*t2*exp(qq2*(1.-(d/aa2)))
*exp(II*(kx*lconst*rx+ky*lconst*ry))*(-ry*ry*lconst*lconst);
// 3rd order
(*Hk_Taylor[6])[fq(i,j,NATOM)] +=
   (1.-pow(aa2/d,2.))*t1/RG*exp(qq1*(1.-(d/aa1)))
*exp(II*(kx*lconst*rx+ky*lconst*ry))*(II*rx*rx*rx*lconst*lconst*lconst);
(*Hk_Taylor[6])[fq(i,j,NATOM)] +=
   pow(aa2/d,2.)*t2*exp(qq2*(1.-(d/aa2)))
*exp(II*(kx*lconst*rx+ky*lconst*ry))*(II*rx*rx*rx*lconst*lconst*lconst);

(*Hk_Taylor[7])[fq(i,j,NATOM)] +=
   (1.-pow(aa2/d,2.))*t1/RG*exp(qq1*(1.-(d/aa1)))
*exp(II*(kx*lconst*rx+ky*lconst*ry))
*(II*rx*rx*ry*lconst*lconst*lconst);
(*Hk_Taylor[7])[fq(i,j,NATOM)] +=
   pow(aa2/d,2.)*t2*exp(qq2*(1.-(d/aa2)))
*exp(II*(kx*lconst*rx+ky*lconst*ry))
*(II*rx*rx*ry*lconst*lconst*lconst);

(*Hk_Taylor[8])[fq(i,j,NATOM)] +=
   (1.-pow(aa2/d,2.))*t1/RG*exp(qq1*(1.-(d/aa1)))
```

```
                *exp(II*(kx*lconst*rx+ky*lconst*ry))
                *(II*rx*ry*ry*lconst*lconst*lconst);
                (*Hk_Taylor[8])[fq(i,j,NATOM)] +=
                   pow(aa2/d,2.)*t2*exp(qq2*(1.-(d/aa2)))
                *exp(II*(kx*lconst*rx+ky*lconst*ry))
                *(II*rx*ry*ry*lconst*lconst*lconst);

                (*Hk_Taylor[9])[fq(i,j,NATOM)] +=
                   (1.-pow(aa2/d,2.))*t1/RG*exp(qq1*(1.-(d/aa1)))
                *exp(II*(kx*lconst*rx+ky*lconst*ry))
                *(II*ry*ry*ry*lconst*lconst*lconst);
                (*Hk_Taylor[9])[fq(i,j,NATOM)] +=
                   pow(aa2/d,2.)*t2*exp(qq2*(1.-(d/aa2)))
                *exp(II*(kx*lconst*rx+ky*lconst*ry))
                *(II*ry*ry*ry*lconst*lconst*lconst);
             }
          }
          for(int nn=0; nn<10; nn++) {
             (*Hk_Taylor[nn])[fq(j,i,NATOM)]=
                 conj((*Hk_Taylor[nn])[fq(i,j,NATOM)]);
          }
       }
    }
#endif
#ifndef NO_OMP
    }
#endif
}
```

Listing 18: Set window for energy cut-off

```
void find_dim_DOWN(int &dim_new, vector<int> &limits, double &mu, dvec &evals,
    cvec &Hk, dvec &kvec, const dvec &lvec, vector<dvec> &UNIT_CELL, int &myrank)
/**
 * Find dimension dim_new of downfolded Hamiltonian
 * -dim_new: integer value of reduced leading order of Hamiltonian
 * -limits: integer vector[2] to store upper/lower limit regarding energy
     cut-off [-w_peierls*lim,w_peierls*lim)
 * -mu: Chemical potential
 * -evals: Real vector[NATOM] to store eigenvalues
```

```
 * -Hk: Complex vector[NATOM*NATOM] to store Hamiltonian
 * -kvec: quasi momentum
 * -lvec: superlattice bravis translational vectors (in lconst*Angstroem)
 * -UNIT_CELL: Vector[NATOM] of real vectors[4] containing atomic positions and
     sublattice info
 * -myrank: Rank of process (MPI)
 */
{
   set_Hk0(kvec, Hk, lvec, UNIT_CELL);
   diagonalize(Hk, evals);
   // Find indices of appropriate window for energies:
   int lower, upper;
   for(int i=0; i<NATOM; ++i)
      if(evals[i]-mu>-lim*w_peierls)
      {
         lower = i;
         break;
      }
   for(int i=0; i<NATOM; ++i)
      if(evals[i]-mu>lim*w_peierls)
      {
         upper = i;
         break;
      }
   if(lim*w_peierls>evals[NATOM-1]-mu)
      upper = NATOM-1;

   dim_new = upper-lower;
   limits[0] = lower;
   limits[1] = upper;
}
```

Listing 19: Set truncated Taylor matrices in original band basis

```
void set_Hk_DOWN_LIST(int &dim_new, vector<int> &limits, dvec &kvec, dvec
    &evals, vector<cvec*> Hk_Taylor, vector<cvec*> Hk_DOWN_LIST, const dvec
    &lvec, vector<dvec> &UNIT_CELL, int &myrank)
/**
 * Calculates truncated Taylor matrices in intital band basis
 * -dim_new: integer value of reduced leading order of Hamiltonian
```

```
* -limits: integer vector[2] to store upper/lower limit regarding energy
    cut-off [-w_peierls*lim,w_peierls*lim)
* -kvec: quasi momentum
* -evals: Real vector[NATOM] to store eigenvalues
* -Hk_Taylor: Vector of complex matrices[10][NATOM*NATOM] to store Taylor
    matrices
* -Hk_DOWN_LIST: Vector of complex matrices[10][dim_new*dim_new] to store
    truncated Taylor matrices in initial band basis
* -lvec: superlattice bravis translational vectors (in lconst*Angstroem)
* -UNIT_CELL: Vector[NATOM] of real vectors[4] containing atomic positions and
    sublattice info
* -myrank: Rank of process (MPI)
*/
{
  int dimH = NATOM*NATOM;
  cvec *TEMP = new cvec(dimH);
  cvec *SMAT = new cvec(dimH);

  double dtime1, dtime11;

  int lower = limits[0];
  int upper = limits[1];

  set_Hk0(kvec, SMAT[0], lvec, UNIT_CELL);
  diagonalize(SMAT[0], evals);

  // Transform Tylor matrices to intital band basis
  for(int n=0; n<10; n++) {
     dtime1 = omp_get_wtime();
     const clock_t begin_time1 = clock();
     times_nd(Hk_Taylor[n][0], SMAT[0], TEMP[0]);
     dtime1 = omp_get_wtime() - dtime1;

     dtime11 = omp_get_wtime();
     const clock_t begin_time11 = clock();
     times(SMAT[0], TEMP[0], Hk_Taylor[n][0]);
     dtime11 = omp_get_wtime() - dtime11;
  }
  delete TEMP, SMAT;
  // Store truncated matrices
```

```
#ifndef NO_OMP
   #pragma omp parallel for
#endif
   for(int i=lower; i<upper; ++i)
   {
      for(int j=lower; j<upper; ++j)
      {
         for(int n=0; n<10; n++) {
            (*Hk_DOWN_LIST[n])[fq(i-lower,j-lower,dim_new)] =
               (*Hk_Taylor[n])[fq(i,j,NATOM)];
         }
      }
   }
}
```

Listing 20: Set t.-d. Hamiltonian in original band basis

```
void set_Hk_DOWN(int &dim_new, cvec &Hk_DOWN, vector<cvec*> Hk_DOWN_LIST, dvec
    &ASD, double &Pol, double time)
/**
  *   Set downfolded td Hamiltonian
  * -dim_new: integer value of reduced leading order of Hamiltonian
 *  -Hk_DOWN: Complex vector[dim_new x dim_new] to store Hamiltonian matrix
  * -Hk_DOWN_LIST: Vector of complex matrices[10][dim_new x dim_new] to store
     truncated Taylor matrices in initial band basis
  * -ASD: Gauge field of source-drain field
  * -Pol: double to set chirality
  * -time: tiome variable
  */
{
   double AX = Ax_t(Pol,time,ASD)/lconst;
   double AY = Ay_t(time)/lconst;

   for(int i=0; i<dim_new*dim_new; ++i){
      Hk_DOWN[i] = (*Hk_DOWN_LIST[0])[i] + FIRST*((*Hk_DOWN_LIST[1])[i]*AX +
          (*Hk_DOWN_LIST[2])[i]*AY) + SECOND*1./2.*((*Hk_DOWN_LIST[3])[i]*AX*AX +
          2.*(*Hk_DOWN_LIST[4])[i]*AX*AY + (*Hk_DOWN_LIST[5])[i]*AY*AY) +
          THIRD*1./6.*((*Hk_DOWN_LIST[6])[i]*AX*AX*AX +
          3.*(*Hk_DOWN_LIST[7])[i]*AX*AX*AY + 3.*(*Hk_DOWN_LIST[8])[i]*AX*AY*AY +
          (*Hk_DOWN_LIST[9])[i]*AY*AY*AY);
```

```
   }
}
```

Listing 21: Set t.-d. derivative of Hamiltonian by Ax in original band basis

```
void set_dHkdAx_DOWN(int &dim_new, cvec &Hk_DOWN, vector<cvec*> Hk_DOWN_LIST,
    dvec &ASD, double &Pol, double time)
/**
  * Set downfolded t.-d. derivative by Ax of Hamiltonian
  * -dim_new: integer value of reduced leading order of Hamiltonian
 *  -Hk_DOWN: Complex vector[dim_new x dim_new] to store Hamiltonian matrix
  * -Hk_DOWN_LIST: Vector of complex matrices[10][dim_new x dim_new] to store
      truncated Taylor matrices in initial band basis
  * -ASD: Gauge field of source-drain field
  * -Pol: double to set chirality
  * -time: tiome variable
  */
{
   double AX = Ax_t(Pol,time,ASD)/lconst;
   double AY = Ay_t(time)/lconst;

   for(int i=0; i<dim_new*dim_new; ++i){
      Hk_DOWN[i] = FIRST*(*Hk_DOWN_LIST[1])[i] +
          SECOND*1./2.*(2.*(*Hk_DOWN_LIST[3])[i]*AX +
          2.*(*Hk_DOWN_LIST[4])[i]*AY) +
          THIRD*1./6.*(3.*(*Hk_DOWN_LIST[6])[i]*AX*AX +
          2.*3.*(*Hk_DOWN_LIST[7])[i]*AX*AY + 3.*(*Hk_DOWN_LIST[8])[i]*AY*AY);
   }
}
```

Listing 22: Set t.-d. derivative of Hamiltonian by Ay in original band baisis

```
void set_dHkdAy_DOWN(int &dim_new, cvec &Hk_DOWN, vector<cvec*> Hk_DOWN_LIST,
    dvec &ASD, double &Pol, double time)
/**
  * Set downfolded t.-d. derivative by Ay of Hamiltonian
  * -dim_new: integer value of reduced leading order of Hamiltonian
  * -Hk_DOWN: Complex vector[dim_new x dim_new] to store Hamiltonian matrix
  * -Hk_DOWN_LIST: Vector of complex matrices[10][dim_new x dim_new] to store
      truncated Taylor matrices in initial band basis
```

```
  * -ASD: Gauge field of source-drain field
  * -Pol: double to set chirality
  * -time: tiome variable
  */
{
   double AX = Ax_t(Pol,time,ASD)/lconst;
   double AY = Ay_t(time)/lconst;

   for(int i=0; i<dim_new*dim_new; ++i){
      Hk_DOWN[i] = FIRST*(*Hk_DOWN_LIST[2])[i] +
          SECOND*1./2.*(2.*(*Hk_DOWN_LIST[4])[i]*AX +
          2.*(*Hk_DOWN_LIST[5])[i]*AY) +
          THIRD*1./6.*(3.*(*Hk_DOWN_LIST[7])[i]*AX*AX +
          2.*3.*(*Hk_DOWN_LIST[8])[i]*AX*AY + 3.*(*Hk_DOWN_LIST[9])[i]*AY*AY);
   }
}
```

C Side-project: A TDDFT approach towards laser-tuned superconductivity in magnesium diboride

While this project clearly falls under the topic of laser-mediate control it is not directly connected to the projects that are discussed in the main part of this thesis but a small unfinished stand-alone project.

In 2001, by a combination of magnetic susceptibility and electrical resistivity measurements, magnesium diboride (MgB_2) was experimentally identified as a BCS-type superconductor with one of the highest known critical temperatures, $T_c = 39$ K [85]. This material is a three-dimensional hexagonal system (space group P6/mmm). A measured boron-isotope effect [86] suggests a BCS-type origin of superconductivity, dominated by strong electron-phonon coupling. Subsequent experimental (neutron scattering) and theoretical ab initio investigations [87] identified four distinct optical phonon modes at the zone center: E_{1u}, E_{2g}, A_{2u}, and B_{1g}. Among these modes the E_{2g}-boron mode was identified as dominant for the BCS transition. Due to its in-plane stretching character, it couples strongly to the boron-$p_{x/y}$ orbitals which build covalent σ-bonds within the boron plane. Moreover, it moderately couples to the metallic π-bonds of the out-of-plane p_z-orbitals. As discussed in [88], this leads to a two-gap superconducting state with associated pairing gaps of energy $\Delta_\sigma = 6.8$ meV and $\Delta_\pi = 1.8$ meV. This two-gap mechanism finds expression in a step-like quasi-particle density-of-states. Reportedly, the strong coupling of the E_{2g}-mode to the electronic system leads, compared to the other modes, to a strong anharmonicity of its effective potential [87]. The key idea behind this project was to employ the strong nonadiabatic electron-phonon coupling in order to manipulate the phonon frequency by a low-energy excitation of the electronic subsystem via a short laser pulses. This control over the energy scale of the phonon would allow to tune the superconducting mechanism in an ultrafast optical setup. Moreover, TDDFT+U simulations might allow to track the emergence of an effectively attractive electronic interaction of the driven system. This might lead to an enhancement of the superconductive condensation.

All presented results are calculated by use of the (TD)DFT code `octopus`. All calculations are done within the LDA approximation using the exchange-correlation potential `hgh_lda`. The shown data is not revised by a peer-review process and should generally be understood as preliminary. The project, including all input files, is available on `https://github.com/Fizztopp/MgB2.git`.

In a first step, the DFT-groundstate is calculated. The unit cell consists of two boron atoms and one magnesium atom. For the lattice constants the parameters $a = 3.0391$ Å and $c = 3.4866$ Å [89] are employed. The used `inp`-file is of the form 23 (see page 113). After the calculation of the groundstate the electronic band structure is calculated. The `inp`-file is of the form 24 (see page 114). A plot of the corresponding band structure is shown in Fig. 8.

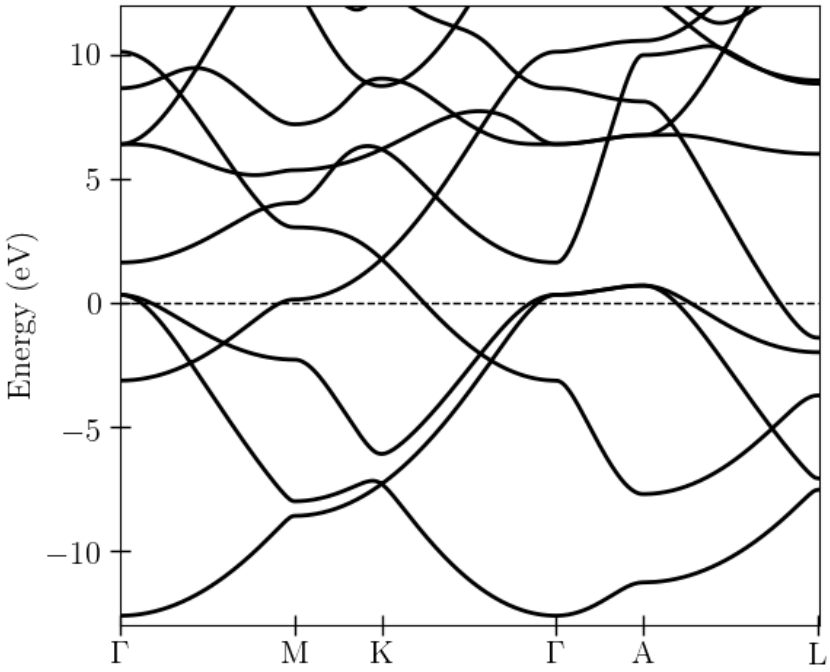

Figure 8: Electronic LDA-band structure of MgB_2.

The calculated energy bands are in good agreement with comparison data from other literature [90].

In a next step, the phonon frequency of the E_{2g}-mode is calculated. This is done by two different approaches. First, the static frozen-phonon calculations are used. Therefore, the two boron nuclei are displaced from their equilibrium positions according to the stretching mode. For every displacement u the total energy $E_{\mathrm{tot}}[u]$ is calculated by calling and performing 25 (see page 115). Approximating the nuclei by harmonic oscillators, the potential energy can be written as [91]

$$\Delta E_{\mathrm{tot}}[u] \approx \frac{\Omega^2}{2} \sum M_k u_k^2 = E^{\mathrm{harm}}(u \neq 0) - E^{\mathrm{harm}}(u = 0).$$

From the evaluation of the second derivative of the potential energy at the origin, the harmonic frequency can be extracted. In the above equation, M_k indicates the mass and u_k the displacement of the k-th nucleus that is involved in the displacive process. For each Boron nucleus an atomic mass of $M_{\mathrm{B}} = 10.811$ amu is assumed. The change in the DFT-calculated total nuclear energy together with a quadratic fit is shown in Fig.9.

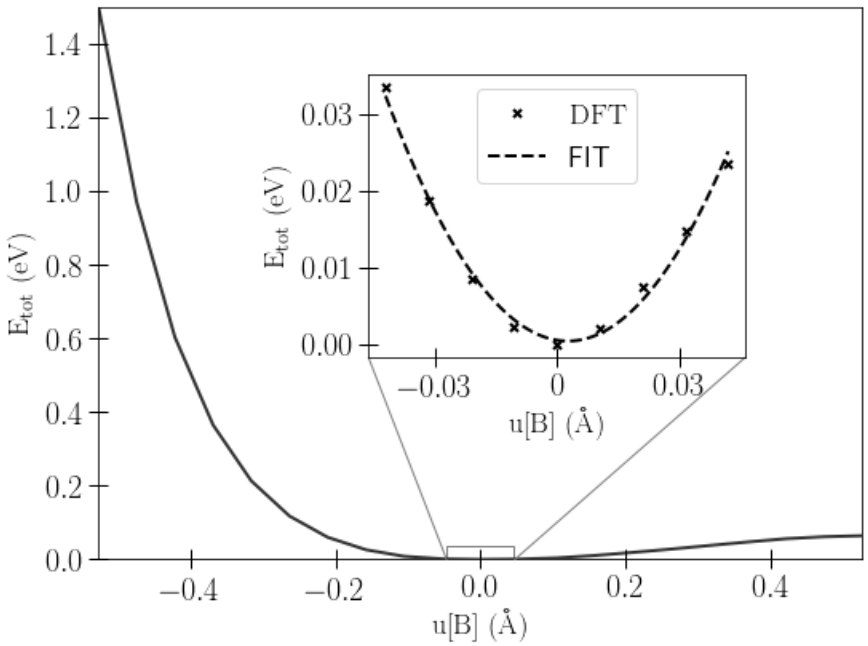

Figure 9: Frozen-phonon calculation for the E_{2g}-mode of MgB_2. The total energy of the system is plotted as a function of the boron displacement. The inset shows the change of energy for very small displacements. The dashed black line indicated a quadratic fit by which the phonon frequency is calculated.

The frozen-phonon approach yields a phonon frequency of $\hbar\Omega^{\mathrm{stat}}_{E_{2g}} = 78.4$ meV. Within the second approach, the phonon frequency is calculated in a time-dependent context. Therefore, the initial state of the nuclear system is set with finite velocity vectors for the boron atoms, pointing in opposite direction according to the stretching mode. The actual propagation is done by a Lanczos method. The time-dependency of the nuclear degrees of freedom are implemented on the basis of Ehrenfest-dynamics. The corresponding `inp`-file is of the form 26 (see page 117). The resulting dynamics of the two boron nuclei are presented in Fig. 10 for for three different initial velocities. Their direction is chosen according to the E_{2g}-mode.

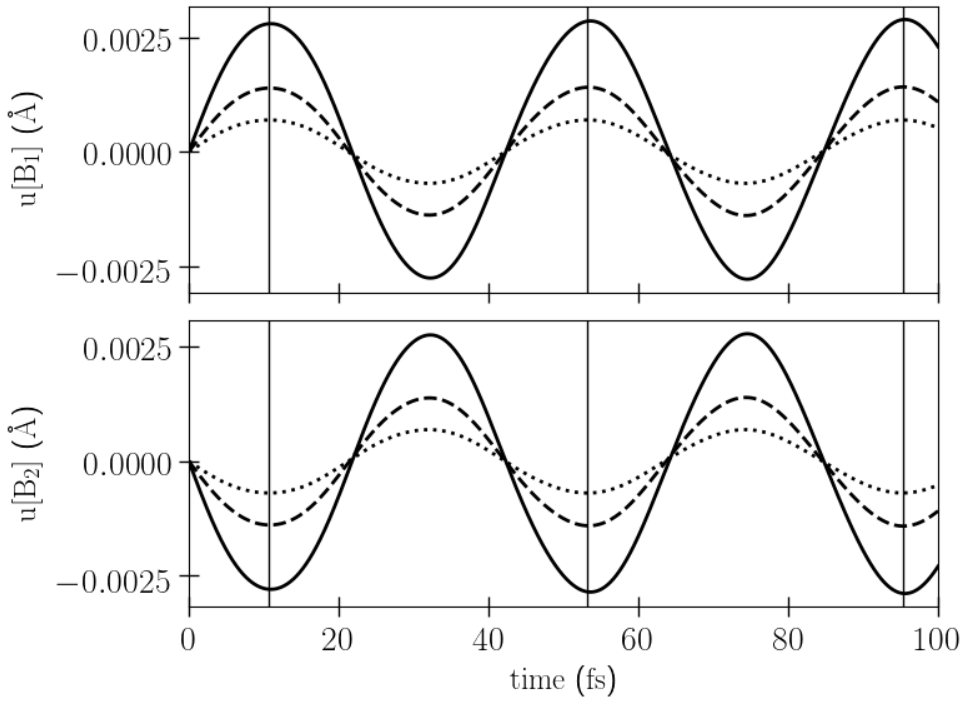

Figure 10: Time-dependent E_{2g}-mode boron displacement of the two boron atoms (B_1 and B_2) for three different initial velocities, $v_0 = 0.5 \cdot 10^{-5}$ a.u. (dotted line), $1.0 \cdot 10^{-5}$ a.u. (dashed line), $2.0 \cdot 10^{-5}$ a.u. (solid line). The vertical lines indicate the maxima/minima of the oscillation.

The linear increase of the oscillation amplitudes with the initial velocities as well as the constant oscillation period clearly indicate that the system is probed in the linear response regime. From the nuclear trajectory an oscillation period of $T = 42.3$ fs can be extracted. This corresponds to a phonon frequency of $\hbar\Omega^{\mathrm{dyn}}_{E_{2g}} = 97.9$ meV. This value is about 20% higher than the result from the frozen-phonon calculation. The discrepancy between the results, calculated by the two different approaches, does per se not imply that the results are wrong. In the dynamical approach the nuclear dynamics are calculated with consideration of a time-dependent polarisation. Thus different results can generally be expected. Likewise, the reported values for the E_{2g}-energy in the literature strongly depend on the employed method and the used parameters. While the value obtained by the static approach lies within the reported interval of 58-82 meV [90], the dynamically calculated value does not. The true origin as well as the validity of the found dynamical hardening of the E_{2g}-mode has to be further investigated by additional studies.

Declaration of contribution **G. E. Topp** set up the `inp`-files with the help of N. Tancogne-Dejean. **G. E. Topp** analysed the (TD)DFT data and created the presented figures. The results were discussed by **G. E. Topp**, M. A. Sentef, and A. Rubio.

Listing 23: DFT groundstate

```
CalculationMode = gs
FromScratch = yes
ExperimentalFeatures = yes

PeriodicDimensions = 3

Spacing = 0.30

BoxShape = parallelepiped

aCell = 3.0391*Angstrom
cCell = 3.4866*Angstrom

%LatticeParameters
 aCell | aCell | cCell
%

%LatticeVectors
 0.5 | -sqrt(3)/2 | 0.
 0.5 |  sqrt(3)/2 | 0.
 0.  | 0.        | 1.
%

%ReducedCoordinates
 'B'  | 2/3 | 1/3 | 0.50
 'B'  | 1/3 | 2/3 | 0.50
 'Mg' | 0.0 | 0.0 | 0.00
%

PseudopotentialSet=hgh_lda
LCAOStart=lcao_states

%KPointsGrid
  12 | 12 | 12
%
KPointsUseSymmetries = no

ParDomains = no
```

```
ParKPoints = auto

ExtraStates = 2

ConvRelDens = 1.e-7

SmearingFunction = fermi_dirac
Smearing = 0.001*eV

Output = geometry
OutputFormat = xcrysden
```

Listing 24: Electronic band structure

```
aCell = 3.0391*Angstrom
cCell = 3.4866*Angstrom

%LatticeParameters
 aCell | aCell | cCell
%

%LatticeVectors
 0.5 | -sqrt(3)/2 | 0.
 0.5 |  sqrt(3)/2 | 0.
 0.  | 0.         | 1.
%

%ReducedCoordinates
 'B'  | 2/3 | 1/3 | 0.50
 'B'  | 1/3 | 2/3 | 0.50
 'Mg' | 0.0 | 0.0 | 0.00
%

PseudopotentialSet=hgh_lda
LCAOStart=lcao_states


%KPointsPath
 100 | 50 | 100 | 50 | 100
 0.0 | 0.0 | 0.0  #Gamma point
```

```
 0.5 | -0.5 | 0.0 # M point
 2/3 | -1/3 | 0.0 # K point
 0.0 |  0.0 | 0.0  # Gamma point
 0.0 |  0.0 | 0.5  # A point
 0.5 | -0.5 | 0.5 # L point
%

ParDomains = no
ParKPoints = auto

%RestartOptions
  restart_gs | "../GS/restart"
%

ExtraStatesToConverge = 5
ExtraStates = 10

ConvRelDens = 1e-7

SmearingFunction = fermi_dirac
Smearing = 0.001*eV

Output = geometry + dos
OutputFormat = xcrysden
```

Listing 25: Frozen-phonon calculation

```
uu=0.0
CalculationMode = gs
FromScratch = yes
ExperimentalFeatures = yes

PeriodicDimensions = 3

Spacing = 0.25

BoxShape = parallelepiped

aCell = 3.0391*Angstrom
cCell = 3.4866*Angstrom
```

```
%LatticeParameters
 aCell | aCell | cCell
%

%LatticeVectors
 0.5 | -sqrt(3)/2 | 0.
 0.5 |  sqrt(3)/2 | 0.
 0.  | 0.         | 1.
%

%ReducedCoordinates
 'B'  | 2/3+uu | 1/3-uu | 0.50
 'B'  | 1/3-uu | 2/3+uu | 0.50
 'Mg' | 0.0    |    0.0 | 0.0
%

PseudopotentialSet=hgh_lda
LCAOStart=lcao_states

%KPointsGrid
  12 | 12 | 12
%

KPointsUseSymmetries = yes

ParDomains = no
ParKPoints = auto

ExtraStates = 2

ConvRelDens = 1.e-7
ConvForce = 1e-8

SmearingFunction = fermi_dirac
Smearing = 0.001*eV

Output = geometry
OutputFormat = xcrysden
```

Listing 26: Dynamcal calcuation of phonon frequency

```
# Calculation mode
#------------------------------------------------------------------------------
CalculationMode = td
FromScratch = yes
ExperimentalFeatures = yes

KPointsUseSymmetries = no

ParKpoints = auto
ParDomains = no

PseudopotentialSet=hgh_lda
LCAOStart=lcao_states

ExtraStates = 2

RestartFixedOccupations = yes

# Structure
#------------------------------------------------------------------------------
PeriodicDimensions = 3
Spacing = 0.30

BoxShape = parallelepiped

aCell = 3.0391*Angstrom
cCell = 3.4866*Angstrom

%LatticeParameters
 aCell | aCell | cCell
%

%LatticeVectors
 0.5 | -sqrt(3)/2 | 0.
 0.5 |  sqrt(3)/2 | 0.
 0.  | 0.        | 1.
%
```

```
%ReducedCoordinates
 'B'  | 2/3 | 1/3 | 0.50
 'B'  | 1/3 | 2/3 | 0.50
 'Mg' | 0.0 | 0.0 | 0.00
%

%KPointsGrid
 12 | 12 | 12
%

%RestartOptions
  restart_gs | "../restart"
%

# Time Propagation
#-------------------------------------------------------------------------------
au2fs = 2.418884 * 1e-2
T_propagation = 100 #fs
T_step = 0.0075       #fs

TDPropagationTime = T_propagation / au2fs
TDTimeStep = T_step / au2fs
RestartWriteInterval = 100
TDExponentialMethod = lanczos
TDExpOrder = 16
TDPropagator = aetrs

# Initial Velocities
#-------------------------------------------------------------------------------
vv = 1.0e-5
%Velocities
 'B'  | 0.0 |  vv | 0.0
 'B'  | 0.0 | -vv | 0.0
 'Mg' | 0.0 | 0.0 | 0.0
%

# TD Output
#-------------------------------------------------------------------------------
MoveIons = yes
TdOutput = energy + geometry
```